Decay Widths from Euclidean Quantum Field Theory; A Scalar Model and Applications to QCD

by

Andrew Nolan

B.A. (Mod.), M.Sc.

A Thesis submitted to
The University of Dublin
for the degree of

Doctor of Philosophy

School of Mathematics
University of Dublin
Trinity College

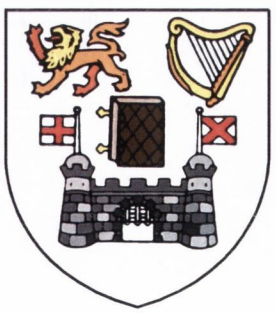

May, 2009

Declaration

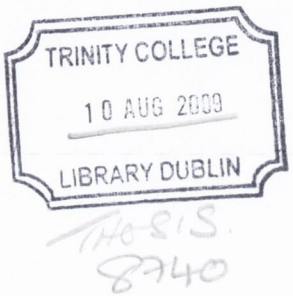

This thesis has not been submitted as an exercise for a degree at any other University. Except where otherwise stated, the work described herein has been carried out by the author alone. This thesis may be borrowed or copied upon request with the permission of the Librarian, University of Dublin, Trinity College. The copyright belongs jointly to the University of Dublin and Andrew Nolan.

Signature of Author .....

Andrew Nolan
May, 2009

Summary

Lüscher provided a method by which the Euclidean correlation function, used in lattice field theories, can be used to evaluate the scattering phase shift, side-stepping the Maiani-Testa Theorem. This result is explored in the context of relativistic particles in a spacially anisotropic box.

Perturbative calculations and anisotropic lattice simulations are used to estimate the decay width of an unstable particle in a scalar quantum field theory, which models the decay of a glueball, G, into a two pion state, $\pi\pi$. The Euclidean perturbative calculations examine the two particle energy spectrum, which is then linked to the scattering phase shift, up to second order in the coupling. The Minkowski perturbative calculations, unrestrained by the Maiani-Testa theorem, afford direct access to the decay width. These results are used as a comparison for the Monte Carlo simulations, in particular to gain an insight into the link between the energy spectrum and the scattering phase shift.

Using Markov Chain Monte Carlo integration techniques applied to anisotropic space-time lattices, we can estimate the exact two particle energy spectrum. From this point, we apply Lüscher's method to recover the scattering phase shift. A genetic fitting algorithm is developed to fit this data to a Breit-Wigner function to provide a value for the decay width.The importance of certain off-diagonal elements of the correlation matrix is noted. When the glueball to $\pi\pi$ case is examined, the analogous elements will be of particular interest. The experience gained from the model theory will provide a foundation for a similar application of Lüscher's method to the $G \to \pi\pi$ decay.

A summary of the current state of glueball research is provided. We then proceed with a thorough discussion of the methods used in glueball simulations, before presenting preliminary results for the $G \to \pi\pi$ correlation matrix entries. In particular, encouraging results using the *distillation* method are given for the $G \to \pi\pi$ correlator.

Acknowledgements

Firstly, my thanks must go to my supervisor, Dr Mike Peardon, for all his help, encouragement and patience. I also wish to thank Dr Sinéad Ryan for her advice and support. The support of all the other members of the Trinlat Collaboration, especially Bugra, was also greatly appreciated. A special thanks must go to all my office mates; Darran, Eduardo, Finnian, Paula and Richie, for, on a daily basis, helping me to appreciate and cherish my normality. I would like to thank all my friends, past and present, especially Nat and Kat, Muireann and Dave, Rory and Mark, Damien and Ruairí, and Paul. The financial support provided by Science Foundation Ireland was greatly appreciated throughout this project. Finally, I would like to thank my family, Mum, Dad, Yvonne, Edmund and, most especially of all, Corrie-Anne, Cathal, Liam, Sarah-Kate, Steffan, Siobhán and Cillian.

For my parents.

Contents

List of Figures

List of Tables

Chapter 1

Introduction

Quantum Chromodynamics (QCD) is widely held as the theory of the strong interaction. It is a non-Abelian $SU(3)$ gauge theory of fermionic fields, called quarks and gauge fields called gluons. These fundamental particles carry a charge in three *colours*, labelled red, green and blue, in analogy with the primary colours. Two of the distinctive properties of QCD are confinement and asymptotic freedom. Confinement states that the force between two quarks does not decrease as their separation increases. Asymptotic freedom states that at high energies, the interactions between quarks and gluons become weak. This theoretical prediction of QCD was demonstrated experimentally and is held as a cornerstone in the assertion of QCD as describing the strong nuclear force. QCD also predicts the existence of bound states of gluons, called *glueballs*. These states are so exotic that confirmation of their existence would provide strong support for the acceptance of QCD. Current research (Sec. 5.1) from various fields mostly accept that some of the experimentally observed resonances correspond to glueball states, though there is little agreement about which of these resonances actually are glueballs. The ultimate goal of this project is to strengthen the link between the experimental and theoretical understanding of glueballs, using Lattice Quantum Chromodynamics.

Lattice Quantum Chromodynaics (LQCD) is the theory of QCD formulated on a discrete space-time grid with spacing a. In this formulation, the quarks fields are represented by values at each grid point, while the gluon fields are represented on the

links between the grid points. Numerical techniques, such as Markov Chain Monte Carlo can be used to evaluate certain fundamental objects in the theory, in particular, correlation functions. This procedure allows for the computational, non-perturbative exploration of QCD, which is automatically regularised by a $1/a$ momentum cut-off. As well as providing a means for the examination of the underlying properties of QCD, such as confinement and the running of the coupling, LQCD also gives access to energy spectra of the particles in the Standard Model, which will be of particular interest to us.

The Problem

Among the predictions of QCD is the existence of glueballs. While their existence is not essential for QCD to hold, confirmation of their existence would provide substantial support to the case for QCD as the theory of the strong interaction. However, as is highlighted in Ref. [1], there is a fundamental disagreement between how the experimentalists and the theorists observe glueballs.

The experimentalists, looking at scattering processes in particle accelerators, measure the differential cross sections, related to decay widths, of the particles to a high level of accuracy. The theorists, on the other hand, use the exponential decay of Euclidean correlation functions to examine the energy spectra of the particles. The contrast between these two approaches is highlighted in Fig. 1-1, which shows typical experimental and theoretical results. It is clear, in this case, that any realtionship between the experimental glueball candidates and the theoretical results is vague.

The first attempt at a solution to this difference in approach might be to use the Euclidean correlation function to gain access to the decay width. But the Maini-Testa Theorem [8] implies that there is no direct access to the decay width from a Euclidean correlation function. (Formally, this theorem states that S-matrix elements cannot be extracted from infinite-volume Euclidean-space Green functions, except at kinematic thresholds.) This theorem does allow for a relationship between decay widths and Minkowski correlation functions. However, the Monte Carlo integration techniques employed to evaluate the correlation functions require a Euclidean formulation to

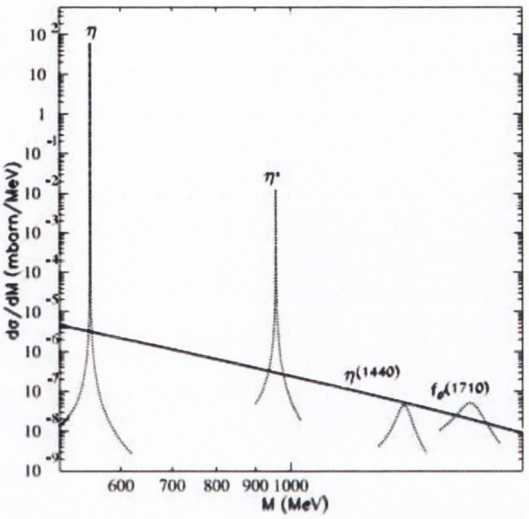

(a) Experimental: Invariant mass distribution of photon production, showing pseudoscalar resonances, η and η', along with glueball candidates, $\eta(1410)$ and $f_0 1710$. Taken from [2].

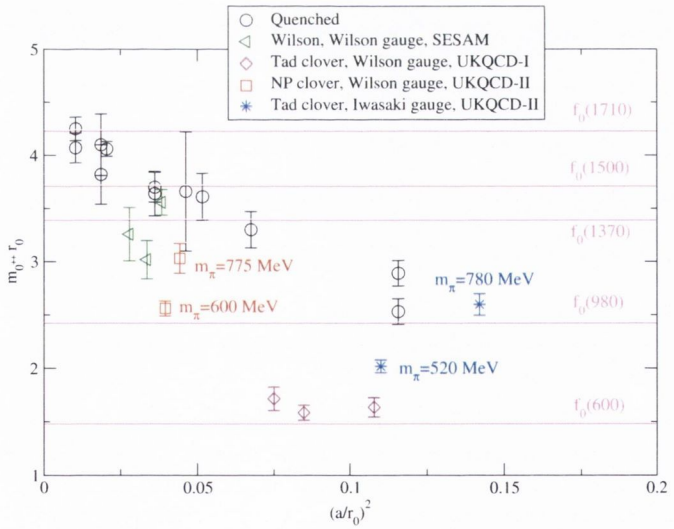

(b) Theoretical: Summary of unquenched results for lightest flavour singlet 0^{++} mesons from [3]. The unquenched results are from SESAM [4], UKQCD-I [5], and UKQCD-II [6]. Taken from [7].

Figure 1-1: Experimental and theoretical results.

provide a positive definite probability measure.

And so, the problem is that LQCD, employed by theorists, can be used to calculate Euclidean correlation functions which, due to the Maiani-Testa Theorem, provide no direct access to decay widths, measured by experimentalists. This forms a fundamental barrier in the identification of glueballs.

The Solution

This problem was addressed by Lüscher [9]. He suggested a relationship between finite volume energy eigenstates, as solutions to the Schrödinger equation, and singular periodic solutions to the Helmholtz equation, related to the scattering phase shift. Once this link between the finite volume energy spectrum and scattering phase shift has been established, the decay width of the particle can easily be recovered from the scattering phase shift using a perturbative expansion or a Breit-Wigner model. While we cannot take the short route across the top of the flow diagram below because of the Maiani-Testa Theorem, we will demonstrate the process of taking the long route from Euclidean correlation function to decay width, via finite volume energy spectrum and scattering phase shift.

$$\begin{array}{ccc} \text{Euclidean Correlation Function} & \not\rightarrow & \text{Decay Width} \\ \downarrow & & \uparrow \\ \text{Finite Volume Energy Spectrum} & \longrightarrow & \text{Scattering Phase Shift} \end{array}$$

Our intention is to demonstrate this principle on a theory which models decay of the glueball, G, into a two pion state, $\pi\pi$. We will demonstrate how the methods prevalent in LQCD can be utilised to apply Lüscher's method to such a decay. We will compare the results using this technique to those of perturbative calculations, before turning our attention to the glueball to $\pi\pi$ decay itself. Using the experience gained from the model theory, we will perform a preliminary examination of the glueball to $\pi\pi$ decay correlation function, with a view to implementing Lüscher's method to this case in the future.

This document is divided up as follows. Chapter 2 presents Luscher's result along with a brief account of its origins. The theory used as a model of the glueball to $\pi\pi$ decay is also discussed. In Chapter 3, the details of the perturbative and Monte Carlo calculations of this model theory are described and the results of these calculations are described in Chapter 4. Chapter 5 details the glueball to $\pi\pi$ theory and measurements. The conclusions of the project are in Chapter 6.

Chapter 2

Volume Dependence of Energy Levels

We now investigate the finite volume effects that come about due to an unstable state. Our goal is to use these finite volume effects to calculate the mass and width of the resonance associated with the unstable state. To get an intuitive idea of the origin of the volume dependence, we will first examine the quantum mechanical case, before looking at a more general case.

We will then discuss the model theory which will be studied over the coming chapters and address the choice of parameter values and box volumes.

2.1 Volume Dependence of the Energy Levels

In this section, we will examine the link between the finite volume energy spectrum and the scattering phase shift. Initially, we will look at a quantum mechanical example to gain an insight into the origin of this connection, before turning our attention to the general case of non-relativistic particles in a spacially anisotropic box. Following Lüscher's approach [9], we will demonstrate how the one-to-one mapping between the singular periodic solutions to the Helmholtz equation and the Schrödinger equation leads to an association between the scattering phase shift and the finite volume energy spectrum.

2.1.1 A Quantum Mechanical Example

In this section, we follow Ref. [10] closely and also Ref. [11]. In the case of two identical, non-relativistic particles of mass m and spin 0, we have the two particle wavefunction, $\psi(x, y)$, which satisfies

$$\psi(x, y) = \psi(y, x) \tag{2.1}$$

The Hamiltonian for the system is of the form

$$H = H_0 + V, \tag{2.2}$$

where

$$H_0\psi(x, y) = -\frac{1}{2m}(\nabla_x^2 + \nabla_y^2)\psi(x, y) \tag{2.3}$$

and

$$V\psi(x, y) = \sum_n \mathcal{V}(x - y + nL)\psi(x, y). \tag{2.4}$$

In the case with zero total momentum, the wavefunction depends only on the particle separation, $z = x - y$, and we can write the Schrödinger equation as

$$\left[-\frac{1}{m}\frac{d^2}{dz^2} + V(z)\right]\psi(z, 0) = E\psi(z, 0) \tag{2.5}$$

For a given E, this has a unique solution

$$\psi_E(z) = e^{-ip|z|} + e^{2i\delta}e^{ip|z|}, \tag{2.6}$$

where $p = \sqrt{mE}$ and $\delta(p)$ is the scattering phase shift. In a finite volume, we impose the periodic boundary conditions

$$\psi_E(-L/2) = \psi_E(L/2), \quad \psi'_E(-L/2) = \psi'_E(L/2). \tag{2.7}$$

This gives us

$$e^{2i\delta(p)}e^{ipL} = 1.$$

$$\Rightarrow \quad pL = 2\pi n - 2\delta(p)$$

Around a resonance, the scattering phase shift can be writen as

$$\delta(p) = \delta_B(p) + \delta_R(p), \tag{2.8}$$

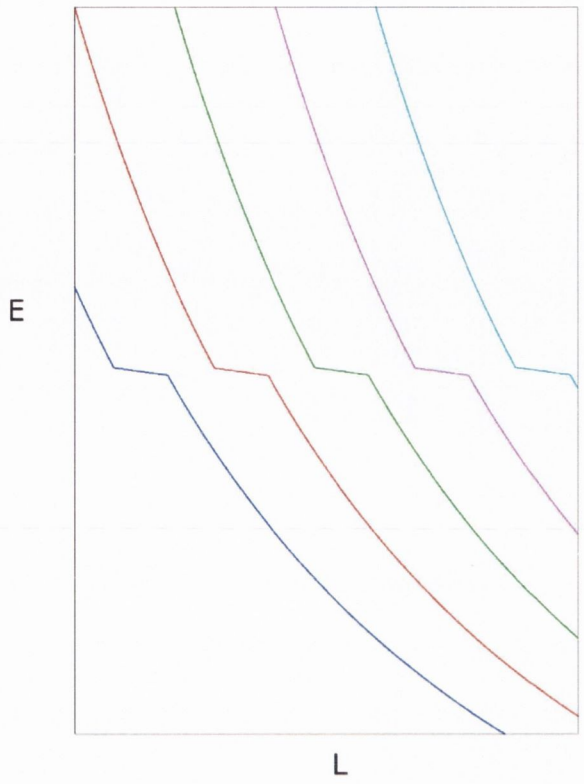

Figure 2-1: Qualitative plot of avoided level crossings.

where δ_B is a smooth background shift and δ_R is the resonance shift, given by

$$\delta_R(p) = \frac{1}{2i} log_e \frac{E_R - E + i\Gamma/2}{E_R - E - i\Gamma/2}. \tag{2.9}$$

Looking at the dependence of E on L in Fig. 2-1, the most striking effect are the plateaus which form at the resonance energy, E_R. These avoided level crossings are a signature of an unstable state and, as we will see, are an intrinsic part of the link between the energy spectrum and the decay width.

Numerical Calculation

As a simple demonstration of this effect, we write a latticised form of the Hamiltonian, H, for a system of two identical particles interacting through the potential

$$V(x,y) = \begin{cases} \alpha & \text{if } |x-y| \leq \delta; \\ 0 & \text{if } |x-y| > \delta. \end{cases} \tag{2.10}$$

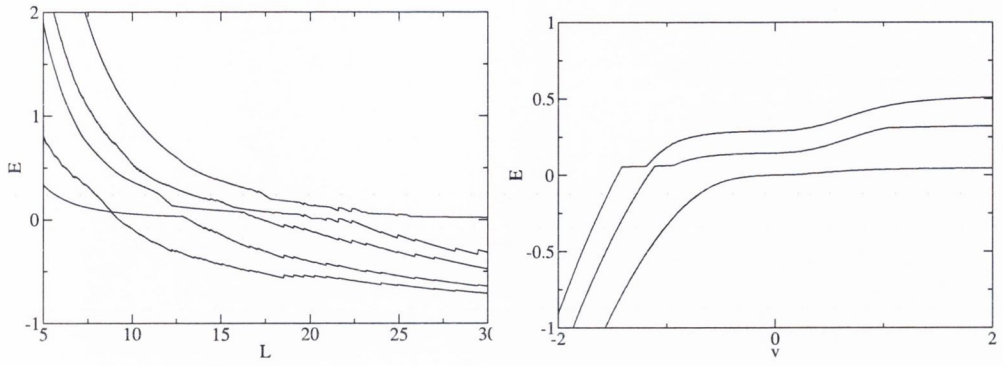

(a) E vs L (b) E vs v

Figure 2-2: Quantum mechanical avoided level crossings.

We rewrite this Hamiltonian in terms of centre of mass and relative coordinates, $x_1 = \frac{x+y}{2}$ and $x_2 = \frac{x-y}{2}$. The energy levels of the system are now given by the eigenvalues of the matrix, H. We can also define $v = \delta\sqrt{m|\alpha|}$, which characterises the strength of the interaction. When we examine the dependence of these eigenvalues on the box size L, in Fig. 2-2, we can see these avoided level crossings quite clearly.

2.1.2 The General Case

Having gained a heuristic idea of the volume dependence of the phase shift in a simple quantum mechanical example, we now move onto the general case of relativistic particles in an anisotropic box. This general case was first described by Lüscher [9], linking the finite volume energy spectrum to the scattering phase shift. This was expanded upon in Ref. [12]. As will be described below, the crucial element of this procedure is the one-to-one relationship between the solutions to the stationary Schrödinger equation, associated with the energy, and the singular periodic solutions to the Helmholtz equation, which can be related to the scattering phase shift. This will lead us to the equation

$$\delta(p) = -\phi(q) \mod \pi, \quad q = \frac{pL}{2\pi}, \tag{2.11}$$

where $\phi(p)$ is a continuous function defined by

$$\tan(-\phi(q)) = \frac{\eta_1 \eta_2 q \pi^{3/2}}{Z_{00}(1, q^2; \eta_1, \eta_2)}, \quad \phi(0) = 0. \tag{2.12}$$

$Z_{00}(s, q^2; \eta_1, \eta_2)$ is a generalised Zeta function;

$$Z_{00}(s, q^2; \eta_1, \eta_2) = \frac{1}{\sqrt{4\pi}} \sum_{\vec{r} \in Z^3} (\tilde{r}^2 - q^2)^{-s} \tag{2.13}$$

The numerical evaluation of $Z_{00}(s, q^2)$ will be looked at in a later section. The variables, η_1 and η_2, are related to the spatial anisotropy of a box of volume $L \times \eta_1 L \times \eta_2 L$. The dependence of the generalised Zeta function on η_1 and η_2 is through the relationship between $\vec{r}$ and $\tilde{r}$; $\tilde{r} = (r_1/\eta_1, r_2/\eta_2, r_3)$.

Energy Eigenstates

For two spinless bosons of mass m with zero total momentum, interacting through a short range force, the state of the system $\psi(\vec{x}, \vec{y})$ is a function only of their relative vector, $\vec{r}$. The Hamiltonian is

$$H = -\frac{\Delta}{m} + V(r). \tag{2.14}$$

The potential is assumed to be smooth and of finite range ($V(r) = 0$ for $r > R$). A solution to the stationary Schrödinger equation

$$H\psi = E\psi \tag{2.15}$$

can be expanded in spherical harmonics;

$$\psi(r) = \sum_{l=0}^{\infty} \sum_{m=-l}^{l} Y_{lm}(\theta, \phi)\psi_{lm}(r). \tag{2.16}$$

The coefficients, $\psi_{lm}(r)$ satisfy the radial Schrödinger equation

$$\left[\frac{d^2}{dr^2} + \frac{2}{r}\frac{d}{dr} - \frac{l(l+1)}{r^2} + k^2 - mV(r)\right]\psi_{lm}(r) = 0. \tag{2.17}$$

The radial Schrödinger equation has only one linearly independent solution, $u_l(r, k)$, which is bounded near the origin, giving us

$$\psi_{lm}(r) = b_{lm}u_l(r, k), \tag{2.18}$$

where

$$E = k^2/m. \tag{2.19}$$

For $r > R$, the potential vanishes, and the solution to the radial Schrödinger equation can be written as a linear combination of spherical Bessel functions, $j_l(kr)$ and $n_l(kr)$;

$$u_l(r, k) = \alpha_l(k)j_l(kr) + \beta_l(k)n_l(kr), \tag{2.20}$$

which gives us

$$\psi(r) = b_{lm}(\alpha_l(k)j_l(kr) + \beta_l(k)n_l(kr)). \tag{2.21}$$

All conventions regarding Legendre polynomials, spherical harmonics and spherical Bessel functions are as in [13]. For our purposes, the most important property of these amplitudes, $\alpha_l(k)$ and $\beta_l(k)$ is their relation to the scattering phase;

$$e^{2i\delta_l(k)} = \frac{\alpha_l(k) + i\beta_l(k)}{\alpha_l(k) - i\beta_l(k)} \tag{2.22}$$

Singular Periodic Solutions to the Helmholtz Equation

When we enclose the particles in a box of volume $L \times \eta_1 L \times \eta_2 L$ the momenta of the particles becomes quantised as $\vec{k} = (2\pi/L)\tilde{n}$. We define, for $\vec{n} \in Z^3$,

$$\tilde{n} = (n_1/\eta_1, n_2/\eta_2, n_3) \tag{2.23}$$

$$\hat{n} = (n_1\eta_1, n_2\eta_2, n_3) \tag{2.24}$$

At this point, we shift our attention to singular solutions of the Helmholtz equation;

$$(\nabla^2 + k^2)\psi(r) = 0. \tag{2.25}$$

The singular periodic solutions to this equation can be formed from the Green's function

$$G(\vec{r}, k^2) = \frac{1}{\eta_1\eta_2 L^3} \sum_{\vec{p}} \frac{e^{i\vec{p}\vec{r}}}{p^2 + k^2}. \tag{2.26}$$

Further singular solutions can be found by differentiating with respect to r. To ensure linear independence of the solutions, we must use differential operators which are not proportional to the Laplacian operator. To this end, we use harmonic polynomials;

$$\mathcal{Y}_{lm}(\vec{r}) = r^l Y_{lm}(\theta, \phi). \tag{2.27}$$

This gives us a set of complete, linearly independent solutions of the Helmholtz equation of degree l;

$$G_{lm}(\vec{r}, k^2) = \mathcal{Y}_{lm}(\nabla) G(\vec{r}, k^2). \tag{2.28}$$

Any general solution can thus be written as a linear combination over this set;

$$\psi(\vec{r}) = \sum_{l=0}^{\Lambda} \sum_{m=-l}^{l} v_{lm} G_{lm}(\vec{r}, k^2). \tag{2.29}$$

The sum over l is conducted up to some angular momentum cut-off, Λ. The original system may be retrieved by taking the $\Lambda \to \infty$ limit. We now expand our basic functions, $G_{lm}(\vec{r}, k^2)$, in terms of spherical harmonics;

$$G_{lm}(\vec{r}, k^2) = \frac{(-1)^l k^{l+1}}{4\pi} \left[Y_{lm}(\Omega_r) n_l(kr) + \sum_{l'm'} M_{lm;l'm'} Y_{l'm'}(\Omega_r) j_{l'}(kr) \right] \tag{2.30}$$

The matrix, $M_{lm;l'm'}$, is given by

$$M_{lm;js} = \sum_{l'm'} \frac{(-1)^s i^{j-l} Z_{l'm'}(1, q^2, \eta_1\eta_2)}{\eta_1\eta_2\pi^{3/2} q^{l'+1}} \sqrt{(2l+1)(2l'+1)(2j+1)} \times \begin{pmatrix} l & l' & j \\ 0 & 0 & 0 \end{pmatrix} \begin{pmatrix} l & l' & j \\ m & m' & -s \end{pmatrix}. \tag{2.31}$$

The convention for the Wigner $3j$ symbols,

$$\begin{pmatrix} j_1 & j_2 & j_3 \\ m_1 & m_2 & m_3 \end{pmatrix}, \tag{2.32}$$

is as presented in [13]. The modified Zeta function is defined by

$$Z_{lm}(s, q^2, \eta_1\eta_2) = \sum_{\vec{n}} \frac{\mathcal{Y}_{lm}(\tilde{n})}{(\tilde{n}^2 - q^2)^s}. \tag{2.33}$$

As we will see later, a closed integral form can be used to evaluate this Zeta function. In [9], a theorem is presented which states that there is a one to one correspondence between the eigenfunctions of H in a finite volume and the singular periodic solutions to the Helmholtz equation. Thus, we can relate our energy eigenstate expansion, Eq.2.21, with our general solution to the Helmhotz equation, Eq. 2.30. This gives us a system of equations in the coefficients, b_{lm};

$$b_{lm}\alpha(k) = \sum_{l'=0}^{\Lambda} \sum_{m'=-l'}^{l'} v_{l'm'} \frac{(-1)^{l'} k^{l'+1}}{4\pi} M_{l'm',lm} \tag{2.34}$$

$$b_{lm}\beta(k) = v_{l'm'} \frac{(-1)^{l'} k^{l'+1}}{4\pi} \tag{2.35}$$

If these equations are recast using our expression for the scattering phase in terms of $\alpha(k)$ and $\beta(k)$, Eq. 2.22, we see that there will only be a non-trivial solution for the coeffiients b_{lm} if

$$\det[e^{2i\delta} - U] = 0, \tag{2.36}$$

where

$$U = \frac{M+i}{M-i}. \tag{2.37}$$

For small relative momentum, k, the scattering phases behave like

$$\tan\delta_l(k) \sim a_l k^{2l+1}. \tag{2.38}$$

In the low momentum limit, d wave and g wave effects can be neglected. Whether we are dealing with cubic symmetry ($\eta_1 = \eta_2 = 1$), D_4 symmetry $\eta_1 = \eta_2 \neq 1$, or D_2 symmetry, the leading contribution is

$$e^{2i\delta_0} = \frac{m_{00} + i}{m_{00} - i}. \tag{2.39}$$

Here, m_{00} is shorthand for the matrix element $M_{lm,l'm'}$. This can be rearranged to give us

$$\tan \delta_0 = \frac{1}{m_{00}} = \frac{\pi^{3/2}\eta_1\eta_2 q}{Z_{00}(1, q^2, \eta_1, \eta_2)}. \tag{2.40}$$

We have now established a link between the finite volume energy spectrum and the scattering phase shift. In the next chapter, we will see how to pratically implement this result to calculate the decay width, using the model theory.

2.2 The Model

We work with a scalar field theory with two fields; ϕ and χ. The Lagrangian for our theory is

$$\mathcal{L} = \frac{1}{2}\phi(-\partial^2 + m_\phi^2)\phi + \frac{1}{2}\chi(-\partial^2 + m_\chi^2)\chi + \lambda\phi\chi^2 + \frac{\mu}{4!}\chi^4 \tag{2.41}$$

For simplicity sake, we write

$$K_\phi = -\partial^2 + m_\phi^2 \tag{2.42}$$

$$K_\chi = -\partial^2 + m_\chi^2 \tag{2.43}$$

We have three free parameters in our theory; m_ϕ, m_χ and λ. As we shall see below the χ^4 coupling, μ, is related to m_ϕ and λ. The fields interact through the term $\mathcal{L}_{int} = \lambda\phi\chi^2$. Above the threshold, ie. when $m_\phi > 2m_\chi$, a ϕ particle can decay into two χ particles (Fig. 2-3). This model is of interest as the $\phi \to \chi\chi$ decay can be seen as first approximation of the $G \to \pi\pi$ decay, with analogies between the ϕ field and the glueball, and the χ field and the pion. The exploration of this $G \to \pi\pi$ decay is our ultimate goal. By investigating this model theory, we hope to understand Lüscher's method more completely when applying it to glueball decays.

2.2.1 An Extra Term in the Action

When we consider the theory

$$\mathcal{L} = \frac{1}{2}\phi(-\partial^2 + m_\phi^2)\phi + \frac{1}{2}\chi(-\partial^2 + m_\chi^2)\chi + \lambda\phi\chi^2, \tag{2.44}$$

we see that if we integrate the ϕ field out of the exponential of the action, we are left with

$$e^{-1/2(\chi K_\chi \chi) + \lambda^2(\chi K_\phi^{-1}\chi)^2/4}. \tag{2.45}$$

The extra λ^2 term above brings about a vacuum instability in the χ field. This extra term comes from completing the square in ϕ in the Lagrangian with the interacting term. To overcome this vacuum instability in the complete theory, we introduce another term, $\mathcal{L}_\mu = \mu\chi^4/4!$, where $\mu = 6\lambda^2/m_\phi^2$. The value of μ is chosen so that this term will always be greater than the exponentially increasing term above.

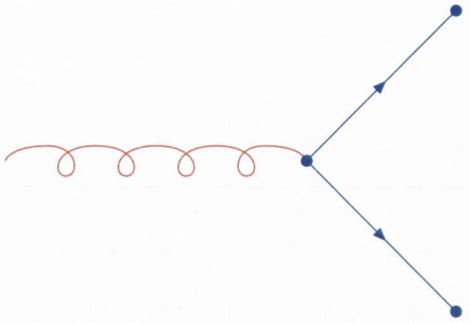

Figure 2-3: Feynman Diagram for the decay vertex.

2.2.2 Kinematics

Before investigating the energy spectrum, let us firstly examine the kinematics of such a system. For two identical, non-interacting bosons, with mass m, and spatial momentum $\vec{p}_1$, $\vec{p}_2$, in a brick-shaped box of volume $N_s^2 \times N_z$, the total energy of the system in the rest frame of the box, which we shall call the laboratory frame, is

$$E_L = \sqrt{\vec{p}_1^2 + m^2} + \sqrt{\vec{p}_2^2 + m^2} \tag{2.46}$$

The centre of mass frame is moving with velocity.

$$\vec{v} = \frac{\vec{P}}{E_L} \tag{2.47}$$

where $\vec{P}$ is the total momentum, $\vec{p}_1 + \vec{p}_2$. In this frame the energy is given by

$$\begin{aligned} E_{CM}^2 = E_L^2 - \vec{P}^2 &= \left[\sqrt{\vec{p}_1^2 + m^2} + \sqrt{\vec{p}_2^2 + m^2}\right]^2 - \vec{P}^2 \\ &= 2\sqrt{\vec{p}^{*2} + m^2} \end{aligned} \tag{2.48}$$

The momentum, $\vec{p}^*$ is related to the rest frame momenta by

$$\vec{p}^* = \hat{\gamma}(\vec{p}_1 - \vec{v}\sqrt{\vec{p}_1^2 + m^2}) = -\hat{\gamma}(\vec{p}_2 - \vec{v}\sqrt{\vec{p}_2^2 + m^2}) \tag{2.49}$$

where

$$\gamma = \frac{1}{\sqrt{1 - \hat{v}^2}} = \frac{E_L}{E_{CM}} \tag{2.50}$$

and

$$\hat{\gamma}\vec{p} = \gamma\vec{p}_{\parallel} + \vec{p}_{\perp}, \qquad \hat{\gamma}^{-1}\vec{p} = \gamma^{-1}\vec{p}_{\parallel} + \vec{p}_{\perp} \tag{2.51}$$

The parallel and perpendicular projections of $\vec{p}$ are given by $\vec{p}_{\parallel} = (\vec{p}.\vec{v})\vec{v}/v^2$ and $\vec{p}_{\perp} = \vec{p} - \vec{p}_{\parallel}$. Ref.[14] generalises Lüscher's method to the case where $\vec{P} \neq 0$. In our case, however, we will restrict ourselves to the $\vec{P} = 0$ case.

2.2.3 Parameters

Our theory has 3 parameters; m_ϕ, m_χ and λ. We are interested in energies, E, in the elastic region, $2m_\chi \leq E \leq 4m_\chi$. As we decrease m_χ, the lattice volumes we must examine before reaching an avoided level crossing increase. However, as we make m_χ heavier, the signal in the Monte Carlo simulations becomes weaker. Thus our aim is to make m_χ as large as possible without losing the signal critically. Since preliminary Monte Carlo simulations of the theory gave workable signals up to $Ea_t = 1.5$, we use this as our upper limit. This give us $m_\chi a_t = 0.375$. We subsequently choose $m_\phi a_t = 1$, where a_t is the temporal lattice spacing. For the coupling λ, we use a value of $\lambda a_t = 0.5$. This then gives us $\mu = 0.0625$.

As will be elucidated in subsequent chapters, the extraction of energy levels from Monte Carlo simulations depend on the limit

$$\lim_{t\to\infty} -\log \frac{C(t+1)}{C(t)} = E. \tag{2.52}$$

This limit is necessary to ensure that contributions from higher energy states are negligible. To allow N_t to be sufficiently large for this limit to hold, without critically slowing the simulation, we use temporally anisotropic lattices with $N_t \neq N_s$, as is discussed in Ref. [15].

Since our aim is to measure the finite volume spectrum, we must, at this point consider the range of volumes to be examined. If we were to use spatially isotropic hypercubes, $V = N_t \times N_s^3$, the computational workload would soon scale beyond our capabilities. To avoid this problem, we use brick shaped volumes, $V = N_t \times N_s^2 \times N_z$. This allows us to vary the spectrum without this scaling issue. This method has already been applied in Ref. [12], which examined the adjustments needed to the generalised Zeta function to account for the symmetries of these lattices. We will set $N_t = 40$ and $N_s = 5$, and vary N_z between these two values to give us the changing volume required. The subtleties arising in the energy spectrum and scattering phase shift from this choice of topology will be addressed in later chapters.

Thus, our lattice will have dimensions $N_t \times N_s^2 \times N_z$. In particular, for the Monte Carlo simulations, we set $N_t = 40$, $N_s = 5$ and vary N_z from 9 to 40.

2.3 Previous Studies

Since the publication of Ref. [9, 11, 16, 17] demonstrated how the finite energy spectrum was related to its infinite volume scattering phase shift, many studies have taken advantage of this result. In particular, Ref. [14] worked on a theory similar to ours, but with discrete values for the fields and included both the rest and non-rest frames. A similar non-rest frame study was examined in Ref. [18]. Ref. [19] investigated the application of this results to four dimensional ϕ^4 theory in the broken phase. Another study germane to our own was carried out by Ref. [12] into the extension of Lüscher's result to brick shaped volumes. In two dimensions, examinations of $O(3)$ nonlinear σ-model [20] and two coupled Ising spins [21] have been carried out. In Ref [22, 23], the result was applied to three dimensional QED. In recent years, Lüscher's method has been utilised in quenched QCD [24, 25, 26, 27, 28, 29, 30, 31, 32, 33, 34, 35].

Chapter 3

Perturbation Theory/MC Simulation of $\phi \to \chi\chi$

In this chapter, our aim is to discuss the methods used to examine the energy spectrum and, hence, the decay width of our scalar $\phi \to \chi\chi$ theory. The Maiani-Testa Theorem state that S-matrix elements, and hence decay widths, cannot be extracted from infinite-volume Euclidean-space Green functions, except at kinematic thresholds. As was demonstrated in the previous chapter, however, the information about the decay width in the Euclidean formulation is encoded in the finite volume energy spectrum, in particular, at the avoided level crossings, where two energy levels come close to contact (Fig. 3-1). The separation of the energy levels at this point is strongly linked to the mixing between the states at that point. We are especially interested in the crossings between the ϕ and $\chi\chi$ states. Therefore, in the Euclidean case, we are interested in mixing several states of the system, $\mathcal{O}$, together to evaluate the energy

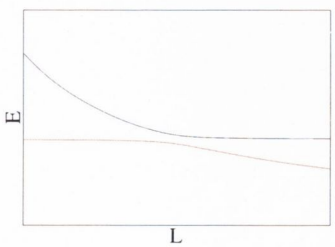

Figure 3-1: An avoided level crossing.

spectrum. To this end, we create a correlation matrix, $C_{\alpha\beta}$;

$$C_{\alpha\beta} = \langle \mathcal{O}_\alpha(t)^\dagger \mathcal{O}_\beta(0) \rangle. \tag{3.1}$$

We will talk in subsequent sections about the form these operators take and how they are calculated in the perturbative and Monte Carlo simulation cases. The mixing between states described above will be measured by the off-diagonal entries of this matrix.

Firstly, we use perturbation theory to obtain an analytic result using a truncated Taylor series in the exponential of the action. We expand each matrix element, $C_{\alpha\beta}$ in λ. In the Euclidean case, we then solve the matrix equation

$$\det C^{-1}(\Omega) = 0 \tag{3.2}$$

for the energy, Ω.

In the Minkowski case, we are unrestrained by the Maiani-Testa theorem and can gain direct access to the decay width from the individual correlation functions, without having to evaluate the entire correlation matrix.

Secondly, we approximate the exact result using Monte Carlo integration techniques. We diagonalise the correlation matrix and fit these eigenfunctions to

$$C(t) = Ae^{-Et}. \tag{3.3}$$

Once we have discussed the specifics of reaching our energy spectrum by each of these methods, we will then look at how, in each of these two cases, we get from this spectrum to the decay width of the ϕ field, Γ.

3.1 Perturbation Theory of Scalar Fields

The aim of our calculations in perturbation theory is to gain an understanding of what to expect from the Monte Carlo simulations and to provide support for those results. We use the Euclidean and Minkowski formulations of perturbation theory to achieve these ends in different ways. In the Euclidean case, we can use the correlation matrix to probe the energy spectrum and from there, the scattering phase shift. Since the

Maiani-Testa theorem, which limits the access to the decay width in the Euclidean case, does not affect the Minkowski case, we are able to calculate decay width directly from the $\phi \to \phi$ and $\chi\chi \to \chi\chi$ correlators individually.

In the discussion which follows, we will assume a Euclidean metric and comment on the differences arising in the Minkowski case where appropriate.

3.1.1 General Perturbation Theory

When dealing with a general theory of two scalar fields, ϕ and χ, we can write the Lagrangian of the system as

$$\mathcal{L} = \mathcal{L}_0 + \mathcal{L}_{int}$$

From here, we can write the action as the integral of the exponential of the system. We break this down into interacting and non-interacting parts.

$$\begin{aligned} S &= \int \mathcal{L} d^4x \\ &= S_0 + S_{int} \end{aligned} \tag{3.4}$$

$$S_0 = \int d^4x \frac{1}{2}(\phi(x) K_\phi \phi(x) + \chi(x) K_\chi \chi(x)) \tag{3.5}$$

where

$$K_{\phi,\chi} = -\partial^2 + m^2_{\phi,\chi} \tag{3.6}$$

At this point we introduce a generating functional;

$$\begin{aligned} W(p,q) &= \int \mathcal{D}\phi \mathcal{D}\chi e^{-S_0 + \phi p + \chi q} \\ &= \int \mathcal{D}\phi \mathcal{D}\chi e^{-\frac{1}{2}(\phi^T K_\phi \phi + \chi^T K_\chi \chi - \phi^T p - p^T \phi - \chi^T q - q^T \chi)} \\ &= \int \mathcal{D}\phi \mathcal{D}\chi e^{-\frac{1}{2}(\phi^T K_\phi \phi + \chi^T K_\chi \chi - p^T K_\phi^{-1} p - q^T K_\chi^{-1} q)} \\ &= \frac{1}{\sqrt{\det K_\phi \det K_\chi}} e^{\frac{1}{2}(p^T K_\phi^{-1} p + q^T K_\chi^{-1} q)} \end{aligned} \tag{3.7, 3.8}$$

From the original definition of $W(p,q)$, we can see that a general n-point function can be written in terms of derivatives of the generating functional.

$$\int \mathcal{D}\phi \mathcal{D}\chi \phi_{a_1} \dots \phi_{a_r} \chi_{b_1} \dots \chi_{b_s} e^{-S_0} = \left. \frac{\partial W(p,q)}{\partial p_{a_1} \dots \partial p_{a_r} \partial q_{b_1} \dots \partial q_{b_s}} \right|_{p,q=0} \tag{3.9}$$

Next, we expand the interacting part of the action, S_{int}, in terms of the coupling, λ.

$$\int \mathcal{D}\phi\mathcal{D}\chi e^{-S_{int}} = \left[\sum_{n=0}^{\infty} \frac{1}{n!} \left(-S_{int}\left(\frac{\partial}{\partial p}, \frac{\partial}{\partial q}\right)\right)^n W(p,q)\right]_{p=q=0} \tag{3.10}$$

Replacing this in the n-point function, we eventually have

$$\begin{aligned} &\int \mathcal{D}\phi\mathcal{D}\chi\phi_{a_1}\dots\phi_{a_r}\chi_{b_1}\dots\chi_{b_s}e^{-S} \\ &= \textstyle\sum_{n=0}^{\infty} \frac{1}{n!} \left[\frac{\partial}{\partial p_{a_1}\dots\partial p_{a_r}\partial p_{b_1}\dots\partial p_{b_s}} \left(-S_{int}\left(\frac{\partial}{\partial p}, \frac{\partial}{\partial q}\right)\right)^n W(p,q)\right]_{p=q=0} \end{aligned} \tag{3.11}$$

. If our coupling, λ is small, we truncate this expansion at order λ^2.

In the Minkowski case, the important results become

$$K_{\phi,\chi} = -\partial_0^2 + \partial_i^2 - m_{\phi,\chi}^2, \tag{3.12}$$

$$W(p,q) = \int \mathcal{D}\phi\mathcal{D}\chi e^{iS_0 + i\phi p + i\chi q} \tag{3.13}$$

$$= \frac{1}{\sqrt{\det K_\phi \det K_\chi}} e^{\frac{-i}{2}(p^T K_\phi^{-1} p + q^T K_\chi^{-1} q)} \tag{3.14}$$

$$\begin{aligned} &\int \mathcal{D}\phi\mathcal{D}\chi\phi_{a_1}\dots\phi_{a_r}\chi_{b_1}\dots\chi_{b_s}e^{iS} \\ &= \textstyle\sum_{n=0}^{\infty} \frac{1}{n!} \left[\frac{(-i)^{r+s}\partial}{\partial p_{a_1}\dots\partial p_{a_r}\partial p_{b_1}\dots\partial p_{b_s}} \left(iS_{int}\left(-i\frac{\partial}{\partial p}, -i\frac{\partial}{\partial q}\right)\right)^n W(p,q)\right]_{p=q=0} \end{aligned} \tag{3.15}$$

At this juncture, we have a general formula from which we can evaluate the n-point function for a general $\mathcal{L}_{int}$. We now need to specify our interaction Lagrangian to investigate the case we are interested in.

Object	Euclidean	Minkowski
ϕ Propagator	$\frac{1}{\vec{p}^2+p_0^2+m_\phi^2}$	$\frac{i}{p_0^2-\vec{p}^2-m_\phi^2+i\epsilon}$
χ Propagator	$\frac{1}{\vec{p}^2+p_0^2+m_\chi^2}$	$\frac{i}{p_0^2-\vec{p}^2-m_\chi^2+i\epsilon}$
$\phi\chi^2$ Vertex	λ	λ
χ^4 Vertex	$\mu/4!$	$\mu/4!$

Table 3.1: Feynman rules for the model scalar field theory.

3.1.2 Scalar $\phi \to 2\chi$ Theory

Now we restrict our attention to the special case. We examine a theory of two scalar fields, ϕ and χ, in which the ϕ field decays into two χ fields. We also require that $m_\phi > 2m_\chi$. In this case our interaction Lagrangian is given by

$$\mathcal{L}_{int} = \lambda\phi\chi^2 + \frac{\mu}{4!}\chi^4 \tag{3.16}$$

We now write down the Feynman rules for this specific theory (Table 3.1).

We impose momentum conservation at each vertex, integrate over each undetermined momentum and divide by the symmetry factor of the diagram.

3.1.3 Lattice Form of the Feynman Propagator

In this subsection, we assume a Euclidean formulation and follow the argument in [36]. As mentioned above, the operators K_ϕ and K_χ are given by

$$K_{\phi,\chi} = -\partial^2 + m_{\phi,\chi}^2. \tag{3.17}$$

For our numerical calculations, we will need a latticised version of these operators, and in particular, their inverses. As we will see later, we will require our temporal Fourier component to be continuous. We are, however, interested in the finite spacial volume properties of the theory. So, while we regard the time direction to be of infinite extent in a continuous variable, the spatial dimensions have finite extent in discrete latticised variables. Rewriting $K_{\phi,\chi}$ in this way, we see that

$$K(\vec{n},\vec{m})_{\phi,\chi} = -\partial_0^2 - \sum_{i=1}^{3}(\delta_{\vec{n}+\hat{i},\vec{m}} + \delta_{\vec{n}-\hat{i},\vec{m}} - 2\delta_{\vec{n}\vec{m}}) + m_{\phi,\chi}^2\delta_{\vec{n}\vec{m}} \tag{3.18}$$

where $\hat{i}$ is the unit vector in the i direction. The indices, $\vec{m}$ and $\vec{n}$, label the sites of the discrete spatial lattice. To find the inverse of this operator, we must look at its Fourier Transform. By translational invariance, the spatial part will be diagonal.

$$\begin{aligned}
\tilde{K}_{\phi,\chi}(\vec{k},k_0) &= \sum_{n,m}\int \frac{dt\,dt'}{(2\pi)^2}\left[-\partial_0^2 - \sum_{i=1}^{3}(\delta_{\vec{n}+\hat{i},\vec{m}} + \delta_{\vec{n}-\hat{i},\vec{m}} - 2\delta_{\vec{n}\vec{m}}) + m^2_{\phi,\chi}\delta_{\vec{n}\vec{m}}\right] \\
&\quad \times e^{i\vec{k}(\vec{n}-\vec{m})}e^{ik_0(t'-t)} \\
&= k_0^2 - \sum_{i=1}^{3}(e^{ik_i} + e^{-ik_i} - 2) + m^2_{\phi,\chi} \\
&= k_0^2 - 2\sum_{i=1}^{3}(\cos(k_i) - 1) + m^2_{\phi,\chi} \\
&= k_0^2 + 4\sum_{i=1}^{3}\left(\sin^2\frac{k_i}{2}\right) + m^2_{\phi,\chi} \qquad (3.19) \\
&= \tilde{K}(k)_{\phi,\chi}
\end{aligned}$$

The conventions regarding Fourier Transforms are the same as those followed in [37].

The diagonal nature of the spacial components of the Fourier Transform gives great benefit to performing the numerical calculations in momentum space. Thus, we can reduce a problem of size N^3, where N is the number of points in each direction of the lattice, to a problem of size N. These latticised propagators will form the building blocks of the operators used to form the correlation matrix.

3.1.4 A First Approximation

The standard method for calculating a decay width is to calculate the renormalised masses and couplings directly using perturbation theory as described in Ref. [37] and to use these to find the value of Γ. The decay width, Γ, depends only on the renormalised masses and couplings;

$$\Gamma = \frac{\lambda_R^2}{8\pi m_\phi^2}\sqrt{m_\phi^2 - 4m_\chi^2} \qquad (3.20)$$

The idea is to calculate the renormalised masses and couplings directly using perturbation theory, and to use these to find the value of Γ.

Mass Renormalisations

The Fourier Transform of the two point function can be written as

$$\begin{aligned}\int d^4x \langle\Omega|T\phi(x)\phi(0)|\Omega\rangle e^{ipx} &= \frac{1}{p^2 - m_{\phi_0}^2} + \frac{1}{p^2 - m_{\phi_0}^2}\Sigma_\phi \frac{1}{p^2 - m_{\phi_0}^2} + \ldots \\ &= \frac{1}{p^2 - m_{\phi_0}^2 - \Sigma_\phi}\end{aligned} \tag{3.21}$$

This full propagator has a pole at the physical mass, m_ϕ, which is the solution to the equation

$$[p^2 - m_{\phi_0}^2 - \Sigma_\phi(p)]|_{p^2=m_\phi^2} = 0. \tag{3.22}$$

The object, $\Sigma_\phi(p)$ is the sum of all one particle irreducible diagrams with two external ϕ propagators. This is simply a $\chi\chi$ loop diagram;

$$\Sigma_\phi(p) = \lambda^2 \int \frac{d^4k}{(2\pi)^4} \frac{1}{k^2 - m_{\chi_0}^2} \frac{1}{(p-k)^2 - m_{\chi_0}^2} \tag{3.23}$$

The same technique can be used to evaluate $\langle\Omega|T\chi(x)\chi(0)|\Omega\rangle$. In this case, $\Sigma_\chi(p)$ has contributions from both the $\phi\chi^2$ and the χ^4 terms;

$$\Sigma_\chi(p) = \lambda^2 \int \frac{d^4k}{(2\pi)^4} \frac{1}{k^2 - m_{\chi_0}^2} \frac{1}{(p-k)^2 - m_{\phi_0}^2} + \frac{\mu}{2} \int \frac{d^4k}{(2\pi)^4} \frac{1}{k^2 - m_{\chi_0}^2} \tag{3.24}$$

While $\Sigma_\phi(p)$ and $\Sigma_\chi(p)$ are logarithmically divergent in the continuum, they can be evaluated numerically using the lattice regularisation, described previously. Solving Eq. 3.22 and the equivalent equation for the χ field, we obtain values for the renormalised masses in Eq. 3.20. The only other input in this formula is the renormalised coupling, λ_R.

Coupling Renormalisations

Again, looking at $\langle\Omega|T\phi(x)\phi(0)|\Omega\rangle$, we see that

$$\begin{aligned}\int d^4x \langle\Omega|T\phi(x)\phi(0)|\Omega\rangle e^{ipx} &= \frac{1}{p^2 - m_{\phi_0}^2} + \frac{1}{p^2 - m_{\phi_0}^2}\Sigma_\phi \frac{1}{p^2 - m_{\phi_0}^2} + \ldots \\ &= \frac{1}{p^2 - m_{\phi_0}^2} \frac{1}{1 - \Pi(p^2)}\end{aligned} \tag{3.25}$$

where

$$\Pi(p^2) = \frac{1}{p^2 - m_{\phi_0}^2} \int \frac{d^4k}{(2\pi)^4} \frac{1}{k^2 - m_{\chi_0}^2} \frac{1}{(p-k)^2 - m_{\phi_0}^2} \tag{3.26}$$

The residue of the $p^2 - m_{\phi_0}^2 = 0$ pole is

$$Z_3 = \frac{1}{1 - \Pi(m_\phi^2)} \tag{3.27}$$

The amplitude for any low momentum scattering process will be shifted by this factor. Since any diagram of this form has a factor of λ^2 attached to it, we can account for this shift by making the substitution $\lambda \to \sqrt{Z_3}\lambda$, giving us our renormalised coupling λ. While a similar calculation can be carried out for the renormalisation of μ, this is not necessary for our evaluation of Eq. 3.20. The methods outlined above can be used to calculate all the mass and coupling renormalisations needed to evaluate Γ using Eq. 3.20.

3.1.5 Operators and Correlators in Perturbation Theory

As will be discussed in the coming sections, the energy spectrum and decay width in perturbation theory are, in both the Minkowski and Euclidean formulations, linked to correlation functions of operators. We now investigate the operators we will use to form the correlators in perturbation theory, their functional form and the contributions from the various Feynman diagrams of the $\phi \to \chi\chi$ theory. The correlation matrix is given by

$$C_{ij} = \int \mathcal{D}\phi\mathcal{D}\chi e^{-S}\langle\Phi_i|\Phi_j\rangle \tag{3.28}$$

where

$$|\Phi_0\rangle = \int e^{-i\vec{p}\vec{x}}\phi(\vec{x},t)d^3x \tag{3.29}$$

$$\langle\Phi_0| = \int e^{i\vec{p}\vec{x}}\phi(\vec{x},t)d^3x \tag{3.30}$$

and

$$|\Phi_i\rangle = \int e^{-i(\vec{p_i}\vec{x_1}-\vec{p_i}\vec{x_2})}\chi(\vec{x_1},t)\chi(\vec{x_2},t)d^3x_1d^3x_2 \tag{3.31}$$

$$\langle\Phi_i| = \int e^{i(\vec{p_i}\vec{x_1}-\vec{p_i}\vec{x_2})}\chi(\vec{x_1},t)\chi(\vec{x_2},t)d^3x_1d^3x_2 \tag{3.32}$$

Expanding to order λ^2 using the Feynman rules prescribed, we must evaluate nine Feynman diagrams in all. Firstly we have the two free diagrams. We then have five diagrams from the $\phi\chi^2$ term in the action. Three of these appear in the $\chi\chi \to \chi\chi$

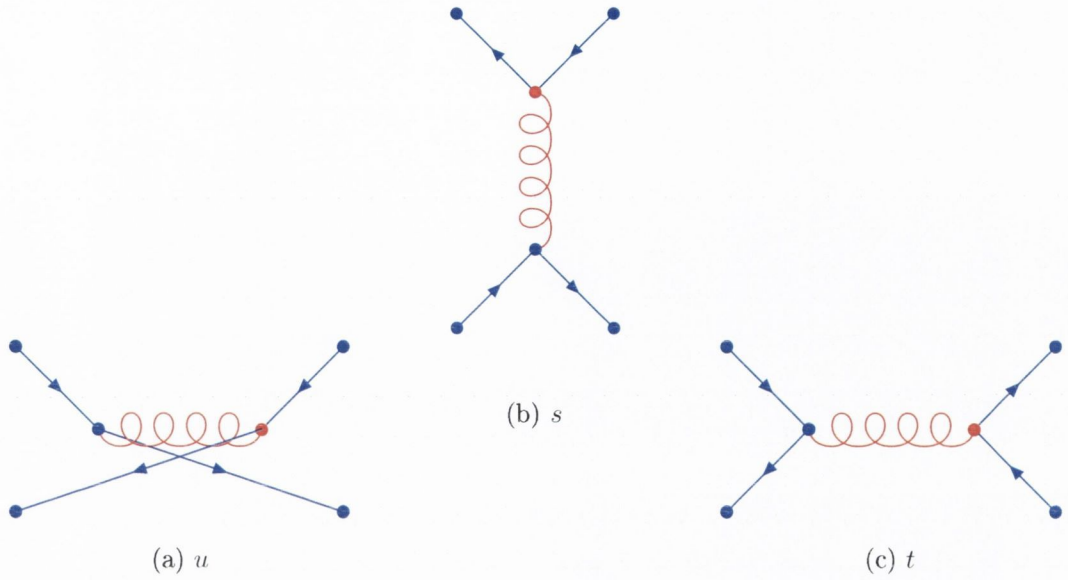

(a) u (b) s (c) t

Figure 3-2: $\chi\chi \to \chi\chi$ Channels in $\phi\chi^2$.

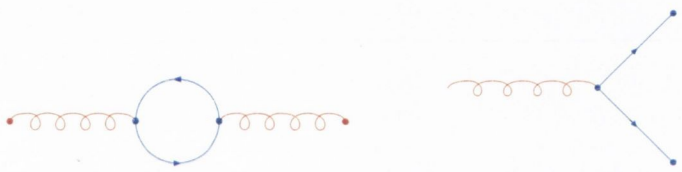

(a) $\phi \to \phi$ loop (b) $\phi \to \chi\chi$ scattering

Figure 3-3: Other diagrams from $\phi\chi^2$ term.

expansion (Fig. 3-2), and one each in the $\phi \to \phi$ and $\phi \to \chi\chi$ expansions (Fig. 3-3). There are two further contributions to the $\chi\chi \to \chi\chi$ channel coming from the χ^4 term (Fig. 3-4).

It is fortuitous that the coupling in the χ^4 term, μ, should be proportional to λ^2. This greatly simplifies the contribution from that term.

For the sake of example, let us calculate the $\phi \to \phi$ correlator. Since it will be of particular interest to us later, we will use a Minkowski formulation.

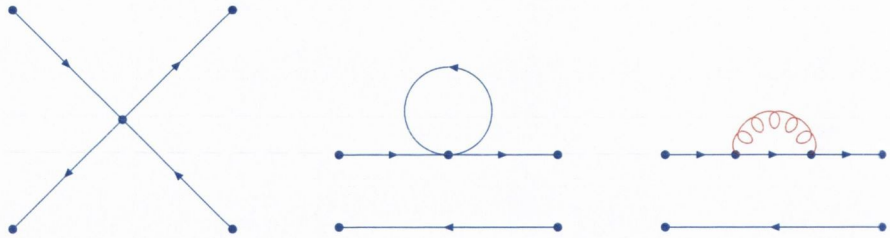

(a) cross (b) epaulette (c) sunrise

Figure 3-4: Diagrams from χ^4.

$$\begin{aligned} c(t) &= c_0(t) + \lambda^2 c_2(t) \\ &= \int d\Omega \tilde{K}_\phi^{-1}(\Omega,0) e^{i\Omega(t-t')} + \lambda^2 \int d\omega_i \tilde{K}_\phi^{-1}(\omega_1,0) \sum_{\vec{k}} \tilde{K}_\phi^{-1}(\omega_4,0) \\ &\quad \times \tilde{K}_\chi^{-1}(\omega_2,\vec{k}) \tilde{K}_\chi^{-1}(\omega_3,-\vec{k}) \delta(\omega_1-\omega_2+\omega_3)\delta(\omega_2-\omega_3-\omega_4) e^{i(\omega_4 t-\omega_1 t')} \\ &= \int d\Omega \left[\tilde{K}_\phi^{-1}(\Omega,0) + \lambda^2 \tilde{K}_\phi^{-1}(\Omega,0) \right. \\ &\quad \left. \times \int d\omega \sum_{\vec{k}} \tilde{K}_\chi^{-1}(\omega,\vec{k}) \tilde{K}_\chi^{-1}(\Omega-\omega,-\vec{k}) \tilde{K}_\phi^{-1}(\Omega,0) \right] e^{i\Omega(t-t')} \end{aligned} \tag{3.33}$$

As we will see, our interest lies in the poles of $c(t)$, or in solving the equation $c^{-1}(t) = 0$. Dropping the integral over the total momentum, we are left solving an equation of the form $f(\Omega) = 0$.

$$\begin{aligned} 0 &= \left[\tilde{K}_\phi^{-1}(\Omega,0) + \lambda^2 \tilde{K}_\phi^{-1}(\Omega,0) \int d\omega \sum_{\vec{k}} \tilde{K}_\chi^{-1}(\omega,\vec{k}) \tilde{K}_\chi^{-1}(\Omega-\omega,-\vec{k}) \tilde{K}_\phi^{-1}(\Omega,0) \right]^{-1} \\ &\approx \tilde{K}_\phi(\Omega,0) - \lambda^2 \int d\omega \sum_{\vec{k}} \tilde{K}_\chi^{-1}(\omega,\vec{k}) \tilde{K}_\chi^{-1}(\Omega-\omega,-\vec{k}) \\ &= \tilde{K}_\phi(\Omega,0) - \lambda^2 L_\phi(\Omega) \end{aligned} \tag{3.34}$$

where

$$L_\phi(\Omega) = \int d\omega \sum_{\vec{k}} \tilde{K}_\chi^{-1}(\omega,\vec{k}) \tilde{K}_\chi^{-1}(\Omega-\omega,-\vec{k}). \tag{3.35}$$

Thus, the solution to $c^{-1}(\Omega) = 0$ we are looking for will have an order λ^2 correction to the free solution, related to the $\chi\chi$ loop; $\Omega = m_\phi + \mathcal{O}(\lambda^2)$.

The description given in Eq. 3.45 for the determinant of the correlation matrix does make some restrictions about which diagrams are included. Let us examine, in particular, a typical $\chi\chi \to \chi\chi$ term in the expansion. We write the interaction terms as a sum of terms, such as the cross and t-channels, which can be factored into products involving two powers of the free $\chi\chi$ propagator, c_0, one power of c_0, such as the epaulette and sunrise terms and those which cannot be factored in c_0, like the u- and s-channels;

$$\begin{aligned} 0 &= \left\{c_0(\omega) + \lambda^2[c_0(\omega)c_2(\omega)c_0(\omega) + c_0(\omega)\hat{c}_2(\omega) + \tilde{c}_2(\omega)]\right\}^{-1} \\ &\approx c_0^{-1}(\omega) - \lambda^2[c_2(\omega) + c_0(\omega)^{-1}\hat{c}_2(\omega) + c_0^{-1}(\omega)\tilde{c}_2(\omega)c_0^{-1}(\omega)]. \end{aligned} \tag{3.36}$$

Since the solution to this equation will have an order λ^2 correction to the free solution, we see that $c_0(\omega)^{-1} = 0$ to first order (and $\tilde{c}_2^{-1}(\omega) \neq 0$ and $\hat{c}_2^{-1}(\omega) \neq 0$). Thus, we have

$$c_0^{-1}(\omega)\tilde{c}_2(\omega)c_0^{-1}(\omega) = 0 \tag{3.37}$$

and

$$c_0^{-1}(\omega)\hat{c}_2(\omega) = 0 \tag{3.38}$$

to order λ^2. This leaves us with

$$c_0^{-1}(\omega) - \lambda^2 c_2(\omega) = 0. \tag{3.39}$$

This analysis discounts contributions from u and s channel scattering and also the so-called epaulette and sunrise terms. The $\phi \to \phi$ case is unaffected. At this point, we should pin down what is meant by the free $\chi\chi$ propagator. Appearing in Eq. 3.45 as C_{ii_0} for $i > 0$, this important object is given by (in the Euclidean metric)

$$\begin{aligned} c_{ii_0} &= \int d\omega \frac{1}{-\omega^2 + \vec{p_i}^2 + m_\chi^2} \frac{1}{-(\Omega - \omega)^2 + \vec{p_i}^2 + m_\chi^2} \\ &= \frac{2\pi}{\Omega\sqrt{\vec{p_i}^2 + m_\chi^2}} \frac{1}{(2i\sqrt{\vec{p_i}^2 + m_\chi^2} - \Omega)} \end{aligned} \tag{3.40}$$

Now that we have examined the operators which we will use to form the correlation matrix, and considered some of the issues involved in the individual correlators, we move on to describe the correlation matrix.

3.1.6 Euclidean Correlation Matrix and the Energy Spectrum

In the Euclidean case, the relationship between the correlation matrix and the energy is greatly simplified by the purely imaginary nature of the poles of the determinant of the correlation matrix. This is a consequence of the Maiani-Testa Theorem [8]. As we have demonstrated, the correlator, and hence the determinant of the correlation matrix can be written as

$$\det C_{\alpha\beta}(t) = \int f(\Omega) e^{i\Omega t} d\Omega. \tag{3.41}$$

Now suppose $f(\Omega)$ has a simple pole at Ω_p. Since the poles in the Euclidean case are purely imaginary, we can assume that $\Omega_p = i\omega$. (On the other hand, the poles in the Minkowski case will not be purely real. This will complicate the analysis but give us direct access to the decay width). Performing this integral over Ω, we see that

$$\det C_{\alpha\beta}(t) \propto e^{-\omega t}. \tag{3.42}$$

But spectral decomposition of $\det C_{\alpha\beta}(t)$ says that

$$\det C_{\alpha\beta}(t) = \sum_n z_n e^{-E_n t}. \tag{3.43}$$

Hence, the energy levels of the system can be retrieved from the poles of the determinant of the correlation matrix, or equivalantly, the zeroes of its inverse, by solving

$$\det C^{-1}(\Omega) = 0 \tag{3.44}$$

where Ω is the energy of the system.

To order λ^2, the determinant of the inverse correlation matrix with one ϕ state and $n-1$ $\chi\chi$ states is given by

$$\begin{aligned} \det C^{-1}(\Omega) &= \begin{vmatrix} C_{00_0} + \lambda^2 C_{00_2} & \lambda C_{01} & \lambda C_{02} & \cdots \\ \lambda C_{10} & C_{11_0} + \lambda^2 C_{11_2} & 0 & \\ \lambda C_{20} & 0 & C_{22_0} + \lambda^2 C_{22_2} & \\ \vdots & & & \end{vmatrix}^{-1} \\ &\approx \prod_{i=0}^{m} (C_{ii_0}^{-1} - \lambda^2 C_{ii_2}) + \lambda^2 \sum_{i=1}^{n} C_{0i}^2 \cdot \prod_{k=0}^{n} C_{kk_0}^{-2} \end{aligned} \tag{3.45}$$

Although there are contributions from the $\chi\chi(\vec{p}) \to \chi\chi(\vec{p'} \neq \vec{p})$ at order λ^2, when the determinant is expanded, these terms only appear in higher order corrections, and are thus neglected.

3.1.7 Energy and Decay Widths in Minkowski Perturbation Theory

In terms of the S matrix, the Jost function, related to the regular solution to the radial Schrödinger equation, $\mathcal{F}(p)$ is given by

$$c(p) = \frac{\mathcal{F}(-p)}{\mathcal{F}(p)}. \tag{3.46}$$

Since $\mathcal{F}(p)$ is analytic on $\Im p < 0$, and $\mathcal{F}(\pm p)$ cannot vanish at the same point, the Jost function vanishes if and only if the S matrix has a pole. Thus there is complete equivalence between the zeroes of the Jost function and the poles of the S matrix. We assume the Jost function is zero for some $\bar{p} = p_R - ip_I$. When we consider the Jost function as a function of E, the mapping from p to E is a two to one function. This means that the Jost function is a function on a two-sheeted Riemann surface. The first sheet is the $\Im p > 0$ half plane and the second sheet is the $\Im p < 0$ half plane. The bound states are given by the zeroes of $\mathcal{F}(p)$ on the imaginary axis p lie on the negative real axis of the first sheet of E. The resonance zero at $\bar{p} = p_R - ip_I$ is a zero on the second sheet given by

$$E = E_R - \frac{i\Gamma}{2}. \tag{3.47}$$

Thus, in the Minkowski case, we can access the decay width directly from the imaginary part of E. (For a detailed account of this explanation, see [38].)

Correlators in the Minkowski Case

In the Minkowski case, access to the S-matrix, and hence, the decay width, is subject to no restrictions from the Maiani-Testa Theorem. Thus rather than concentrate on the entire correlation matrix, as in the Euclidean case, we can gain access to the decay width directly from the $\phi \to \phi$ and $\chi\chi \to \chi\chi$ correlation functions. We will initially consider the $\chi\chi \to \chi\chi$ correlators, followed by the more intricate $\phi \to \phi$

correlator. For convenience sake, we will carry over the notation from the Euclidean correlation function, using the superscript, M, to denote the Minkowski formulation. In the Minkowski formulation, the $\chi\chi \to \chi\chi$ correlator, C_{ii}^M, $\quad i \neq 0$, is given by

$$\begin{aligned} C_{ii}^M(\Omega)^{-1} &= \left[\int d\omega \frac{1}{-\omega^2 - \vec{p_i}^2 - m_\chi^2} \frac{1}{(\Omega-\omega)^2 - \vec{p_i}^2 - m_\chi^2} - \frac{\lambda^2}{N_s^2 N_z} \frac{1}{\Omega^2 - m_\phi^2} + \mu \right]^{-1} \\ &\approx \Omega\sqrt{\vec{p_i}^2 + m_\chi^2}(2\sqrt{\vec{p_i}^2 + m_\chi^2} - \Omega) - \frac{\lambda^2}{N_s^2 N_z} \frac{1}{\Omega^2 - m_\phi^2} + \mu. \end{aligned} \tag{3.48}$$

As before, the subscript, i, refers to the ith $\chi\chi$ state. The two contributions to the interaction come from the cross and t channels, as discussed previously. The factor of $1/N_s^2 N_z$ in the cross channel comes from an extra integration over an undetermined momentum in that channel. The energy and decay width can be evaluated numerically by solving $C_{ii}^M(\Omega)^{-1} = 0$. The case can be solved simply using the numerical method outlined below. Any imaginary part developed in this expression relates to the decay width, $\Gamma_{\chi\chi}$, of the $\chi\chi$ state in a ϕ state. At kinematic thresholds, when $E_{\chi\chi} \sim E_\phi$, we expect this decay width to open up.

The $\phi \to \phi$ correlator, C_{00}^M, requires a more subtle approach, due to the $\chi\chi$ loop diagram. We will follow the method used in [39], adapted to three infinite, continuous and one finite, discretised dimensions. We will consider the temporal direction and the x and y directions to be of infinite extent, and set the length of the z direction to be N_Z. This will reduce the integral over the momentum in that direction to a sum over possible momenta given by $2n\pi/N_z, n \in N$. The correction to the ϕ correlator from the $\chi\chi$ loop is given by

$$\begin{aligned} \Pi(p^2) &= \frac{\lambda^2}{N_Z} \sum_{k_z} \sum_{k_z'} \int \frac{d^3k}{(2\pi)^3} \frac{d^3k'}{(2\pi)^3} \frac{1}{k^2 + m_\chi^2 - i\epsilon} \frac{1}{k'^2 + m_\chi^2 - i\epsilon} \delta(k + k' - p) \\ &= \frac{\lambda^2}{N_Z} \sum_{k_z} \int \frac{d^3k}{(2\pi)^3} \frac{1}{k^2 + m_\chi^2} \frac{1}{(k+p)^2 + m_\chi^2} \\ &= \frac{\lambda^2}{N_Z} \sum_{k_z} \int_0^1 dx \int \frac{d^3k}{(2\pi)^3} \frac{1}{[x(m_\chi^2 + (k+p)^2 + (1-x)(m_\chi^2 + k^2)]^2} \\ &= \frac{\lambda^2}{N_Z} \sum_{k_z} \int_0^1 dx \int \frac{d^3k}{(2\pi)^3} \frac{1}{[(k+xp)^2 + p^2(1-x)x + m_\chi^2]^2} \\ &= \frac{\lambda^2}{N_Z} \sum_{k_z} \int_0^1 dx \int \frac{d^3q}{(2\pi)^3} \frac{1}{(q^2 + D)^2} \end{aligned} \tag{3.49}$$

where $D = x(1-x)p^2 + m_\chi^2 + k_z^2 = x(1-x)p^2 + R^2$ and $q = \check{k} - xp$. We define $\check{k} = (k_t, k_x, k_y)$ to be the three vector containing the components of k in the dimensions of infinite extent. Using the general formula

$$\int d^d q (2\pi)^d \frac{(q^2)^a}{(q^2+D)^b} = \frac{\Gamma(b-a-d/2)\Gamma(a+d/2)}{(4\pi)^{d/2}\Gamma(b)\Gamma(d/2)} D^{-(b-a-d/2)}, \tag{3.50}$$

we see that

$$\Pi(p^2) = \frac{\lambda^2}{N_Z} \sum_{k_z} \frac{\Gamma(-1+(\kappa-2)/2)}{(4\pi)^{3-(\kappa-3)/2}\Gamma(2)} \int_0^1 dx \frac{1}{D^{1/2}} \frac{1}{D^{\kappa/2}} - Ak^2 - Bm_\chi^2. \tag{3.51}$$

The dimension, κ, is given by $\kappa = 3 - d$, and examine the $\kappa \to 0$ limit. Using

$$A^{\kappa/2} = 1 + \frac{\kappa}{2} \log_e A \tag{3.52}$$

and

$$\Gamma(z) \approx \frac{2^z}{z}(1+z)^{-1} \tag{3.53}$$

we see that

$$\Pi(p^2) = \frac{12\sqrt{2}\lambda^2}{N_Z(4\pi)^{3/2}} \sum_{k_z} \int_0^1 dx \frac{1}{D^{1/2}} \log_e \left(\frac{D}{4\pi}\right). \tag{3.54}$$

Our interest is in the imaginary part of $\Pi(p^2)$, since it corresponds to the decay width, Γ. When the particles are above threshold (i.e.. $p^2 < 4R^2$), the value of x is negative and $\Im \log_e D = i\pi$, contributing an imaginary part to $\Pi(p^2)$. This happens over the range $x_- < x < x_+$, where $x_\pm = 1/2 \pm 1/2(1+R^2/p^2)^{1/2}$. R is related to the spatial momentum $\vec{k}$ of the χ particles by $\sqrt{\vec{k}^2 + m_\chi^2}$. Integrating over this range, we see that

$$\begin{aligned}
\Im\Pi(p^2) &= \frac{6\lambda^2}{N_Z(4\pi)^{3/2}} \sum_{k_z} \int_{x_-}^{x_+} \frac{1}{D^{1/2}} dx \\
&= \frac{6\lambda^2}{N_Z(4\pi)^{3/2}} \sum_{k_z} \frac{i}{p} \left[\log_e \left(ip\sqrt{1+\frac{4R^2}{p^2}} \right) \right. \\
&\quad \left. - \log_e \left(2\sqrt{2} - ip\sqrt{1+\frac{4R^2}{p^2}} \right) \right] \qquad (3.55) \\
\Rightarrow \Im\Pi(-m_\phi^2) &= \frac{6\lambda^2}{N_Z(4\pi)^{3/2}} \sum_{k_z} \frac{1}{m_\phi} \left[\log_e \left(m_\phi\sqrt{1-\frac{4R^2}{m_\phi^2}} \right) \right. \\
&\quad \left. - \log_e \left(2\sqrt{2} - m_\phi\sqrt{1-\frac{4R^2}{m_\phi^2}} \right) \right] \qquad (3.56)
\end{aligned}$$

Now, introducing a Heaviside step function when summing over all possible values of $R^2(\vec{k}) = \vec{k}^2 + m_\chi^2$ around the loop, we see that

$$\Gamma = \frac{12\lambda^2}{N_Z(4\pi)^{3/2}} \sum_{k_z} \frac{1}{m_\phi} \left[\log_e \left(m_\phi \sqrt{1 - \frac{4R^2}{m_\phi^2}} \right) - \log_e \left(2\sqrt{2} + m_\phi \sqrt{1 - \frac{4R^2}{m_\phi^2}} \right) \right] \theta(m_\phi - 2R(\vec{k})). \tag{3.57}$$

Here, we have collected a factor of 2 from the definition $\Gamma = 2\Im\Pi(p^2)$.

Numerical Complex Root Finding

We have demonstrated how we are confronted with a simple complex root finding problem. To solve this we use Müller's method [40]. This is an iterative method similar to the secant method. At each step it makes a quadratic approximation of the function, $f(x)$. It then updates the system by

$$x_{k+1} = x_k - \frac{2f(x_k)}{\omega \pm \sqrt{\omega^2 - f(x_k) f[x_k, x_{k-1}, x_{k-2}]}} \tag{3.58}$$

where ω and $f[x_k, x_{k-1}, x_{k-2}]$ are divided differences representing first and second derivatives respectively.

$$\omega = f[x_k, x_{k-1}] + f[x_k, x_{k-2}] - f[x_{k-1}, x_{k-1}] \tag{3.59}$$

and

$$\begin{aligned} f[x_k, x_{k-1}, x_{k-2}] &= \frac{f[x_{k-1}, x_{k-2}] - f[x_k, x_{k-1}]}{x_{k-2} - x_k} \\ &= \frac{1}{x_{k-2} - x_k} \left[\frac{f(x_{k-2}) - f(x_{k-1})}{x_{k-2} - x_{k-1}} - \frac{f(x_{k-1}) - f(x_k)}{x_{k-1} - x_k} \right] \end{aligned} \tag{3.60}$$

given

$$f[x, y] = \frac{f(y) - f(x)}{y - x} \tag{3.61}$$

The presence of the square root in the denominator allows for the existence of complex roots, which would not be found by an algorithm like the secant method, which makes a linear, rather than quadratic approximation. Also, this method does not require evaluation of the derivative as is the case in the Newton-Raphson method,

for instance. This is beneficial in this case, where the function is are complicated and calculation of the derivative would be numerically expensive. Other than iterative overheads, the Muller method requires only one function evaluation per iteration. The order of convergence of Müller's method is approximately 1.84. Thus it makes more progress per iteration than the secant method (1.62), but less than Newton-Raphson (2).

Having examined the form of the correlation matrix in the Euclidean formulation and the calculation of the decay width in the Minkowski case perturbatively to order λ^2, we will now study the estimation of the correlation matrix using Markov Chain Monte Carlo integration techniques.

3.2 Monte Carlo Simulation of Correlation Matrix

As was discussed previously, in the context of Euclidean perturbation theory, to gain the mixing of states to properly describe the avoided level crossings, the object of interest in the Monte Carlo simulations of the model $\phi \rightarrow \chi\chi$ theory is the correlation matrix

$$C^0_{ab}(t) = \langle \mathcal{O}_{0,a}(t)^\dagger \mathcal{O}_{0,b}(0) \rangle \tag{3.62}$$

where the operators $\mathcal{O}_{0,a}(t)$, represent the ϕ and $\chi\chi$ states. Previously, when calculating matrix elements, we expanded the exponential in the action to order λ^2. We could then evaluate the matrix exactly to order λ^2 up to some momentum cut-off governed by the lattice spacing, a. Monte Carlo simulation provides us with a tool to estimate the elements of this matrix non-perturbatively, up to some statistical error.

3.2.1 Correlation Matrix

When evaluating the matrix elements, C_{ab}, we, in fact, want to measure the vacuum subtracted correlation function;

$$C_{ab}(t) = \frac{1}{Z} \int \mathcal{D}\phi \mathcal{D}\chi e^{-S} \langle \Phi_a | \Phi_b \rangle - \int \mathcal{D}\phi \mathcal{D}\chi e^{-S} \langle \Phi_a \rangle \int \mathcal{D}\phi \mathcal{D}\chi e^{-S} \langle \Phi_b \rangle \tag{3.63}$$

To calculate these integrals, we perform Markov Chain Monte Carlo integrations with fixed point e^{-S}/Z. At each iteration, once we have the field thermalised at the fixed point, we construct the creation and annihilation operators by summing up all the values of the field on a given time-slice. The value of the integrals is evaluated over many field ensembles. We would like to include operators, firstly, in which the χ fields have equal and opposite momentum, $\vec{p}$, and also the case where the ϕ field has some momentum, $\vec{P}$. Since we are only interested in the lowest lying energy states of the system, it will suffice to include just a few lowest momentum operators. We will define an appropriate set of operators, $\mathcal{O}_a$, and measure the correlation matrix, $\langle \mathcal{O}_a(t)^\dagger \mathcal{O}_b(0) \rangle$. We then diagonalise this matrix and extract the energy values from the exponential decay of the eigenvalues of the correlation matrix.

Operators

Since we are only interested in the lowest lying energy states of the system, it will suffice to include just a few of the lowest momentum operators. We would like to construct ϕ operators with momentum $\vec{P} = 0$, concentrating our efforts on the centre of mass frame. We also need χ operators for the lowest momentum states. As we will see later, the states corresponding to the lowest energies changes due to level crossings higher in the spectrum. Thus, we must choose our operators differently for each N_z. Let us intially define our basic building block operators as simple Fourier transforms of the field;

$$\tilde{\phi}(\vec{P}, t) = \frac{1}{V} \sum_{\vec{x}} \phi(\vec{x}, t) e^{i\vec{P}\vec{x}} \tag{3.64}$$

and similarly for the χ field;

$$\tilde{\chi}(\vec{n}, t) = \frac{1}{V} \sum_{\vec{x}} \chi(\vec{x}, t) e^{i\vec{p}\vec{x}} \tag{3.65}$$

with

$$\vec{n}_i = \left(\frac{p_{xi} N_s}{2\pi}, \frac{p_{yi} N_s}{2\pi}, \frac{p_{zi} N_z}{2\pi} \right) \in Z^3. \tag{3.66}$$

We will now combine these according to the momentum requirements of each specific ϕ and $\chi\chi$ operator. The ϕ operators are quite simply defined as $\mathcal{O}_{\vec{P},0} = \tilde{\phi}(\vec{P}, t)$. As mentioned previously, we are restricting ourselves to the $\vec{d} = 0$ case. The $\chi\chi$ operators in the $\vec{d} = 0$ case consists of two χ fields with equal and opposite momentum. The momenta, $\vec{p}_i$, corresponding to the lowest free energy states, E_i, are used. Up to renormalisation, these should coincide with the lowest momentum states of the interacting theory. Our $\chi\chi$ operators are thus given as

$$\mathcal{O}_{0,i}(t) = \frac{1}{N_i} \sum_{\vec{m}} \delta_{(m_x^2+m_y^2),(n_{xi}^2+n_{yi}^2)} \delta_{m_z,n_{zi}} \tilde{\chi}(\vec{m}, t) \tilde{\chi}(-\vec{m}, t) \tag{3.67}$$

where $N_i = \sum_{\vec{m}} \delta_{(m_x^2+m_y^2),(n_{xi}^2+n_{yi}^2)} \delta_{m_z,n_{zi}}$.

We now correlate these operators giving our correlation matrix.

$$C_{ab}^0(t) = \langle \mathcal{O}_{0,a}(t)^\dagger \mathcal{O}_{0,b}(0) \rangle \tag{3.68}$$

As before, we perform a disconnected subtraction. Whereas in the case of the perturbation theory, the vaccuum subtraction amounted to excluding certain disconnected contractions in the expansion, in the Monte Carlo simulation, we must perform these subtractions explicitly,

$$C^0_{ab}(t) = \langle \mathcal{O}_{0,a}(t)^\dagger \mathcal{O}_{0,b}(0) \rangle - \langle \mathcal{O}_{0,a}(t) \rangle \langle \mathcal{O}_{0,b}(0) \rangle \tag{3.69}$$

While, in the perturbative case, the extent of the temporal direction was taken to be infinite, in the Monte Carlo simulations, this direction will be of finite extent. The expression for the lattice propagator is now extended over the temporal direction;

$$K_{nm} = -\sum_{\mu=0}^{3} (\delta_{n+\mu,m} + \delta_{n-\mu,m} - 2\delta_{nm}) + m^2 \delta_{nm} \tag{3.70}$$

$$\tilde{K}_k = \sum_{\mu=0}^{3} \left(\sin^2 \frac{k_\mu}{2} \right) + m^2. \tag{3.71}$$

The form of the action allows us to perform a simple transformation of the ϕ field, which will greatly improve the accuracy of the Monte Carlo measurements in channels involving the ϕ operator.

3.2.2 Integrating Out the ϕ field

To reduce the noise in our measurements, we now note that $\mathcal{L}$ is quadratic in ϕ. This means that if we "complete the square" in the ϕ field, we can perform a change of variables which will leave us with a Gaussian integral over our new field ϕ'. This integration can then be performed analytically. (Here, we use the notation $\phi_a = \phi(\vec{x_a}, t_a)$ etc.) Firstly let us see how our ϕ field will transform to give us a Gaussian integral.

$$\begin{aligned}
\mathcal{L} &= \frac{1}{2}\phi(\partial^2 + m_\phi^2)\phi + \frac{1}{2}\chi(\partial^2 + m_\chi^2)\chi + \lambda\phi\chi^2 + \frac{\mu}{4!}\chi^4 \\
&= \phi_p K_{\phi pq} \phi_q + \chi_p K_{\chi pq} \chi_q + \lambda \phi_p \chi_q^2 + \frac{\mu}{4!}\chi^4 \\
&= \left(\phi_p + \frac{\lambda \chi_u^2 K^{-1}_{\phi up}}{2} \right) K_{\phi pq} \left(\phi_q + \frac{\lambda \chi_v^2 K^{-1}_{\phi vq}}{2} \right) - \frac{\lambda^2 \chi_u^2 K^{-1}_{\phi uv} \chi_v^2}{4} \\
&\quad + \chi K_\chi \chi + \frac{\mu}{4!}\chi^4
\end{aligned} \tag{3.72}$$

We make the change of variable

$$\phi_a \to \phi'_a = \phi_a + \frac{\lambda \chi_p^2 K^{-1}_{\phi pa}}{2} \tag{3.73}$$

Thus we have

$$\mathcal{L} = \phi'_p K_{\phi pq} \phi'_q - \frac{\lambda^2 \chi_u^2 K^{-1}_{\phi uv} \chi_v^2}{4} + \chi K_\chi \chi + \frac{\mu}{4!} \chi^4 \tag{3.74}$$

The partition functions

$$Z_\phi = \int \mathcal{D}\phi e^{-S_\phi} \tag{3.75}$$

and

$$Z_\chi = \int \mathcal{D}\chi e^{-S_\chi} \tag{3.76}$$

are unchanged by this procedure. Now we will implement this change of variable in three cases; $\langle \phi_a \rangle$, $\langle \phi_a \chi_b \chi_b \rangle$ and $\langle \phi_a \phi_b \rangle$.

$$\begin{aligned}
\langle \phi_a \rangle &= \frac{1}{Z_\phi Z_\chi} \frac{1}{V} \sum_{\vec{x}_a} \int \mathcal{D}\phi \mathcal{D}\chi \ \phi_a e^{-S} \\
&= \frac{1}{Z_\phi Z_\chi} \frac{1}{V} \sum_{\vec{x}_a} \int \mathcal{D}\phi \mathcal{D}\chi \ \left(\phi_a - \frac{\lambda \chi_u^2 K^{-1}_{\phi ua}}{2} \right) e^{-S} \\
&= -\frac{1}{Z_\chi} \frac{1}{V} \sum_{\vec{x}_a} \int \mathcal{D}\chi \ \frac{\lambda \chi_u^2 K^{-1}_{\phi ua}}{2} e^{-S_\chi}
\end{aligned} \tag{3.77}$$

The first term above, in the ϕ field, vanishes, since it is a product of the odd function, ϕ, with the even Gaussian exponential. This is the vacuum subtraction for the ϕ field. Note how the ϕ field has been replaced in this expression by a new field, $\frac{\lambda \chi_u^2 K^{-1}_{\phi ua}}{2}$. Similarly in the second case;

$$\begin{aligned}
\langle \phi_a \chi_b \chi_c \rangle &= \frac{1}{Z_\phi Z_\chi} \frac{1}{V^3} \sum_{\vec{x}_a, \vec{x}_b, \vec{x}_c} \int \mathcal{D}\phi \mathcal{D}\chi \ \phi_a \chi_b \chi_c e^{-S} e^{i\vec{p}(\vec{x}_b - \vec{x}_c)} \\
&= \frac{1}{Z_\phi Z_\chi} \frac{1}{V^3} \sum_{\vec{x}_a, \vec{x}_b, \vec{x}_c} \int \mathcal{D}\phi \mathcal{D}\chi \ \left(\phi_a - \frac{\lambda \chi_u^2 K^{-1}_{\phi ua}}{2} \right) \chi_b \chi_c e^{-S} e^{i\vec{p}(\vec{x}_b - \vec{x}_c)} \\
&= -\frac{1}{Z_\chi} \frac{1}{V^3} \sum_{\vec{x}_a, \vec{x}_b, \vec{x}_c} \int \mathcal{D}\chi \ \frac{\lambda \chi_u^2 K^{-1}_{\phi ua}}{2} \chi_b \chi_c e^{-S_\chi} e^{i\vec{p}(\vec{x}_b - \vec{x}_c)}
\end{aligned} \tag{3.78}$$

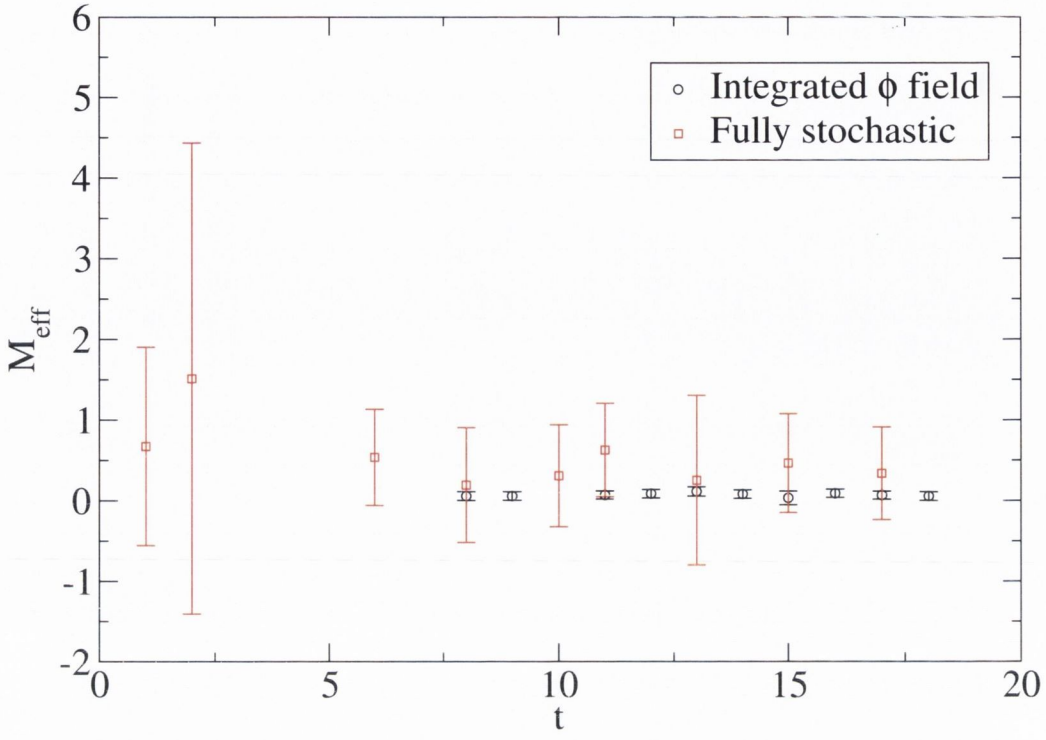

Figure 3-5: $\phi \rightarrow \chi\chi$ Effective mass plots for fully stochastic and integrated ϕ cases at similar statistics. In the integrated case, an effective mass of about 0.05 is measured. This signal is statistically zero in the fully stochastic case.

The final case is slightly different;

$$\begin{aligned}
\langle \phi_a \phi_b \rangle &= \frac{1}{Z_\phi Z_\chi} \frac{1}{V^2} \sum_{\vec{x}_a, \vec{x}_b} \int \mathcal{D}\phi \mathcal{D}\chi \ \phi_a \phi_b e^{-S} \\
&= \frac{1}{Z_\phi Z_\chi} \frac{1}{V^2} \sum_{\vec{x}_a, \vec{x}_b} \int \mathcal{D}\phi \mathcal{D}\chi \ \left(\phi_a - \frac{\lambda \chi_u^2 K^{-1}_{\phi ua}}{2} \right) \left(\phi_b - \frac{\lambda \chi_q^2 K^{-1}_{\phi qb}}{2} \right) e^{-S} \\
&= \frac{1}{Z_\phi Z_\chi} \frac{1}{V^2} \sum_{\vec{x}_a, \vec{x}_b} \int \mathcal{D}\phi \mathcal{D}\chi \ \left(\phi_a \phi_b + \frac{\lambda \chi_u^2 K^{-1}_{\phi ua}}{2} \frac{\lambda \chi_q^2 K^{-1}_{\phi qb}}{2} \right) e^{-S} \\
&= \frac{1}{Z_\chi} \frac{1}{V^2} \sum_{\vec{x}_a, \vec{x}_b} \left[K_{\phi ab} + \frac{\lambda^2}{4} \int \mathcal{D}\chi \ \chi_u^2 K^{-1}_{\phi ua} \chi_q^2 K^{-1}_{\phi qb} \right] e^{-S_\chi} \qquad (3.79)
\end{aligned}$$

Again, in the final term, the ϕ field is replaced by a $\frac{\lambda \chi_u^2 K^{-1}_{\phi ua}}{2}$ field. The first term integrates to give us the Feynman propagator and cross terms, proportional to λ vanish as before by symmetry. In Fig. 3-5, we see the dramatic effect this integration has on, in particular, the $\phi \rightarrow \chi\chi$ effective mass plot.

While this integration trick clears up the $\phi \rightarrow \chi\chi$ channel, the inversion of the $\phi\phi$

is computationally expensive, especially when it is considered that the contribution of this channel in negligible unless $E_\phi \sim E_{\chi\chi}$. To prevent an irrelevant calculation from critically slowing the simulation, this integration trick is only used in the vicinity of an avoided level crossing. Elsewhere, the correlation matrix is taken to be diagonal. When we examine the decompostion of the energy eigenstates, we will justify ignoring the overlap between states in this area. Also, when this integration trick isn't implemented, the $\phi \rightarrow \phi$ correlator is measured purely stochastically. Though the error is higher than in the integrated case, it will be comparable with the error in the $\chi\chi \rightarrow \chi\chi$ channel. Such a sacrifice is acceptable to simulation time in regions where the $\phi \rightarrow \chi\chi$ channel is less relevant.

Discrete Action

We must rewrite our action in a discrete form for lattice calculations. The anisotropic nature of the lattice must be respected by the introduction of two distinct lattice spacings, a_t and a_s in the temporal and spatial directions respectively. The discrete form of the action used is

$$\begin{aligned} S \;=\; & \sum_x \Bigg[\sum_i \frac{1}{a_i^2} \Big[\Big(\phi(x) - \phi(x+\hat{i})\Big)^2 + \Big(\phi(x) - \phi(x-\hat{i})\Big)^2 \\ & + \Big(\chi(x) - \chi(x+\hat{i})\Big)^2 + \Big(\chi(x) - \chi(x-\hat{i})\Big)^2 \Big] \\ & + m_\phi^2 \phi(x)^2 + m_\chi^2 \chi(x)^2 + \lambda \phi(x)\chi(x)^2 + \lambda \phi(x)\chi(x)^2 + \frac{\mu}{4!}\chi(x)^4 \Bigg] . \end{aligned} \tag{3.80}$$

To reduce the lattice spacing errors, we set $a_t = 0.5$, while keeping a_s set to unity. This quadratic form of the kinetic terms prevents the fields from collapsing to $-\infty$ in the Monte Carlo simulations.

3.2.3 From the Correlation Matrix to the Energy Spectrum

With our examination of the correlation matrix measurement complete, we must now consider how we will recover the energy spectrum from this point. In Ref. [20], Lüscher and Wolff equip us with a method for doing just that. If we solve the

generalised eigenvalue problem;

$$C(t)\psi_a = \lambda_a(t, t_0)C(t_0)\psi_a, \tag{3.81}$$

we find that the eigenvalues, λ, are of the form

$$\lambda_a = e^{-(t-t_0)E_a}. \tag{3.82}$$

We choose the reference time, t_0, to be small.

In practice, this can be achieved by diagonalising $D(t)$;

$$D(t) = C^{-1/2}(t_0)C(t)C^{-1/2}(t_0). \tag{3.83}$$

Each of these eigenvalues is then fit to an exponential from which the energy of each state can be extracted. This also affords us the opportunity to examine the composition of the eigenvectors, Ψ_a, corresponding to these eigenfunctions. We see that $\psi_a = C^{-1/2}(t_0)\Psi_a$ gives the projections of Ψ_a onto the states used to compose the correlation matrix. The normalised squares of these components can be used to analyse the composition of each eigenvectors.

Now that we have discussed the extraction of the finite volume energy spectrum from the correlation matrix using both Euclidean perturbation theory and Markov Chain Monte Carlo, we must now examine the path from this spectrum to the decay width, as presribed by Lüscher.

3.2.4 From the Energy Spectrum to the Decay Width

Now that we have discussed how to extract the energy spectrum of our theory, using both Perturbation Theory and Monte Carlo integration, we now must use this finite volume spectrum to calculate the infinite volume scattering phase shift, as Lüscher prescribes, and then fit this to a perturbative or Breit-Wigner function to calculate the decay width.

$\bullet E \rightarrow p$

Since the expression for the scattering phase shift, δ, is a function of the absolute value of the momentum, p, we must find some way to express p as a function of the energy, E. There are a number of possibilities [14, 19]. A simple approach would be to use the lattice dispersion relation directly, writing it as

$$p^2 = 4\sinh^2\left(\frac{W}{4}\right) - m_\chi^2 \tag{3.84}$$

For low energies, this will work quite well, but approaching the inelastic threshold, $W = 4m_\chi$, lattice effects make this method unfeasible. The next approach is to use the limits of the elastic region to define bounds on p. The elastic region is bounded by $0 \leq p < \sqrt{3}m_\chi$. Replacing this in the lattice dispersion relation, this gives us

$$\sqrt{3}\cos^{-1}\left[1 - \frac{1}{3}(\cosh(W/2) - \cosh m_\chi)\right] \leq p \leq \cos^{-1}\left[1 - (\cosh(W/2) - \cosh m_\chi)\right] \tag{3.85}$$

While these bounds are tight (to about 1%), we will still waste the accuracy of the data by using this method.

If we assume that our energy state is bounded between two free energy levels; $W_n \leq W \leq W_{n+1}$, with associated momenta $\vec{p}_n$ and $\vec{p}_{n+1}$, we can write the momentum, $\vec{p}$, of the state with energy W as

$$\vec{p} = \rho\vec{p}_n + (1-\rho)\vec{p}_{n+1}. \tag{3.86}$$

We, now, simply interpolate a value of ρ until we find $\vec{p}$ which satisfies the lattice dispersion relation for that value of W.

$\bullet p \longrightarrow \delta(p)$

Now that we have values for the momentum corresponding to the energies, we are now ready to evaluate the scattering phase shift, $\delta(p)$. Again, we have

$$\delta(p) = -\phi(q) \mod \pi, \quad q = \frac{pL}{2\pi}, \tag{3.87}$$

where $\phi(p)$ is a continuous function defined by

$$\tan(-\phi(q)) = \frac{\gamma q \pi^{3/2}}{Z_{00}(1, q^2)}, \quad \phi(0) = 0. \tag{3.88}$$

$Z_{00}(s, q^2)$ is a generalised Zeta function;

$$Z_{00}(s, q^2) = \frac{1}{\sqrt{4\pi}} \sum_{\vec{r} \in Z^3} (\vec{r}^2 - q^2)^{-s} \tag{3.89}$$

Our next task is to evaluate $Z_{00}(s, q^2)$ numerically.

Numerical Calculation of the Generalised Zeta Function

To evaluate the generalised Zeta function numerically, we must first truncate the infinite sum in some way. We write it as

$$Z_{lm}(s, q^2, \eta_1, \eta_2) = \sum_{|\vec{r}| < \lambda} \mathcal{Y}_{lm}(\tilde{r}^2 - q^2)^{-s} + \frac{(2\pi)^3}{\Gamma(s)} \int_0^\infty dt \; t^{s-1} e^{tq^2} K^\lambda_{lm}(t, 0) \tag{3.90}$$

where

$$\mathcal{Y}_{lm} = r^l Y_{lm}(\theta, \phi) \tag{3.91}$$

and $K(t, \vec{x})$ is the heat kernel of the Laplace operator on a $\vec{d}$-periodic torus (i.e. such that the periodicity is given by $\phi(\vec{x}) = (-1)^{\vec{d}.\vec{n}} \phi(\vec{x} + 2\pi\hat{\gamma}\vec{n})$, $\vec{n} \in \mathbb{Z}^3$);

$$K(t, \vec{r}) = \begin{cases} (2\pi)^{-3/2} \sum_{\vec{n} \in Z^3} e^{i\tilde{n}r - t\tilde{n}^2}, & t > 1 \\ \eta_1 \eta_2 (4\pi t)^{-3/2} \sum_{\vec{n} \in Z^3} e^{-(r - 2\pi\tilde{n})^2/4t}, & t \leq 1 \end{cases} \tag{3.92}$$

$$K^\lambda(t, \vec{r}) = K(t, \vec{r}) - (2\pi)^{-3} \sum_{|\tilde{n}| < \lambda} e^{i\tilde{n}r - t\tilde{n}^2} \tag{3.93}$$

$$K^\lambda_{lm}(t, \vec{r}) = (i)^l \mathcal{Y}_{lm} K^\lambda(t, \vec{r}) \tag{3.94}$$

We have introduced a cut-off λ in the sum. The value of λ is chosen such that $\lambda^2 > \Re q^2$. In particular, for $l = m = 0$ and $s = 1$, we have

$$Z_{00}(1, q^2, \eta_1, \eta_2) = \frac{1}{\sqrt{4\pi}} \sum_{|\tilde{r}|<\lambda} (\tilde{r}^2 - q^2)^{-1} + (2\pi)^3 \int_0^\infty dt\ e^{tq^2} K_{00}^{\lambda}(t, 0) \tag{3.95}$$

As $t \to \infty$, the integrand vanishes. As $t \to \infty$, $e^{tq^2} K_{00}^{\lambda}(t, 0) = t^{-3/2}$. Using this asymptotic behaviour, we can rewrite this as

$$\begin{aligned} Z_{00}(1, q^2, \eta_1, \eta_2) &= \frac{1}{\sqrt{4\pi}} \sum_{|\tilde{r}|<\lambda} (\tilde{r}^2 - q^2)^{-1} \\ &+ (2\pi)^3 \int_0^1 dt\ \left[e^{tq^2} K_{00}^{\lambda}(t, 0) - t^{-3/2} \right] \\ &+ (2\pi)^3 \int_1^\infty dt\ e^{tq^2} K_{00}^{\lambda}(t, 0) - 2. \end{aligned} \tag{3.96}$$

Rearranging this and performing the intergration from 1 to ∞ analytically, it becomes

$$\begin{aligned} Z_{00}(1, q^2, \eta_1, \eta_2) = &\sum_n \frac{1}{4\pi} \frac{e^{q^2 - \tilde{n}^2}}{\tilde{n}^2 - q^2} - \pi\eta_1\eta_2 \\ &+ \frac{\pi}{\eta_1\eta_2} \int_0^1 t^{-3/2} (e^{tq^2} - 1) dt \\ &+ \frac{\pi\eta_1\eta_2}{\sqrt{4\pi}} \int_0^1 t^{-3/2} \sum_n e^{tq^2 - \pi^2\tilde{n}^2/t} dt. \end{aligned} \tag{3.97}$$

We have now written $Z_{00}(1, q^2, \eta_1, \eta_2)$ in a form which can be computed numerically; a quickly converging sum and an integral which can be evaluated using Simpson's Rule.

In Fig. 3-6, we see the plot of $\phi(q)$ against q^2 we obtain using this method. A direct numerical comparison for the $\eta_1 = \eta_2 = 1$ case is available in [17] and for the $\eta_1 \neq \eta_2$ case in [1].

$\bullet \delta(p) \to \Gamma$

The final step in the process is to calculate the decay width, Γ, from the scattering phase shift, $\delta(p)$. There are two ways to achieve this; we can fit to a Breit-Wigner expression. While this is theory independent, it is only valid for certain values of $\delta(p)$ ($\pi/4 \leq \delta(p) \leq 3\pi/4$). Alternatively, we can fit to a tree-level perturbative expansion for $\delta(p)$. While this is valid for all values of the scattering phase shift, it is model

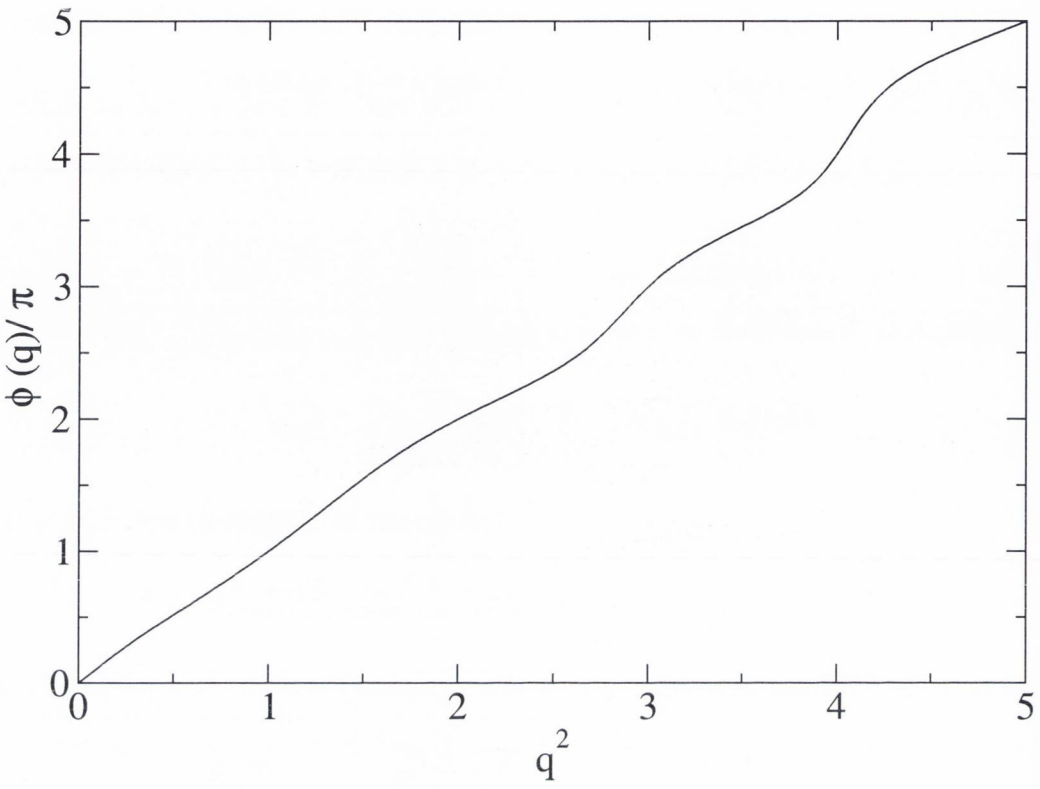

Figure 3-6: $\phi(q)$ vs q^2

dependent and also subject to the inherent higher order corrections of a perturbative calculation.

Breit-Wigner Fit

For $\pi/4 \leq \delta(p) \leq 3\pi/4$, the Breit-Wigner form

$$\tan(\delta - \frac{\pi}{2}) = \frac{W^2 - m_\phi^2}{m_\phi \Gamma}. \tag{3.98}$$

We fit the values of m_ϕ and Γ using this expression. While this approach has the advantage of being model independent, only the few measurements in the region of the avoided level crossings fall in the range over which this form is valid. Measurements away from the avoided level crossings, where $\delta \sim \pi$ or $\delta \sim 0$, may not be included in a fit to a Breit-Wigner function.

Perturbative Fits

An alternative approach is to use a tree-level perturbative expansion for $\delta(p)$. Conversely, this is model dependent, but works for the full range of values the scattering phase shift. Writing $\delta(p)$ as a sum of a regular and a singular part, as in, [14], we have

$$\delta(p) = \delta_r(p) + \delta_s(p) \tag{3.99}$$

$$\delta_r(p) = -\frac{3\mu_R p}{4\pi W} + \frac{\lambda_R^2}{32\pi W p} log_e \frac{4p^2 + m_\phi^2}{m_\phi^2} \tag{3.100}$$

$$\tan(\delta_s(p)) = -\frac{\lambda_R^2 p}{16\pi W(W^2 - m_\phi^2)} \tag{3.101}$$

We fit these to the phase shift data with λ_R, μ_R and m_ϕ as our fit parameters. Once values for these parameters have been found, we can use them to calculate the decay width from

$$\Gamma = \frac{\lambda_R^2}{8\pi m_\phi^2}\sqrt{m_\phi^2 - 4m_\chi^2} \tag{3.102}$$

The discussion of the methods used in the Euclidean formulation of perturbation theory and Markov Chain Monte Carlo to, firstly, calculate the finite volume energy spectrum and hence, evaluate the decay width, is now complete. We now address the results of these calculations, and also the Minkowski perturbation theory calculations.

Chapter 4

Results/Analysis of $\phi \longrightarrow \chi\chi$

The results of the calculations discussed in the previous chapter are now presented. We will begin with the perturbative calculations, then the Markov Chain Monte Carlo results, before, finally, comparing the outcomes of the two approaches.

4.1 Perturbation Theory Results

The results of the perturbative calculations come in three parts. Firstly, we will examine the estimate of the decay width, Γ, from the mass and coupling renormalisations. Subsequently, the Euclidean energy spectrum and scattering phase shift and the Minkowski decay width will be investigated.

4.1.1 Mass and Coupling Renormalisations

We initially look at the mass and coupling renormalisations. We solve

$$[p^2 - m^2_{\phi,\chi 0} - \Sigma_{\phi,\chi}(p)]|_{p^2=m^2_{\phi,\chi}} = 0. \tag{4.1}$$

with

$$\Sigma_\phi(p) = \lambda^2 \int \frac{d^4k}{(2\pi)^4} \frac{1}{k^2 - m^2_{\chi 0}} \frac{1}{(p-k)^2 - m^2_{\chi 0}} \tag{4.2}$$

and

$$\Sigma_\chi(p) = \lambda^2 \int \frac{d^4k}{(2\pi)^4} \frac{1}{k^2 - m^2_{\chi 0}} \frac{1}{(p-k)^2 - m^2_{\phi 0}} + \frac{\mu}{2} \int \frac{d^4k}{(2\pi)^4} \frac{1}{k^2 - m^2_{\chi 0}}. \tag{4.3}$$

	Renormalised Values	Bare Values
m_ϕ	1.0016	1
m_χ	0.3949	0.375
λ_R	0.588	0.5
μ_R	2.0808	1.5

Table 4.1: Masses and couplings renormalised perturbatively

The values of $\Sigma_{\phi,\chi}$ are calculated numerically using the prescription given in the section on the lattice form of the progagator. The box sizes, N_z and N_t are set to 40 and N_s is increased until an infinite volume limit is reached. Plots of the renormalised masses and couplings against N_s are given Fig. 4-1. Stable values are seen to be reached by about $N_s = 25$. The renormalised values of the masses and couplings are presented in Table 4.1. As we will see, these values match well with those measured in the Monte Carlo simulations. Using these in the perturbative expansion for the decay width, Γ(Eq. 3.20), gives us a value of $\Gamma = 8.44 \times 10^{-3}$. A plot showing how Γ approaches this value with increasing N_s is given in Fig. 4-2. One important point to note is that the correlation matrix approach takes into account the correlations between the ϕ and $\chi\chi$ states, omitted in this method. This is strongly believed to be a cause of any discrepancy between the results of the two approaches.

4.1.2 Euclidean Correlation Matrix and Spectrum

For these calculations, we set $N_s = 5$, $N_t = 40$ and varied N_z from 10 to 40. At each lattice volume, the lowest four $\chi\chi$ states, together with the resting ϕ state were used to construct a correlation matrix. The nuances of ordering states on this brick shaped lattice will be discussed in the Monte Carlo results section. By solving the matrix determinant equation

$$\det C^{-1}(\Omega) = 0 \tag{4.4}$$

we can probe the energy spectrum of the states in the Euclidean formulation, as was observed in the last chapter.

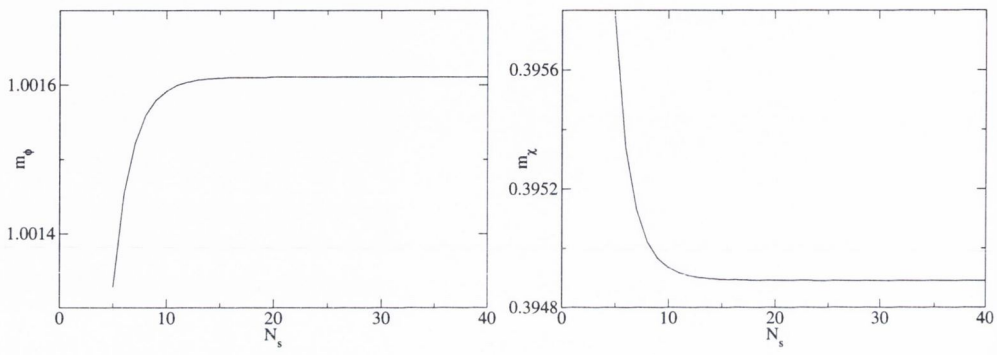

(a) m_ϕ (b) m_χ

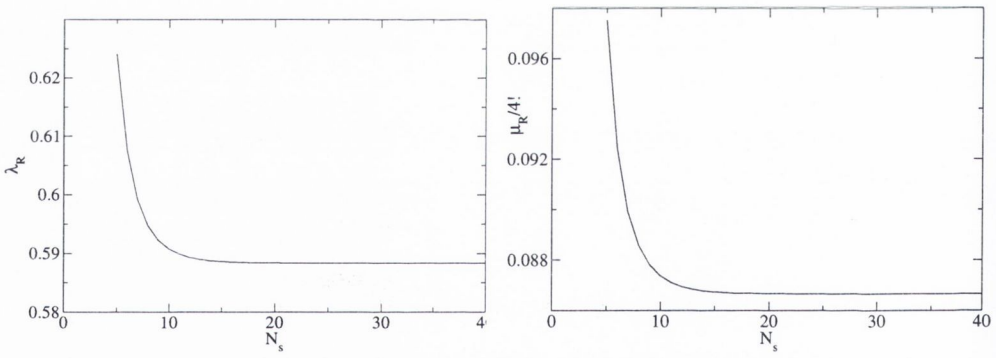

(c) λ (d) μ

Figure 4-1: Perturbative mass and coupling renormalisations

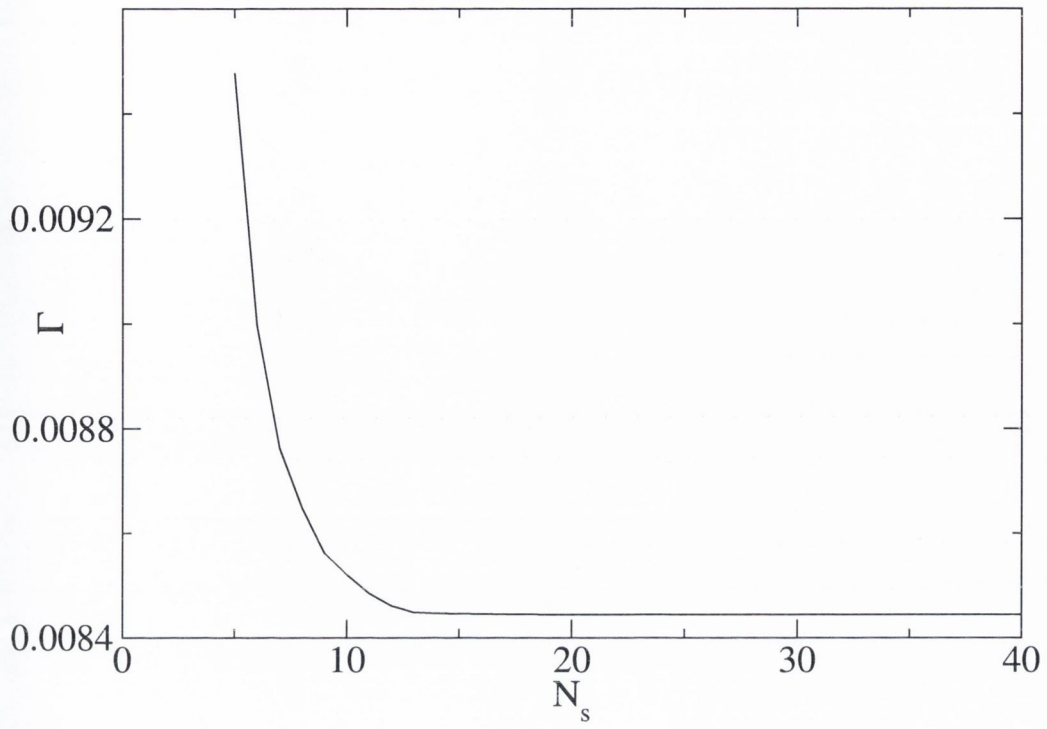

Figure 4-2: Γ vs N_s using the renormalised couplings and masses in the perturbative expansion.

Energy Spectrum

The energy spectrum calculated in perturbation theory is shown in Fig. 4-3. This gives us some guideline of what to expect from the Monte Carlo simulations, though there will be some $\mathcal{O}(\lambda^4)$ corrections. Also, the two approaches depend on slightly different dispersion relations, a fact which will manifest itself as discrepancies at high energies.

The avoided level crossings caused by the ϕ state cutting across the $\chi\chi$ spectrum are evident. These crossings can be quantified by looking at the parameter ρ, defined previously when we were examining the interpolation of the momenta by

$$\vec{p} = \rho\vec{p}_n + (1-\rho)\vec{p}_{n+1}. \tag{4.5}$$

The dependence of ρ on N_z for the ϕ state is presented in Fig. 4-4. We can clearly see initially the value of ρ falling to zero. This corresponds to the ϕ state moving towards the first excited $\chi\chi$ state at the avoided level crossing at $N_z = 20$. At this point, ρ returns to a value of 1, as it begins to chart the movement of the the ϕ state from

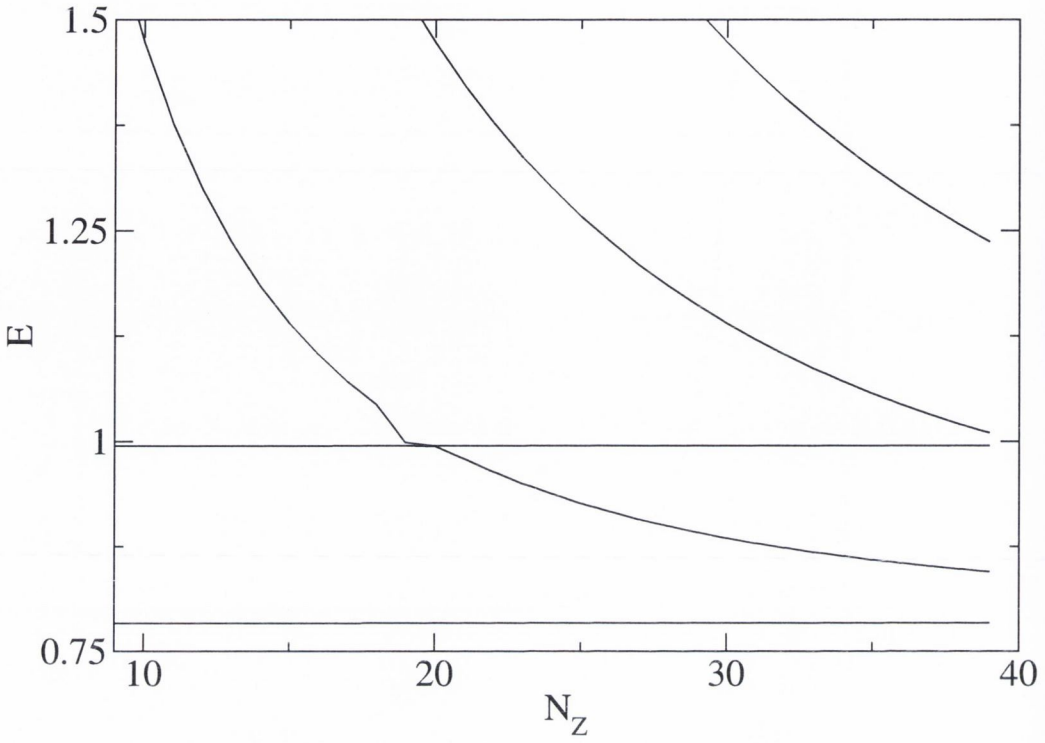

Figure 4-3: Two particle spectrum in Euclidean perturbation theory.

the first excited to the second excited $\chi\chi$ state. Again, we see ρ falling towards zero at an avoided level crossing just beyond the limit of our investigation at $N_z = 40$.

We also examine the scattering phase shift, $\delta(p)$, as a function of momentum (Fig. 4-5). As was noted in Ref. [14], points with $p > M_\chi$ and small lattice volumes are subject to large finite volume polarisations and finite lattice spacing effects. Thus only values of $\delta(p)$ for the ϕ state, and the ground and first excited $\chi\chi$ states are plotted. While we cannot continue down the path laid out in the previous chapter, as this would require us to fit the phase shift data to the perturbative expansion, this examination of the scattering phase shift the perturbative case gives us a useful comparison for the Monte Carlo data. We see a sudden step in the scattering phase at $p = 0.307$. This momentum corresponds to an energy of m_ϕ. The cluster of points near the origin correspond to the ground $\chi\chi$ state, while the vertical line comes from the ϕ state. The excited $\chi\chi$ state accounts for the remaining points forming the horizontal plateaux.

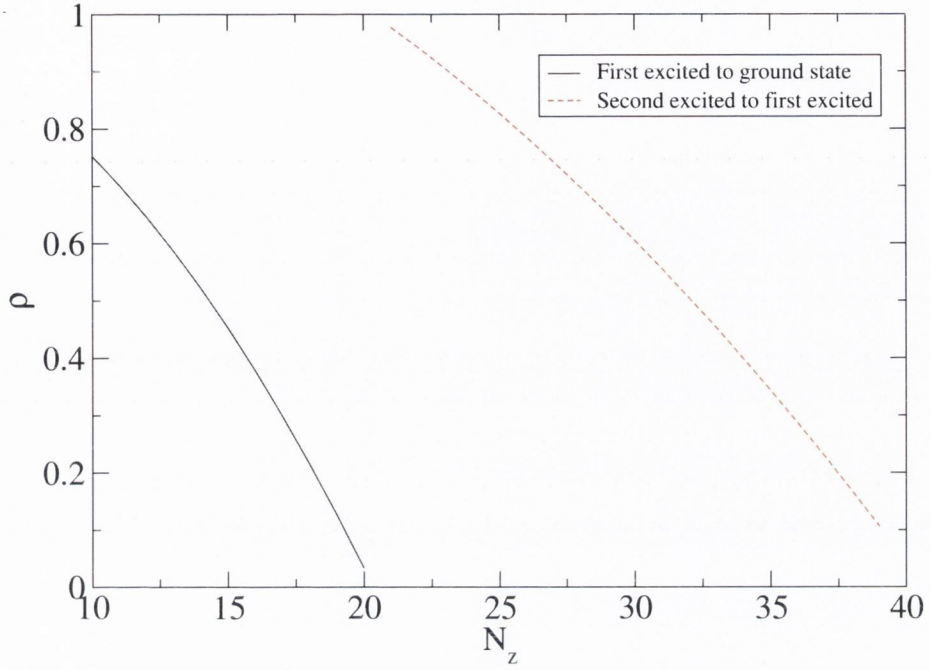

Figure 4-4: ρ vs N_z

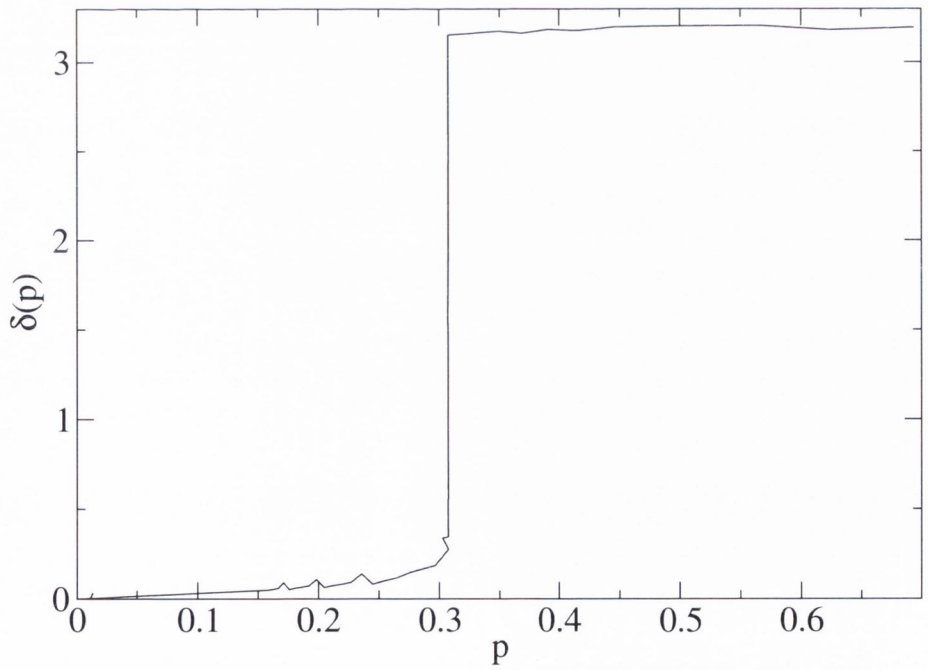

Figure 4-5: $\delta(p)$ vs p/m_χ from perturbation theory.

4.1.3 Minkowski Formulation and the Decay Width

We saw in the previous chapter, that the imaginary part of the energy at the pole in the correlation function is related to the decay width of a particle. Here, we will look at the results for the $\phi \rightarrow \phi$ and $\chi\chi \rightarrow \chi\chi$ cases separately.

ϕ Decay Width

From the previous chapter the decay width of the ϕ particle is related to the $\chi\chi$ loop, and can be written as a sum over the $\chi\chi$ states;

$$\Gamma = \frac{12\lambda^2}{N_Z(4\pi)^{3/2}} \sum_{k_z} \frac{1}{m_\phi} \left[\log_e \left(m_\phi \sqrt{1 - \frac{4R^2}{m_\phi^2}} \right) - \log_e \left(2\sqrt{2} + m_\phi \sqrt{1 - \frac{4R^2}{m_\phi^2}} \right) \right] \theta(m_\phi - 2R(\vec{k})). \tag{4.6}$$

While the dependence of Γ on λ is trivially quadratic, the behaviour when the masses are changed is less obvious. The plots in Fig. 4-6 give us good qualitative insight into Γ. For these plots, we set $N_z = 100000$, $m_\chi = 0.375$, $m_\phi = 1$ and $\lambda = 0.5$, varying only the parameter indicated. Though the value of N_z seems very large, it is necessary to go to this volume to ensure the infinite volume limit in this case. Looking at the relationship between Γ and m_ϕ, we see that $\Gamma = 0$ at $m_\phi = 0.75 = 2m_\chi$, as is to be expected at threshold. The value of Γ then rises quickly as is to be expected for an increasingly unstable particle. Similarly, as the χ particle becomes heavier, the decay width becomes smaller, vanishing at the threshold.

Now let us examine the dependence of Γ on the volume of the box, N_z. A plot of Γ against N_z for the ϕ state can be seen in Fig. 4-7. This plot shows individual contributions from each of the $\chi\chi$ states, as well as the sum, as indicated in Eq. 4.6. We can see how each of the $\chi\chi$ channels starts contributing once the Heaviside step function is satisfied. This produces discrete jumps in Γ as the new decay processes become available. In the infinite volume limit, $N_Z \rightarrow \infty$, Γ tends to a value of $\Gamma = 8.93 \times 10^{-3}$.

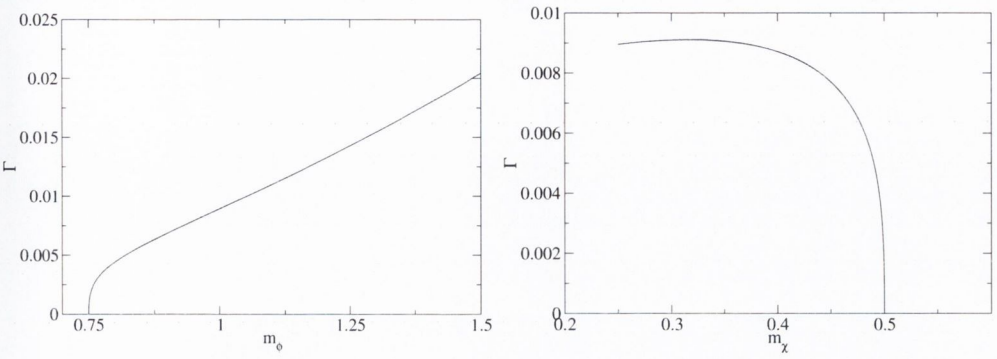

(a) Γ vs m_ϕ (b) Γ vs m_χ

Figure 4-6: The dependence of Γ on the masses, m_ϕ and m_χ.

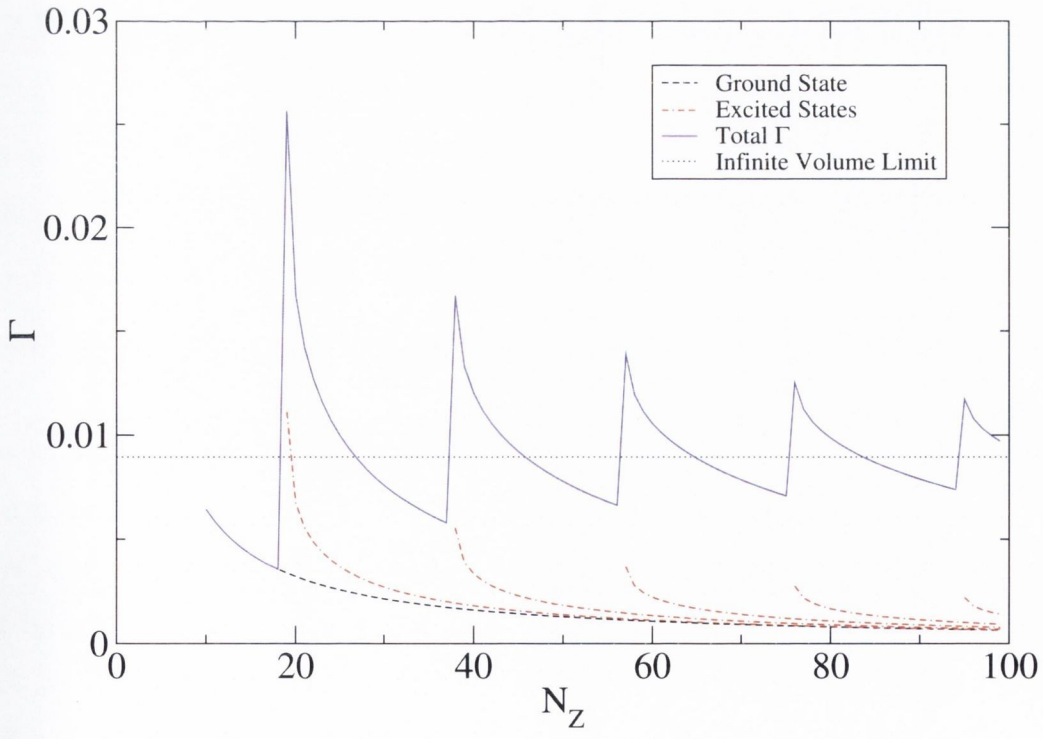

Figure 4-7: Γ vs N_z for the ϕ state.

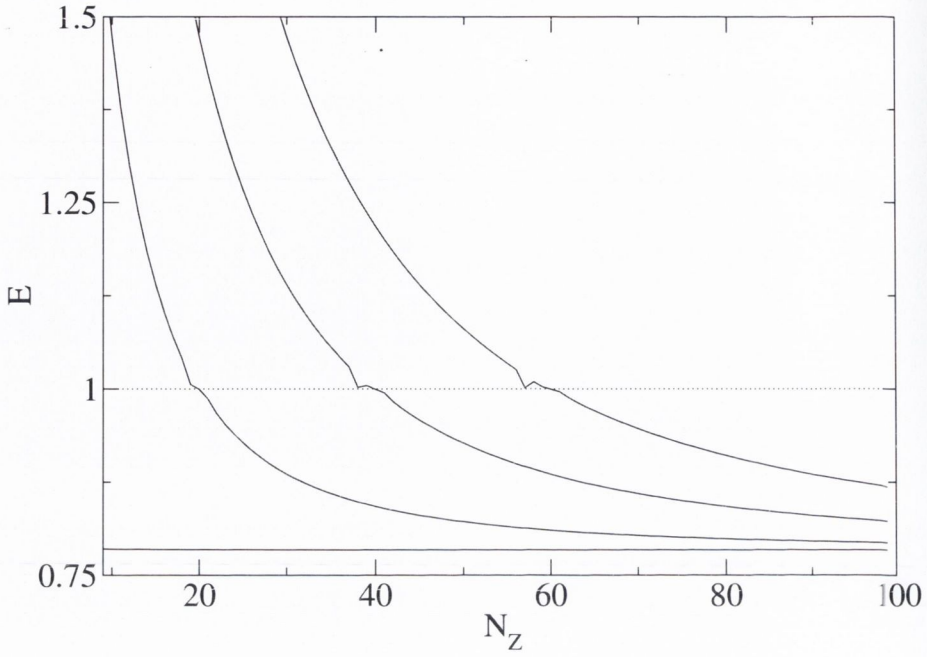

Figure 4-8: The $\chi\chi$ spectrum.

$\chi\chi$ Decay Width and Spectrum

We investigated the properties of the $\chi\chi$ states more thoroughly. We were able to solve the equation $c^{-1}(\Omega) = 0$ directly. This final form of this equation is

$$2\pi R\Omega(\Omega - 2R) - \lambda^2 \left(\frac{1}{(\Omega^2 - m_\phi^2)N_s^2 N_Z} - \frac{1}{4m_\phi^2} \right) = 0 \tag{4.7}$$

where $R^2 = \vec{k}^2 + m_\chi^2$. Here we have used $\mu = \lambda^2/4m_\phi^2$. The volume factor between the two interaction terms comes from a extra integration over an undetermined momentum in the s-channel diagram.

As well as giving us access to the decay width, via the imaginary part of Ω, we could also plot the energy from the real part. The energy spectrum can be seen in Fig. 4-8. A dashed line is included to indicate $m_\phi = 1$ to guide the eye. We see slight plateaux in the spectrum around m_ϕ. The reasons for this are linked to the high dependence of the interacting terms of Eq. 4.7 on m_ϕ. If we look at $\Im E = \Gamma_{\chi\chi}/2$ (Fig. 4-9), we see that it takes on non-zero values at other values of N_z corresponding to these plateaux. When the $\chi\chi$ energy is close enough to m_ϕ, it is kinematically possible for the $\chi\chi$ state to decay to a ϕ particle. Thus, we see spikes in $\Im E$ around

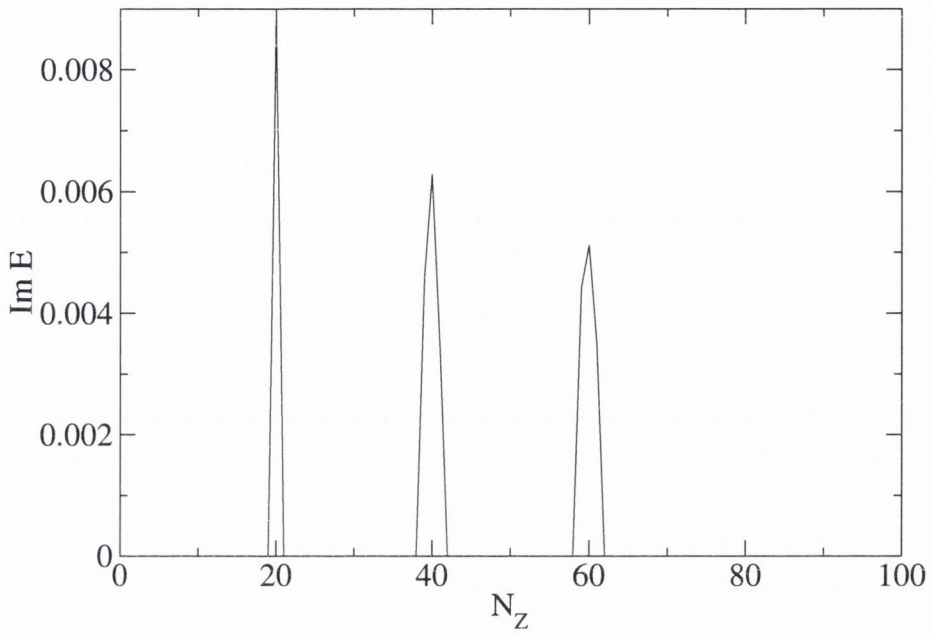

Figure 4-9: $\Im E$ vs N_z for the $\chi\chi$ states.

the appropriate values of N_z.

We have used several techniques in both the Euclidean and Minkowski formulations of perturbation theory to measure various important quantities in the model $\phi \rightarrow \chi\chi$. As the value of the coupling, λ, is sufficiently small, we would hope that there would be a strong agreement with the results of the Monte Carlo simulations, which will be discussed next.

	$N_z = 9$		$N_z = 12$		$N_z = 16$	
	$\vec{p}$	$\lvert\vec{p}\rvert/2\pi$	$\vec{p}$	$\lvert\vec{p}\rvert/2\pi$	$\vec{p}$	$\lvert\vec{p}\rvert/2\pi$
1	$(0,0,0)$	0	$(0,0,0)$	0	$(0,0,0)$	0
2	$(0,0,1)$	0.111	$(0,0,1)$	0.0833	$(0,0,1)$	0.0625
3	$(0,1,0)$	0.2	$(0,0,2)$	0.167	$(0,0,2)$	0.125
4	$(0,0,2)$	0.222	$(0,1,0)$	0.2	$(0,0,3)$	0.1875
5	$(0,1,1)$	0.229	$(0,1,1)$	0.216	$(0,1,0)$	0.2
6	$(0,0,3)$	0.333	$(0,0,3)$	0.25	$(0,1,1)$	0.32

Table 4.2: This table shows how the lowest six energy states differ for varyious values of N_z.

4.2 Monte Carlo Simulation Results

We now turn our attention to the results of the Monte Carlo integration of the correlation matrix. Firstly, let us look at the two particle spectrum in the $\lambda = 0$ case. This is done directly using the lattice dispersion relation (Eq. 4.11). The justification for using the lattice, rather than continuum, dispersion relation will be apparent when we investigate the one particle spectrum. We now encounter one of the problems with using brick shaped lattices; the ordering of the momentum states depends on the volume. For instance, we list the lowest five momenentum states in the free theory at $N_z = 9, 12, 16$ (Table4.2).

It is evident that momentum states can swap order because of the constancy of N_s. This is demonstrated quite dramatically when we look at the lowest ten states of the free spectrum in Fig. 4-10. We see states with $p_y = 0$ decaying to $2m_\chi$ and states with $p_y = 1$ dropping to $\sqrt{(4m_\chi^2 + (2\pi/5)^2}$, with the states crossing through each other, bring about this order swapping. As a consequence of this, care will be needed when operators are being constructed for the correlation matrix in the interacting case to ensure the lowest states are chosen at each N_z.

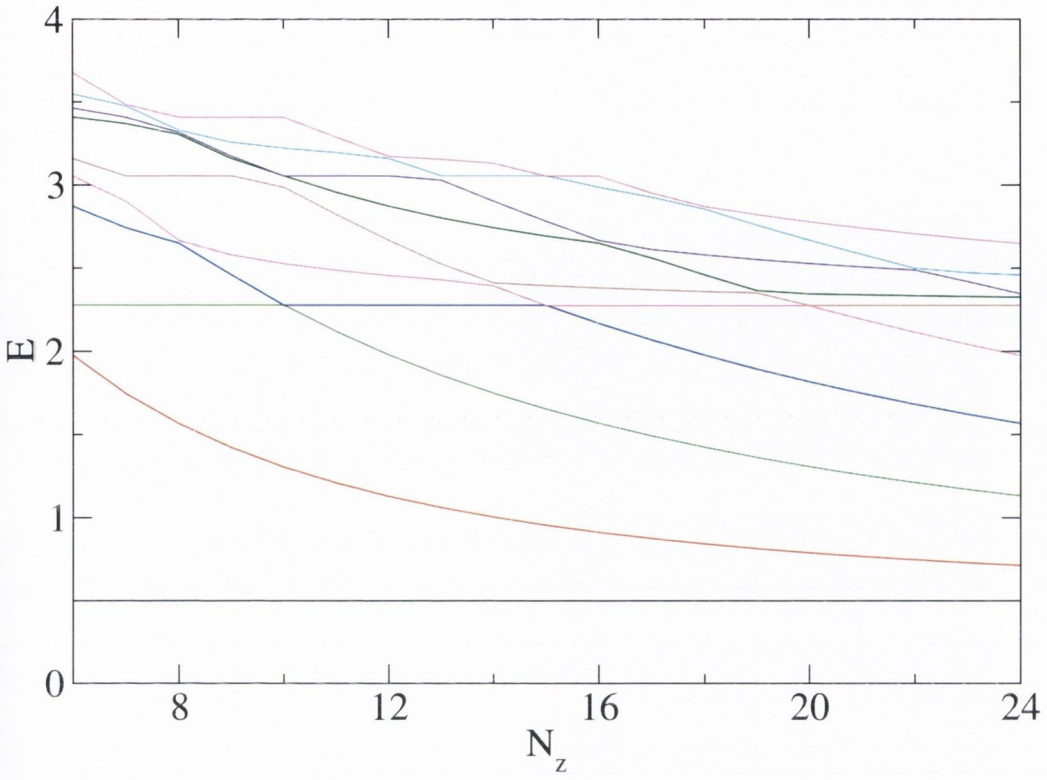

Figure 4-10: The lowest ten states of the free two particle spectrum

4.2.1 Single Particle Spectrum

The correlation of single χ states is carried out as follows.

$$C(t-t') = \langle \frac{1}{L^3} \sum_x \chi(\vec{x},t) e^{i\vec{p}\vec{x}} \frac{1}{L^3} \sum_y \chi(\vec{y},t') e^{-i\vec{p}\vec{x}} \rangle \tag{4.8}$$

To calculate the phase shift, we first must determine m_χ. This is done by correlating χ rest states ($\vec{p} = 0$ in Eq. 4.8). Including finite volume polarisation effects, we expect $m_\chi(L)$ to behave like

$$m_\chi(L) = m_\chi + \frac{ce^{-m_\chi N_z}}{N_s N_z^{1/2}}. \tag{4.9}$$

This is an adaptation of the formula used in [14] to the case of a lattice of spatial volume $N_s^2 \times N_z$. When the data is fit to this function we obtain $m_\chi = 0.3924(1)$. In Fig. 4-12, we see that this value fits well into the χ spectrum.

The χ dispersion relation is examined to ascertain whether the continuum dispersion relation

$$E(\vec{p}) = \sqrt{\vec{p}^2 + m_\chi^2} \tag{4.10}$$

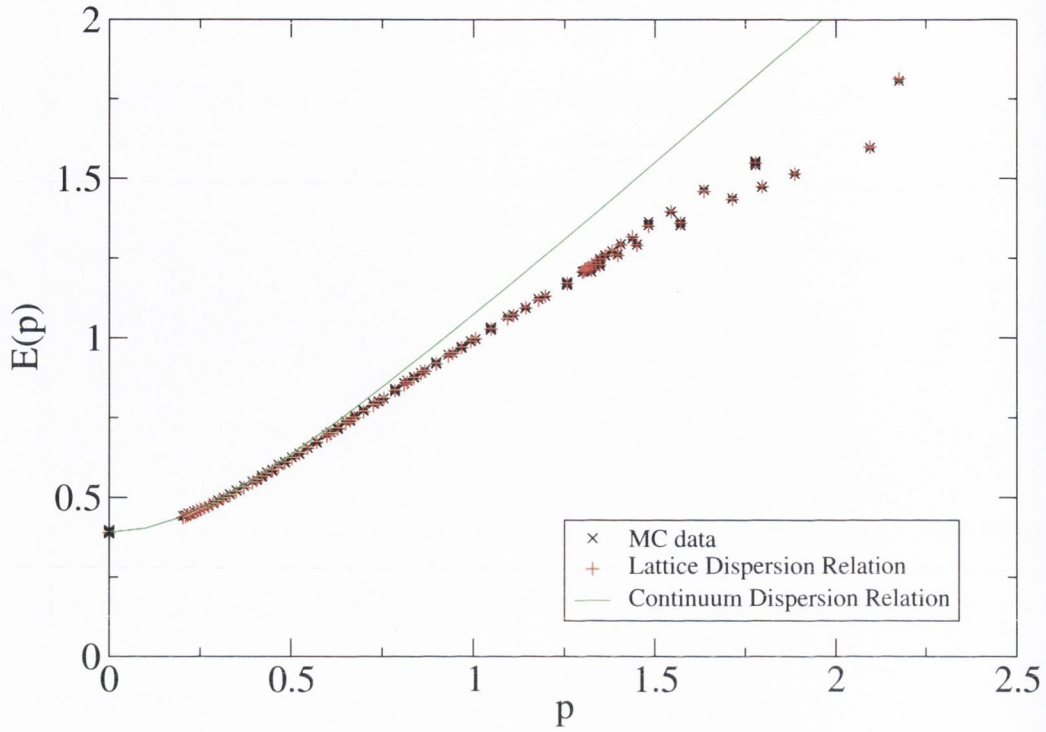

Figure 4-11: χ dispersion relation

holds in our simulations, or if the lattice alternative

$$\cosh(E(\vec{p})) - \cosh m_\chi = \sum_{i=1}^{3}(1 - \cos p_i) \tag{4.11}$$

is required. To this end, χ operators were constructed with the lowest momentum states of that volume. The energy of each operator was taken calculated from the exponential decay of the correlation function of the operator with itself. In Fig. 4-11, we have the dispersion relation. We see a strong agreement with the lattice dispersion relation (Eq. 4.11), but a large deviation from Eq. 4.10 at large p, due to the small spacial extent of the lattices. As a by-product of the investigation of the dispersion relation, we have the χ spectrum (Fig. 4-12).

4.2.2 Two Particle Spectrum

When constucting the correlation matrix in the two particle case, we must take the same precautions to ensure that the lowest states at each volume are chosen. Once this is done we can measure $C_{\alpha\beta}$ as prescribed. We then implement the diagonalisa-

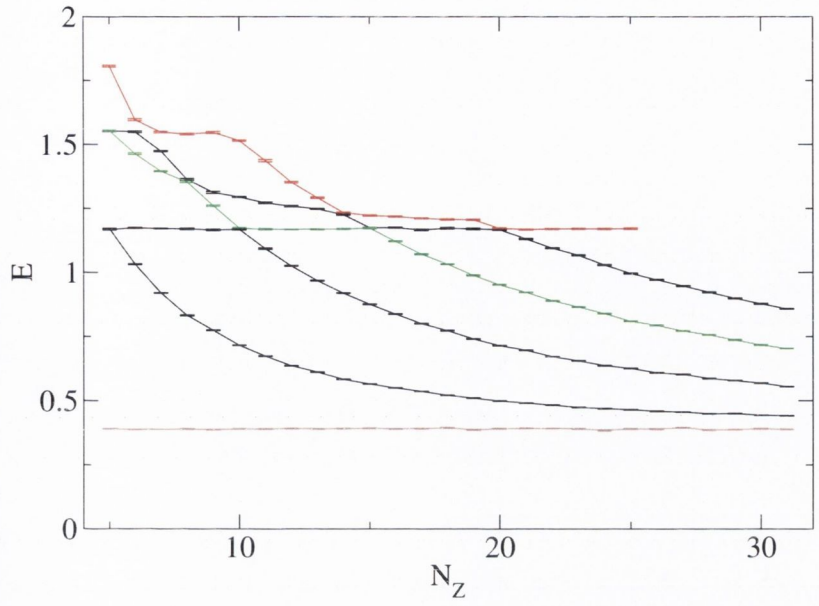

Figure 4-12: The five states of the χ spectrum measured using Monte Carlo integration. The solid line is included to make the avoided level crossings more evident.

tion procedure described previously, giving us exponentially decaying eigenfunctions which we can then fit to extract the energy of that state. The energy spectrum can be seen in Fig. 4-13. We can see the $(0,0,1)$ and $(0,0,2)$ states decaying to the constant $(0,0,0)$ state, crossing over the ϕ state. The error bars on the ϕ state energy levels drop dramatically between $N_z = 18$ and $N_z = 22$. Over this range of N_z, ϕ field is integrated out, as described previously in Sec. 3.2.2, leaving the Feynman propagator plus a stochastic contribution at $\mathcal{O}(\lambda^2)$. This results in a significant reduction the energy error bars for these values of N_Z.

In the vicinity of the level crossings, where the overlap between the states is non-negligible, it is possible to decompose the energy eigenstates, Ψ_a into the states represented by the correlation matrix using $\psi_a = C^{-1/2}(t_0)\Psi_a$. The normalised squares of the components, ψ_a indicate the composition of each eigenvector of the correlation matrix. We expect to see the individual energy states shift between the states constructed as the energy levels cross. In Fig. 4-14(a), we see how the second energy level is initially dominated by the $\phi \to \phi$ state, but switches to the first excited $\chi\chi \to \chi\chi$ state. In Fig. 4-14(b), as is to be expected, we see the third energy level mirror this transition. The dominance of the eigenvectors by one particular state immediately

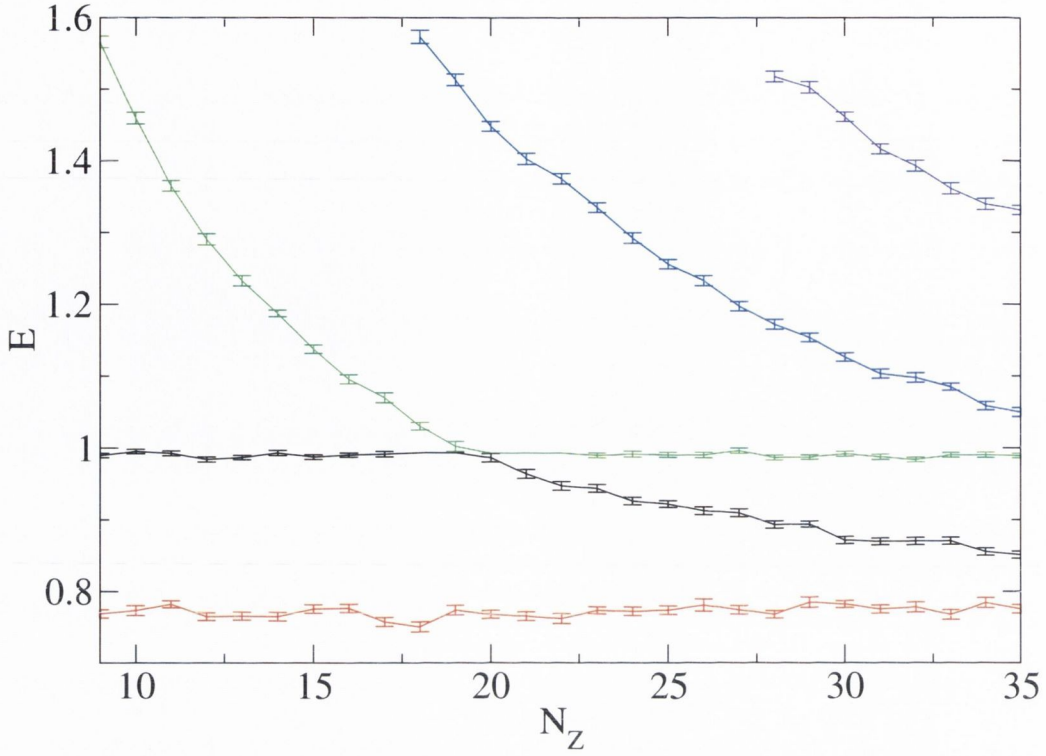

Figure 4-13: Two Particle Spectrum

either side of the level crossing justifies the omission of off-diagonal matrix elements away from this area.

4.2.3 Scattering Phase Shift and Decay Width

Using the method outlined previously in Sec. 3.2.4, we retrieve the associated momenta for each value of the energy. We then use these values to evaluate $\delta(p)$. These values of $\delta(p)$ were then fit to the Breit Wigner formula

$$\tan\left(\delta - \frac{\pi}{2}\right) = \frac{W^2 - m_\phi^2}{m_\phi \Gamma}. \tag{4.12}$$

While it would be ideal to fit to the perturbative form and extract values for the renormalised couplings, the uncertainties involved in fitting values this small render this approach impractical. Fitting data to a discontinuous function such as Eq. 4.12 presents problems to the standard Marquardt-Levenberg fitting algorithm. It is worthwhile to investigate this problem and discuss the solution.

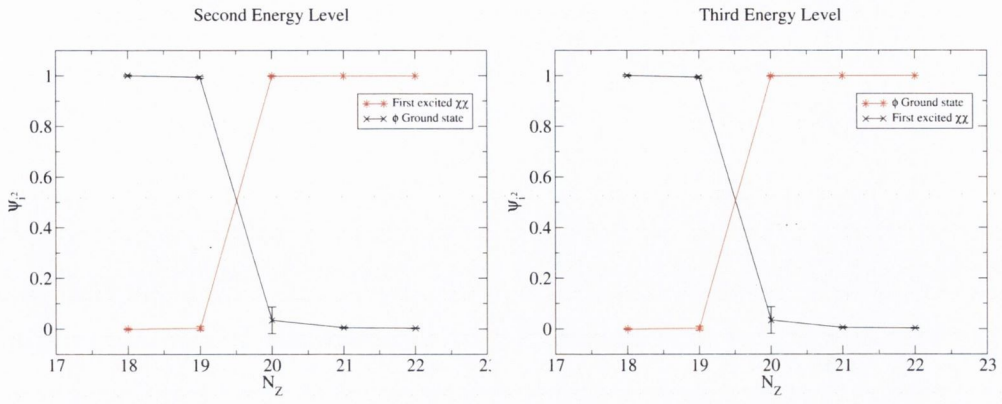

(a) Composition of Second Energy Level

(b) Composition of Third Energy Level

Figure 4-14: Crossings

A Genetic Fitting Algorithm

Our object is to find best fit values for M parameters, β_i, for a function $f(\beta_i; x_k)$, with N variables x_k, fitted to N data points, v_k. The standard approach to fitting data to a given function to extract the values of a set of parameters is to apply the Marquardt-Levenberg algorithm [40]. This is a numerical algorithm for solving the problem of minimising the function

$$\chi_i^2 = \frac{1}{N} \sum_{k=1}^{N} [f(\beta_i; x_k) - v_k]^2 \tag{4.13}$$

to give a least square fit. Starting with an initial parameter vector, β, it iteratively updates β using a first order Taylor expansion

$$f(x, \beta + \delta) \approx f(x, \beta) + J\delta. \tag{4.14}$$

Here, x represents the variables. The matrix, J, is associated with the derivatives of f with respect to the parameters, β_i. From here the iterative process can be reduced to solving a matrix inverse problem, involving the matrix J.

A problem occurs when one of the derivatives of f with respect to one of the parameters is discontinuous. In our case, the first derivative of Eq. 4.12 with respect

to m_ϕ is discontinuous in the region in which we are interested. A solution to this problem is to adapt a genetic algorithm for the purposes of fitting.

The principle of genetic algorithms [41] is to repeatedly "breed" a population of solutions to a problem. The parents are selected using some fitness function, which serves to ensure that favourable solutions are chosen with greater frequency. The algorithm also allows for random mutation of genes which assists in the exploration of the entire solution space. We will now examine the particulars of adapting such an algorithm for fitting.

Starting with a random initial population of R solutions, g_i, we obtain a χ^2 value for each gene using Eq. 4.13.

Let the lowest of these χ_i's be called χ_{best}, and the average χ^2 be χ_{ave}. Our aim is to "breed" a gene which minimises this χ^2 function. Thus, if a gene has a lower χ^2 value, it should be more likely to be chosen as a parent. Therefore, our fitness function is given by

$$G(g_i) = Ae^{(\chi^2_{best}-\chi^2_i)/\chi^2_{ave}}. \tag{4.15}$$

The value of A is used to normalise the χ^2 values such that

$$\sum_{i=1}^{R} G(g_i) = 1. \tag{4.16}$$

This means that

$$A = \frac{1}{\sum_{i=1}^{R} e^{(\chi^2_{best}-\chi^2_i)/\chi^2_{ave}}}. \tag{4.17}$$

We can now view the value of $G(g_i)$ as the probability of gene i being chosen as a parent. With this task completed, we turn our attention to the matter of combining the parent genes to produce favourable children. In a typical genetic algorithm this is done by bitwise exchanging segments of the parent genes. This proved to be an ineffective way of combining real, continuous values however,since large segments of the parent genes are bitwise identical for double precision numbers. A more satisfactory solution was to take a weighted average of the parent genes. Combining two genes, g_a and g_b, componentwise, to get g_c, we have

$$g_c^{(i)} = \frac{g_a^{(i)}G(g_a) + g_b^{(i)}G(g_b)}{G(g_a) + G(g_b)}. \tag{4.18}$$

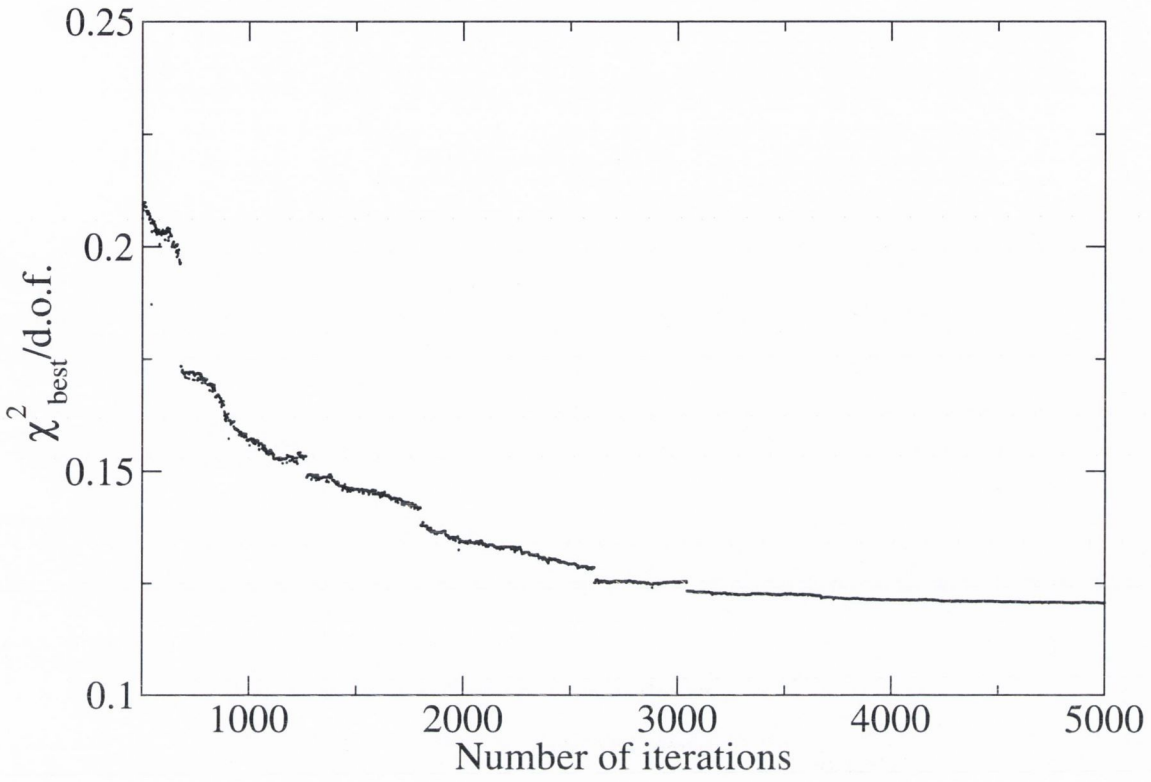

Figure 4-15: Plot of the lowest χ^2_{best} value of the population against the number of iterations for the genetic fitting algorithm.

Aside from receiving genes from the parents, genetic modification is also allowed by random mutations using a Poisson process. This is achieved by randomly adding a small amount to a value of $g(a)^{(i)}$. Also, using a Poisson process, we can bring about migration by randomly removing a gene and replacing it with a randomly assigned new values. These two processes ensure that the algorithm explores the entire phase space of solutions.

When this procedure has been applied many times, the resultant gene-pool will produce a gene with the ideal fit values of β_i. Fig. 4-15 shows a typical progression for the χ^2_{best} value as the algorithm iterates. The discrete drops in χ^2_{best} are caused by favourable mutations and migrations. In Fig. 4-16, we see a plot of δ vs p, along with a curve representing the fitted Breit Wigner function. A good agreement is seen between the fit function and the data over the range of the fit. Outside this range, the Breit-Wigner formulation is unreliable and the fit is less accurate. As in the perturbative case, only the ϕ state and the ground and first excited $\chi\chi$ states are

m_ϕ	$0.995 \pm 2 \times 10^{-3}$
m_χ	0.3924 ± 10^{-4}
Γ	$8.2(6) \times 10^{-3}$

Table 4.3: Fit values from Monte Carlo simulations.

included, due to large finite volume polarisation and finite lattice spacing effects in the higher $\chi\chi$ states. The values obtained from this fit for m_ϕ and Γ, together with the value of m_χ from the one particle spectrum, are presented in Table 4.2.3.

The value, $\Gamma = 8.2(6) \times 10^{-3}$ ($\chi^2/d.o.f. = 0.12$) is in reasonable agreement with the values obtained from the perturbative calculations, as is shown in Sec. 4.3.

4.2.4 Matrix Elements

In the next chapter, our interest will turn to the calculation of elements in $G \to \pi\pi$ correlation matrix. We will examine, in particular, the $G \to \pi\pi$ matrix element. At this point, we will briefly investigate the role of the corresponding $\phi \to \chi\chi$ element in the model theory. The importance of this element (given by $C_{0i}, \quad i \neq 0$ in the expansion below) in the perturbative calculation is evident when the expansion of the determinant of the correlation is examined;

$$\begin{aligned} \det C^{-1}(\Omega) &= \begin{vmatrix} C_{00_0} + \lambda^2 C_{00_2} & \lambda \mathbf{C_{01}} & \lambda \mathbf{C_{02}} & \cdots \\ \lambda \mathbf{C_{10}} & C_{11_0} + \lambda^2 C_{11_2} & 0 & \\ \lambda \mathbf{C_{20}} & 0 & C_{22_0} + \lambda^2 C_{22_2} & \\ \vdots & & & \end{vmatrix}^{-1} \\ &\approx \prod_{i=0}^{m} (C_{ii_0}^{-1} - \lambda^2 C_{ii_2}) + \lambda^2 \sum_{i=1}^{n} \mathbf{C_{0i}}^2 . \prod_{k=0}^{n} C_{kk_0}^{-2}. \end{aligned} \tag{4.19}$$

This matrix element is the only off-diagonal element to contribute at $\mathcal{O}(\lambda^2)$. To gain a more quantitative understanding of the importance of the $\phi \to \chi\chi$ correlator, $C_{0i}(t)$, in the Monte Carlo simulations, we examine (Fig. 4-17) the behaviour of $C_{0i}(0)$ in the region of the avoided level crossing. We see a discrete step in $C_{0i}(0)$ for all i at the avoided level crossing at $N_Z = 20$.This indicates this channel is very sensitive to

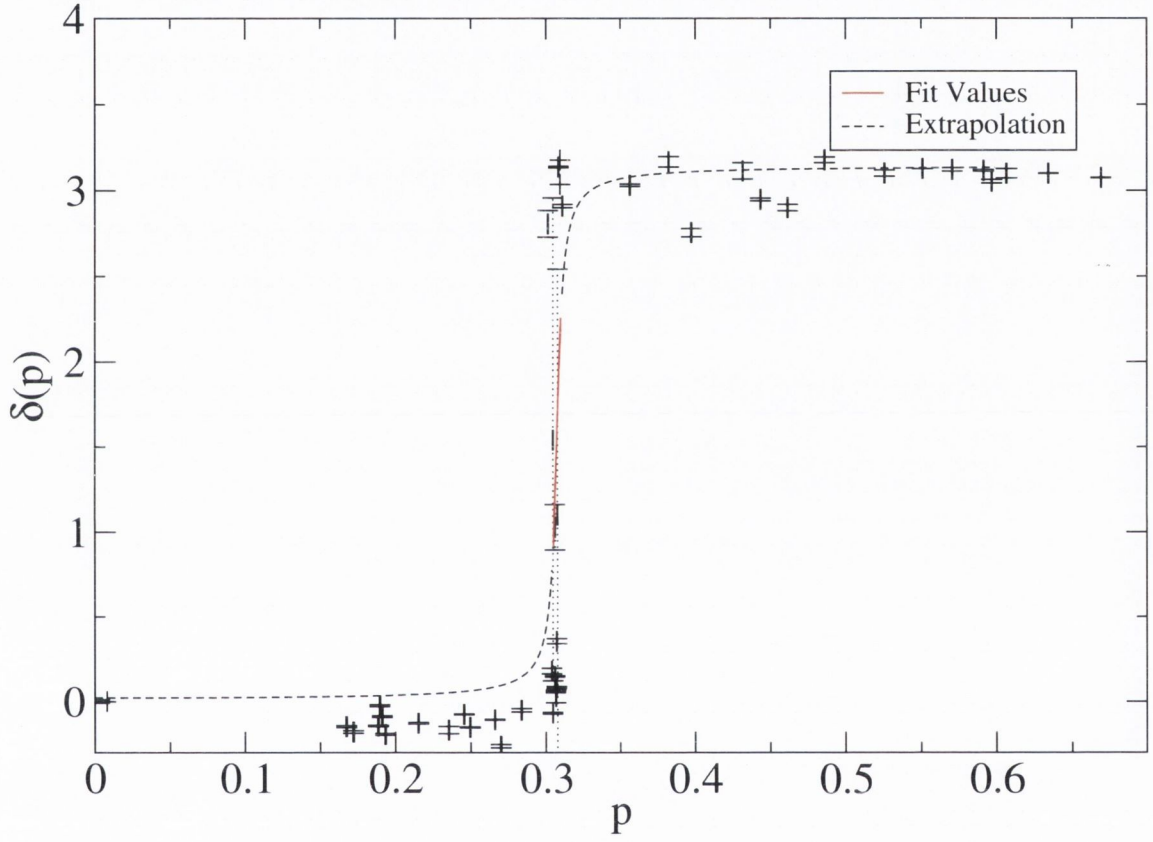

Figure 4-16: Plot of δ vs p with fit function. This shows the data along with the Breit-Wigner function associated with the fit values. The fit was performed over the range $\pi/4 < \delta < 3\pi/4$ and was extrapolated over other values of p.

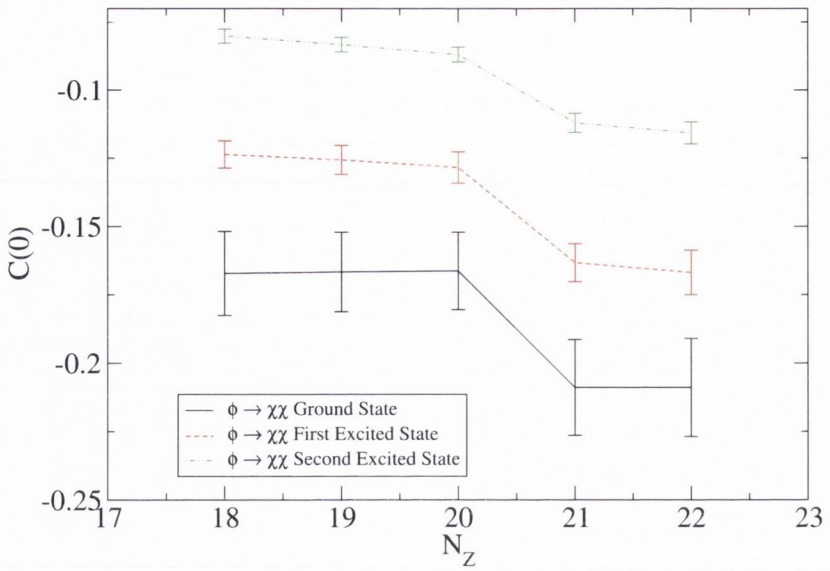

Figure 4-17: The behaviour of the $\phi \rightarrow \chi\chi$ correlator in the vicinity of the avoided level crossing.

the reordering of the states and an accurate measurement of this quantity is essential in the vicinity of the avoided level crossing.

4.3 Comparison of Perturbative and Monte Carlo Results

There are three points of contact between the two approaches. Firstly in Fig. 4-18, we see a plot of the two particle spectra from the perturbative and Monte Carlo simulations. We see a strong agreement between the two cases as would be expected for a small value of λ.

Fig. 4-19 shows a comparison of the scattering phase shift, $\delta(p)$, for the two cases. Again, the data for the two cases are relatively close. Discrepancies must be expected, as the two obey different dispersion relations, which will lead to a slight variation in the values of the momenta associated with each value of the energy.

Finally, we look at the three values obtained for the decay width of the ϕ particle, Γ. The two values from the perturbative calculations, as well as the Monte Carlo simulation value are shown in Fig. 4-20. The values all agree to about 10% accuracy.

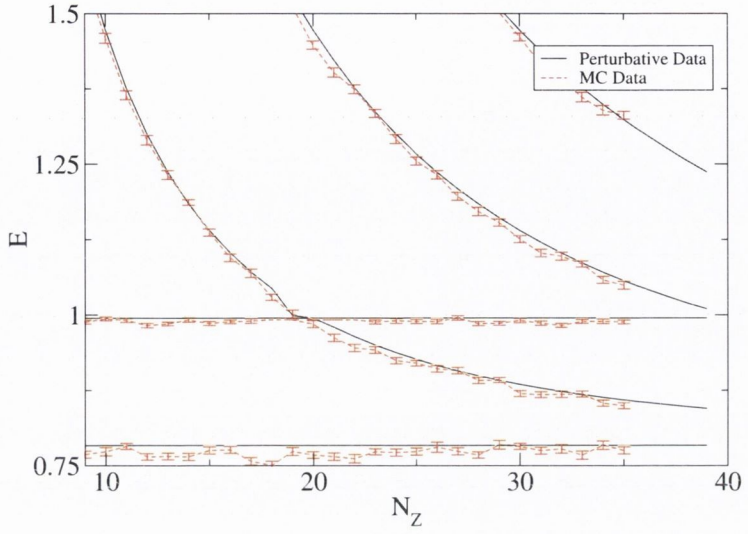

Figure 4-18: The two particle spectra from the perturbative and Monte Carlo simulations.

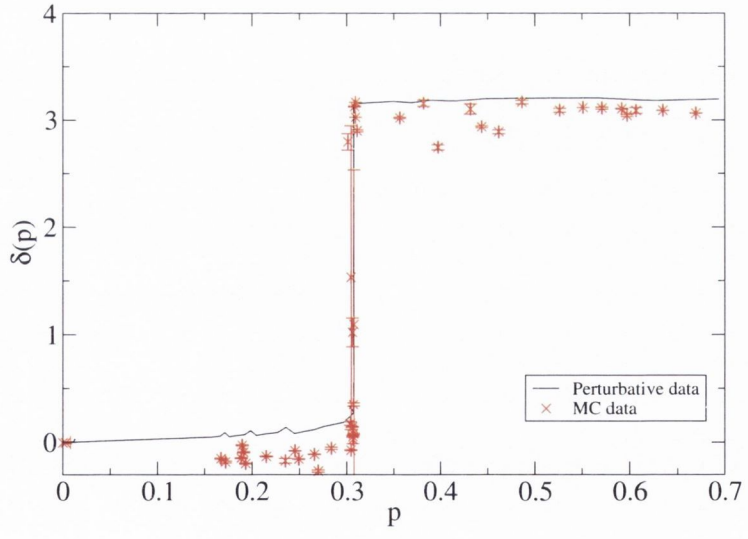

Figure 4-19: The scattering phase shift, $\delta(p)$, from the perturbative and Monte Carlo simulations.

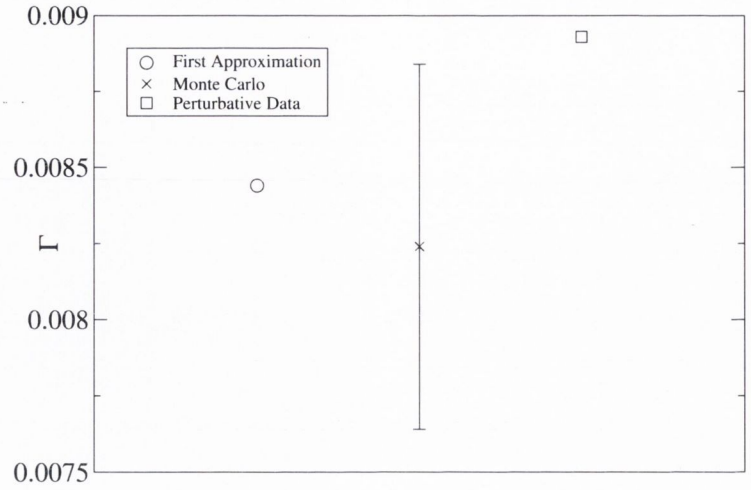

Figure 4-20: The decay width, Γ from the two perturbative calculations and Monte Carlo simulations.

As is to be expected when λ is small (0.5), the perturbative results compare well to the Monte Carlo data. To conclude the discussion of the model $\phi \rightarrow \chi\chi$ theory, we will present the results in an experimental format. To do this, we plot the probability density function, $f(E)$, analogous to the mass distributions measured in scattering experiments;

$$f(E) = \frac{A}{(E^2 - m_\phi^2) + m_\phi^2\Gamma^2} \tag{4.20}$$

A is a normalisation factor, which is set equal to 1. In Fig. 4-21, the function, $f(E)$, is plotted for the two estimates of Γ from perturbation theory (mass and coupling renormalisations, and Minkowski perturbation theory), as well as the Monte Carlo result, with upper and lower bounds. The value of Γ found in Minkowski perturbation theory does not have a value of m_ϕ naturally associated with it from our calculations. For this curve, m_ϕ was set to the bare value of 1. We have used various approaches in perturbation theory and Markov Chain Mote Carlo to evaluate the decay width, Γ, of the ϕ particle in the model $\phi \rightarrow \chi\chi$ theory. Our particular interest was in applying Lüscher's method to the Euclidean formulation of this theory, exploring all the issues raised in using this technique to calculate Γ. The value found in this manner was found to be in good agreement with the results from Minkowski perturbation theory.

Having gained experience in the $\phi \rightarrow \chi\chi$ model theory, our interest now lies in a preliminary investigation of the $G \rightarrow \pi\pi$ correlation matrix, with a view to a full

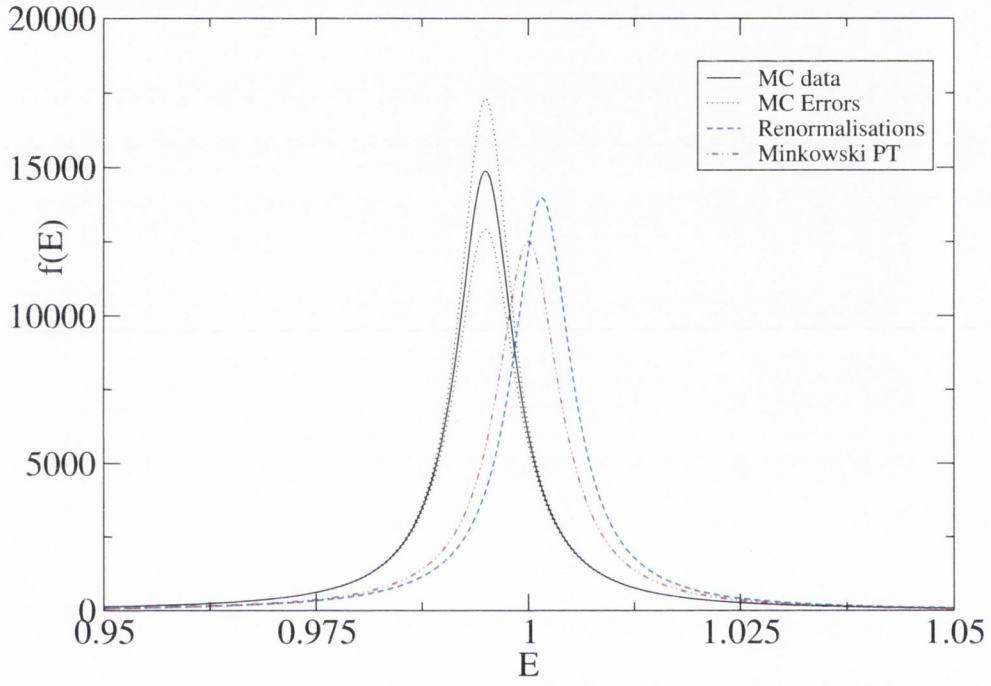

Figure 4-21: Probability density functions for $\phi \rightarrow \chi\chi$ results. Perturbative results from the mass and coupling renormalisation approach and Minkowski perturbation theory, as well as the Monte Carlo result with error bars are shown.

application of Lüscher's method to this interaction in the future.

Chapter 5

QCD

5.1 Glueballs in QCD

It is believed that all hadrons are made from quarks and gluons. So far, in all examined hadrons, the quark content has been greater than the gluon content. There is also, however, the possibility of hadronic states in which the gluonic contribution is dominant. Such states are known as *glueballs*. Glueballs are so exotic from the point of view of naïve quark model that their existence will be a direct support of QCD. Experimental endeavours to identify glueballs have been hampered by an inability to unambiguously identify glueball states. Several candidates have been isolated using many varied methods, with little clear consensus about which states actually correspond to glueballs.

As explained in Ref. [42], one approach is to attempt to group the experimentally observed scalar states into flavour multiplets. The states remaining after this process serve as a starting point for the identification of glueballs. Other distinctive features of glueball states, such as their abundance in gluon rich processes and their suppression in $\gamma\gamma$ reactions can, also serve as a guideline for the identification process. One scheme using this process [43] suggests $f_0(1370)$, $f_0(1500)$ or $f_0(1710)$ as glueballs. Although, Ref. [44] uses QCD factorisation based on an effective Lagrangian to suggest that $f_0(1710)$ has a large quark content. Another scheme [45] seems to point towards $f_0(600)$. Quantitative glueball results are available from QCD sum rules and Lattice

QCD. From QCD sum rules calculations, the lightest glueball state is predicted to have a mass of 1 GeV with a width into $\pi\pi$ of 1 GeV and a width into $\gamma\gamma$ of 0.2 keV ([46]).

For many years, Lattice QCD has been used as an *ab initio* tool for the exploration of the glueball spectrum. The following review of recent progress in the field is based on Ref. [7]. In pure $SU(3)$ Yang-Mills theory, the lowest lying glueball has a mass of 1700 MeV ([15]). In that particular study, a total of 13 glueballs with masses under 4 GeV were found with various J^{PC} states. Much of the work in quenched lattice QCD has concentrated on the lower spin states. Chen et al ([47]) reported the mass of the lightest scalar glueball to be 1710(50)(80) MeV, in agreement with the value found in Ref. [15]. The results suggest that there should be only two 0^{++} mesons between 1300 and 1800 MeV. This would imply that this observed glueball state is contained in the $f_0(1370)$, $f_0(1500)$ or $f_0(1710)$ states. Although, Ref. [48] examines the mixing between glueball and quark states and suggest that the $f_0(1710)$ state is 75% glueball. This result has been called into question [5].

Unquenched simulations [4, 5] have rethought this mixing of glueball and $q\bar{q}$ states and suggested a much lighter mass for the lightest flavour singlet 0^{++}. This would imply a stronger connection with the lighter $f_0(600)$ and $f_0(980)$ mesons. These simulations were carried out on coarse lattices, although Ref. [49] reports unquenched calculations with $a \sim 0.2$ fm. Thus far, continuum extrapolations have only been possible in the unquenched simulations. The dependence of glueball masses on the lattice spacing was found to be large unless Symanzik improved gauge actions are used, as in Ref. [50]. Also in unquenched studies, variational techniques are required to monitor the mixing of $q\bar{q}$ and glueball states with singlet scalar mesons. This was done by Hart [51].

It is clear that there are many approaches to the task of glueball identification, and while most sources agree that the glueball states account for some of the experimental resonances, there is little clear agreement about which exact ones. LQCD is at the forefront of the theoretical simulations of glueballs. In the coming sections, we will demonstrate the methods used in these calculations. The long term goal is to repeat

Lüscher's analysis on the $G \rightarrow \pi\pi$ interaction, as carried out previously in the model $\phi \rightarrow \chi\chi$ theory. New techniques and results will be provided which are central to the understanding of $G \rightarrow \pi\pi$ interaction, corresponding to the $\phi \rightarrow \chi\chi$ matrix element described in the model theory.

5.2 Simulating Glueballs

The spectrum of glueballs in QCD can be probed non-perturbatively using lattice techniques. To calculate the necessary transition matrix elements, very large statistics are needed for the Monte Carlo simulations. This prohibits large lattice size. On the other hand, the scale of the glueball masses requires a small lattice spacing in the temporal direction so that a reliable signal may be extracted from the correlator before it is lost to statistical noise. A compromise between these two conflicting requirements is provided by *anisotropic lattices*. In an anisotropic lattice, a large lattice spacing is used in the spatial directions to keep the computational size of the problem small, along with a small temporal lattice spacing which allows for a better signal detection. The spatial grid separation should be comparable to the size of the wavefuntion of the state (0.2 fm). The temporal lattice spacing should be given by the inverse of the energy scale being measured. In the case of glueballs, about 1.5 GeV. This corresponds to a length scale of about 0.12 fm. To allow a clear signal to develop in the simulations, a lattice spacing somewhat smaller than that is ideal.

In this section, we will discuss the topics necessary for simulation of glueballs on such anisotropic lattices. In many cases, these will analogous calculations to those in the model theory, while other topics will be case specific. Firstly we will examine the gauge and fermion actions, discussing the improvements, such as Symanzik and tadpole improvement of the gauge fields and ARIA actions for the fermion fields, which can be made to reduce discretisation errors. We will, then, investigate the operators used to form the correlation matrix in this theory. The process of smearing the operators to reduce spurious contributions from higher energy states will be discussed. Special consideration will be given to the expression of spin on a lattice. Having demonstrated all aspects of operator construction, we will investigate the for-

mation of the correlation matrix and the extraction of masses. Finally, the procedure of setting the scale to recover physical masses will be discussed.

5.2.1 Gauge Actions on a Lattice

Firstly, we address the discretisation of the gauge fields, which will be used to represent the glueball operators. Symanzik [52] and tadpole [53] improvements are used to remove some of the discretisation errors which occur in the naïve discretisation.

Symanzik Improvement

To remove all $\mathcal{O}(a^2)$ errors from all Green's function in lattice QCD at tree level in perturbation theory, it suffices to remove all $\mathcal{O}(a^2)$ artefacts from the action and the operators. With a view to removing these artefacts from the action, let us examine the Wilson lattice gauge action;

$$S_G^{SU(N)}[U] = \beta \sum_{x,\mu>\nu} \frac{1}{3} ReTr[1 - U_{\mu\nu}(x)] \tag{5.1}$$

where $\beta = 2N/g_0^2$. If we take with the temporal and spatial plaquette variables,

$$U_{sp} = U_i(x)U_j(x+\hat{i})U_i^\dagger(x+\hat{j})U^\dagger(x), \tag{5.2}$$

$$U_{tp} = U_t(x)U_j(x+\hat{t})U_t^\dagger(x+\hat{j})U^\dagger(x), \tag{5.3}$$

we can rewrite the Wilson discretisation in a way which has the correct naive continuum limit, respecting the anisotropic approach we have taken;

$$S_G[U] = \beta \left(\frac{1}{\xi_g} \Omega_{sp} + \xi_g \Omega tp \right) = \frac{1}{2} \int d^4x Tr F_{\mu\nu} F^{\mu\nu} + \mathcal{O}(a_s^2, a_t^2). \tag{5.4}$$

Here ξ is, at tree level, the anisotropy factor

$$\xi = a_s/a_t. \tag{5.5}$$

Also, we have split the temporal and spatial parts of the action, Ω_{tp} and Ω_{sp};

$$\Omega_{tp} = \sum_{x,i} \frac{1}{3} ReTr[1 - U_{tp}(x)] \tag{5.6}$$

$$\Omega_{sp} = \sum_{x,i<j} \frac{1}{3} ReTr[1 - U_{sp}(x)]. \tag{5.7}$$

At the tree-level in perturbation theory, any lattice operator, O, constructed from link variables will have an asymptotic expansion in powers of the spatial and temporal lattice spacings that can be written using a basis of local continuum operators of dimension $d = d_s + d_t$;

$$\mathcal{O} = \sum_d a_s^{d_s} a_t^{d_t} \sum_\alpha r_\alpha \mathcal{O}_\alpha^d. \tag{5.8}$$

These continuum operators respect all the symmetries of the anisotropic lattice and are also gauge invariant. There are two such dimension four operators;

$$\mathcal{O}_1^4 = g^2 \sum_{i,j} TrF_{ij}F_{ij} \tag{5.9}$$

$$\mathcal{O}_2^4 = g^2 \sum_i TrF_{it}F_{it} \tag{5.10}$$

There are no operators of this kind for dimensions less than four, none of dimension five and eighteen of dimension six. Let us write a general improved action in the form

$$S_G^{SU(N)} = \frac{2N}{g_0^2} \sum_x \sum_i c_i \mathcal{O}_i[U]. \tag{5.11}$$

To eliminate the $\mathcal{O}(a^2)$ errors in $\mathcal{O}$, we simply tune the coefficients, c_i, such that the coefficients of the dimension six operators vanish, and the coefficients of the dimension four operators are equal. Of the elementary loops available to us for this process, we follow the convention made in Ref. [50]. We use the sum over all spatial plaquettes, Ω_{sp}, temporal plaquettes, Ω_{tp}, 2×1 spatial rectangular loops, Ω_{sr}, and short temporal rectangles of one temporal and two spatial links, Ω_{str}.

$$\begin{aligned}
\Omega_{\rm sp} &= \sum_x \sum_{i>j} \tfrac{1}{3}{\rm ReTr}\left[1 - U_i(x)U_j(x+\hat{\imath})U_i^\dagger(x+\hat{\jmath})U_j^\dagger(x)\right], \\
\Omega_{\rm tp} &= \sum_x \sum_i \tfrac{1}{3}{\rm ReTr}\left[1 - U_t(x)U_i(x+\hat{t})U_t^\dagger(x+\hat{\imath})U_i^\dagger(x)\right], \\
\Omega_{\rm sr} &= \sum_x \sum_{i\neq j} \tfrac{1}{3}{\rm ReTr}\left[1 - U_i(x)U_i(x+\hat{\imath})U_j(x+2\hat{\imath})U_i^\dagger(x+\hat{\imath}+\hat{\jmath})U_i^\dagger(x+\hat{\jmath})U_j^\dagger(x)\right], \\
\Omega_{\rm str} &= \sum_x \sum_i \tfrac{1}{3}{\rm ReTr}\left[1 - U_i(x)U_i(x+\hat{\imath})U_t(x+2\hat{\imath})U_i^\dagger(x+\hat{\imath}+\hat{t})U_i^\dagger(x+\hat{t})U_t^\dagger(x)\right].
\end{aligned}$$

When we apply the above procedure to pin down the weights, c_i, we arrive at the action

$$S_{II} = \beta \left\{ \frac{5}{3\xi}\Omega_{\rm sp} + \frac{4\xi}{3}\Omega_{\rm tp} - \frac{1}{12\xi}\Omega_{\rm sr} - \frac{\xi}{12}\Omega_{\rm str} \right\}. \tag{5.12}$$

This action has $\mathcal{O}(a_t^2, a_s^4)$ errors. The $\mathcal{O}(a_t^2)$ errors can be removed by adding terms such as a rectangle with two temporal links and one spatial link. The improvement conditions can be altered slightly to remove the redundant high energy modes this will introduce. The remaining $\mathcal{O}(a_t^2)$ contributions are suppressed by ξ^4, as given in Eq. 5.5.

Tadpole Improvement

When we represent the gauge fields in terms of an exponential, $U_\mu(x) = e^{iag_0 A_\mu(x)}$, we introduce terms with vertices with an arbitrary number of gauge fields. The higher contributions are lattice artefacts. Contracting the gauge fields in these terms leads to ultra-violet divergences from tadpole diagrams. Since tadpole contributions are generally process independent, it is possible to measure their effect in one quantity and correct for this elsewhere. To proceed, we rewrite the gauge fields in terms of an infrared and an ultraviolet part;

$$U_\mu(x) = e^{iag_0 A_\mu(x)} = e^{iag_0(A_\mu^{IR}(x) + A_\mu^{UV}(x))} = u_0 e^{iag_0 A_\mu^{IR}(x)} \equiv u_0 \tilde{U}_\mu(x) \tag{5.13}$$

This new field is much closer to the continuum value, since the ultraviolet effects from the tadpoles have been divided out, giving a better agreement between perturbative and non-perturbative calculations. Extending this idea to the anisotropic case, we have

$$U_i = u_s \tilde{U}_i(x) \tag{5.14}$$

$$U_t = u_t \tilde{U}_t(x). \tag{5.15}$$

One common choice of tadpole factors are the fourth root of the plaquettes, $\langle \frac{1}{3} \Re \mathrm{Tr} U_{sp} \rangle$ and $\langle \frac{1}{3} \Re \mathrm{Tr} U_{tp} \rangle$. In Landau gauge perturbation theory,

$$1 - \left\langle \frac{1}{3} \Re \mathrm{Tr} U_{tp} \right\rangle \propto \frac{a_t^2}{a_s^2}. \tag{5.16}$$

Since, on our anisotropic lattices, $a_t \ll a_s$, we set $u_t = 1$. Rewriting our action (5.12) with tadpole improvement, we have

$$S_{II} = \beta \left\{ \frac{5}{3} \frac{\Omega_{\mathrm{sp}}}{\xi u_s^4} + \frac{4}{3} \frac{\xi \Omega_{\mathrm{tp}}}{u_s^2 u_t^2} - \frac{1}{12} \frac{\Omega_{\mathrm{sr}}}{\xi u_s^6} - \frac{1}{12} \frac{\xi \Omega_{\mathrm{str}}}{u_s^4 u_t^2} \right\}. \tag{5.17}$$

5.2.2 Fermion Actions on a Lattice

It is substantially harder to construct a lattice description of fermion fields. A naive attempt to discretise the fermion will lead to the doubler problem, described at length in [36]. A solution to this problem was proposed by Wilson. In doing so, however, he breaks chiral symmetry at $\mathcal{O}(a)$. These errors are prohibitively large for the use of Wilson fermions on coarse lattices. If we use field redefinitions which involve free parameters, we will have redundant couplings which can be set to remove doublers. One such class of actions are the $D234$ actions.

$D234$ Actions

Up to the existence of doublers, a naive description of fermions given by the operator $\gamma.\nabla + m$, using an improved lattice derivative

$$\nabla_{c\mu} = \nabla_\mu \left(1 - \frac{1}{6}a_\mu^2 \Delta_\mu\right) = D_\mu + \mathcal{O}(a^4), \tag{5.18}$$

where

$$\Delta_\mu = \frac{1}{a_\mu^2}\left(U_\mu(x)\psi(x+\hat{\mu}) + U_\mu^\dagger(x-\hat{\mu})\psi(x-\hat{\mu}) - 2\psi(x)\right) \tag{5.19}$$

will yield a lattice action with $\mathcal{O}(a^4)$ errors. The simplest way to remove the doublers without introducing any leading order errors is to perform a field redefinition in the continuum and, only then, discretise the action. In the continuum, the action is

$$\int \bar{\psi}_c M_c \psi_c = \int d^4x \bar{\psi}_c (D + m_c)\psi_c \tag{5.20}$$

We redefine the field;

$$\begin{aligned} \psi_c &= \Omega_c \psi_c \\ \bar{\psi}_c &= \bar{\psi}_c \bar{\Omega}_c \\ \bar{\psi}_c M_c \psi_c &= \bar{\psi}_c M_\Omega \psi_c \\ M_\Omega &= \bar{\Omega}_c M_c \Omega_c. \end{aligned} \tag{5.21}$$

The canonical choice of field redefinition is

$$\begin{aligned} \bar{\Omega}_c &= \Omega_c \\ \bar{\Omega}_c \Omega &= 1 - \frac{r a_t}{2}(D - m_c). \end{aligned} \tag{5.22}$$

Expanding the transformed fermion operator gives us

$$M_\Omega = m_c\left(1+\frac{1}{2}ra_t m_c\right) + D - \frac{1}{2}\left(\sum_\mu D_\mu^2 + \frac{1}{2}\sigma.F\right). \tag{5.23}$$

The Hermitean $\sigma_{\mu\nu}$ matrices are defined by

$$\sigma_{\mu\nu} = -\frac{i}{2}[\gamma_\mu, \gamma_\nu] = -\sigma_{\nu\mu}. \tag{5.24}$$

We have used

$$\frac{1}{2}\{\gamma_\mu D_\mu, \gamma_\nu D_\nu\} = \delta_{\mu\nu} D_\mu^2 + \frac{1}{2}\sigma_{\mu\nu}F_{\mu\nu}. \tag{5.25}$$

The lattice version of the field strength tensor, $F_{\mu\nu}$, is given by the clover term [54];

$$iF_{\mu\nu} = \frac{1}{8}(f_{\mu\nu} - f_{\mu\nu}^\dagger), \tag{5.26}$$

where $f_{\mu\nu}$ is the sum of four one-by-one oriented loops of links, starting at x. The upper right corner is

$$U_\mu(x)U_\nu(x+\hat{\mu})U_\mu(x+\hat{\nu})^\dagger U_\nu(x)^\dagger. \tag{5.27}$$

Using leading order discretisations of the derivatives gives us the Sheikholeslami-Wohlert action on an anisotropic lattice;

$$M_{SW} = m_c\left(1+\frac{1}{2}ra_t m_c\right) + \gamma.\nabla - \frac{ra_t}{2}\sum_\mu \Delta_\mu - \frac{1}{4}ra_t\sigma.F. \tag{5.28}$$

This action gives the doublers a large mass at the cut-off scale for any $r > 0$ and no doublers at $r = 1$. Taking these expansions of continuum derivatives to the next order gives the class of D_{234} actions;

$$\begin{aligned} M_{D234} &= m_c\left(1+\frac{1}{2}ra_t m_c\right) + \sum_\mu \gamma_\mu \nabla_\mu (1 - b_\mu a_\mu^2 \Delta_\mu) \\ &\quad -\frac{1}{2}ra_t\left(\sum_\mu \nabla_\mu + \frac{1}{2}\sigma.F\right) + \sum_\mu c_\mu a_\mu^3 \nabla_\mu^2 \end{aligned} \tag{5.29}$$

$D234$ Actions on Anisotropic Lattices and ARIA

As was discussed previously in Sec.5.2, the energy scales being simulated require lattice spacing of about 0.04 fm.This cannot be achieved on an isotropic lattice as the cost of the simulations scales as $\mathcal{O}(a^4)$. The use of an anisotropic lattice

greatly alleviates this problem, however, such a lattice has less axis permutation symmetry, resulting in the anisotropic action having more independent coefficients. At the quantum level, some of these coefficients must be tuned to restore space-time exchange symmetry. To derive a $D234$ class action for an anisotropic lattice, the allowed operators at $\mathcal{O}(a)$ consist of the spatial and temporal parts of the Wilson and clover term, and $[\gamma_t D_t, \sum \gamma_i D_i]$. The most general field transformations lead to three redundant operators, so two coefficients remain to be tuned at $\mathcal{O}(a)$.These can be chosen to be the spatial and temporal parts of the clover. On an anisotropic lattice, one must also allow a relative coefficient between the temporal and spatial kinetic terms. This can be tuned non-perturbatively, by imposing, for example, a relativistic dispersion relation for the pion. Thus our $D234$ action for an anisotropic lattice is

$$\begin{aligned} M_{D234}^{Anis} &= m_0 + \sum_\mu v_\mu \gamma_\mu \nabla_\mu (1 - b_\mu a_\mu^2 \Delta_\mu) \\ &\quad -\frac{1}{2} a_t \left(\sum_\mu r_\mu \Delta_\mu + \sum_{\mu<\nu} c_{SW}^\mu \sigma_{\mu\nu} F_{\mu\nu} \right) + \sum_\mu V_\mu d_\mu A_\mu^3 \Delta_\mu^2 \end{aligned} \tag{5.30}$$

From the field redefinition, Eq. 5.22, for a fixed Wilson parameter, r, we recover spatial doublers in the anisotropic case, since $\Omega_c \to 1$ as $a_t \to 0$. To construct such a redefinition suitable for the anisotropic case, let us write

$$\bar{\Omega}_c \Omega_c = 1 - \frac{r a_t}{2} (\gamma_0 D_0 - m_c). \tag{5.31}$$

This sets some of our free parameters;

$$\begin{aligned} (v_0, v_i) &= (1, \mu_r) \\ (c_{SW}^0, c_{SW}^i) &= \left(0, \frac{1}{2}\right) \\ (r_0, r_i) &= (r, 0) \end{aligned} \tag{5.32}$$

Improving temporal derivatives is problematic since it necessarily involves including increasingly non-local contributions which introduce lattice ghosts. To circumvent this, we retain the one-hop improvement of the field redefinition, but remove the

improved temporal discretisation. This amounts to setting the parameters as follows;

$$\begin{aligned}(b_0, b_i) &= \left(0, \frac{1}{6}\right) \\ (d_0, d_i) &= (0, s).\end{aligned} \tag{5.33}$$

The removal of spatial doublers is ensured by choosing $b_i = 1/6$ and $d_i = s$. Putting all this together gives us our final fermion action;

$$\begin{aligned}M_{ARIA}\psi(x) &= \frac{1}{a_t}\Bigg[\left(\mu_r m a_t + \frac{18s}{\xi} + r + \frac{r a_t^2 g}{4}\sigma_{i0}F_{i0}\right)\psi(x) \\ &\quad -\frac{1}{2u_t}[(r-\gamma_0)U_t(x)\psi(x+\hat{t}) + (r+\gamma_0)U_t^\dagger(x-\hat{t})\psi(x-\hat{t})] \\ &\quad -\frac{1}{\xi_q}\sum_i\left(\frac{1}{u_s}\left(4s - \frac{2}{3}\mu_r\gamma_i\right)U_i(x)\psi(x+\hat{i})\right. \\ &\quad +\frac{1}{u_s}\left(4s + \frac{2}{3}\mu_r\gamma_i\right)U_i^\dagger(x-\hat{i})\psi(x-\hat{i}) \\ &\quad -\frac{1}{u_s^2}\left(s - \frac{1}{12}\mu_r\gamma_i\right)U_i(x)U_i(x+\hat{i})\psi(x+2\hat{i}) \\ &\quad \left.-\left(s + \frac{1}{12}\mu_r\gamma_i\right)U_i^\dagger(x-\hat{i})U_i^\dagger(x-2\hat{i})\psi(x-2\hat{i})\right)\Bigg]\end{aligned} \tag{5.34}$$

At tree level, the fermion anisotropy, ξ_q, is given by $\xi = a_s/a_t$. We call the action here ARIA; Anisotropic, Rotated, Improved Action. Its leading errors are at $\mathcal{O}(a_t^2, a_s^3)$.

5.2.3 Distillation

To smear quark fields, a new method called "*distillation*" was used. The usual gauge-covariant smearing algorithm uses an approximate representation of the function

$$\Box = \exp\left(\sigma^2\nabla^2\right) \tag{5.35}$$

with ∇^2 the gauge covariant Laplace operator and σ a free parameter. A typical choice of σ means a very small number of modes contribute to the smearing operator, and a truncation can be introduced while maintaining a good smearing method. The method constructs a small vector space of "smooth" fields by finding the lowest N eigenvectors of ∇. In this simple test, $N = 16$ was used. These vectors are then used to construct a smearing operator on fields on sites of the lattice;

$$\Box(\underline{x},\underline{y}) = \sum_{i=1}^{N} v(x) \otimes v^*(y) \tag{5.36}$$

Then it is seen that all correlation function of smeared fields can be computed using just $O(N)$ inversions, which requires a modest amount of computer time.

A correlation function such as the pion-pion correlator becomes

$$\begin{aligned} C_\pi &= \text{Tr } \Box M^{-1} \Box \gamma_5 \Box M^{-1} \Box \gamma_5 \\ &= \text{Tr } (v^* M^{-1} v)\gamma_5 (v^* M^{-1} v)\gamma_5 \\ &= \text{Tr } (v^* M^{\dagger -1} v)(v^* M^{-1} v) \end{aligned} \tag{5.37}$$

where in the last step, γ_5-hermiticity of the quark operator has been used;

$$M^\dagger = \gamma_5 M \gamma_5. \tag{5.38}$$

Note that since all elements of the propagation matrix between eigenvectors i and j, $\mathcal{P}_{ij} = v^{*i} M^{-1} v^j$ can be computed, the method provides all-to-all propagation from the vector space of smooth fields, allowing accurate Monte Carlo measurements of many diagrams that are typically noisy, such as those including disconnected quark lines. These disconnected diagrams will be needed to measure correlation between glueball operators and two-pion states.

5.2.4 Glueball Operator Construction

To achieve the goal of extracting the energy states from the correlation matrix, as in our model theory, we must create a set of operators corresponding to glueball and $\pi\pi$ states, analogous to the ϕ and $\chi\chi$ states we had previously.

One major difference between the $\phi \to \chi\chi$ model and the current model is that the glueball and $\pi\pi$ states have non-trivial J^{PC}. The mass of a glueball with a given J^{PC} can be extracted from the large t behaviour of the correlation function, $C(t) = \langle 0|\bar{\Phi}^{(R)\dagger}(t)\bar{\Phi}^{(R)\dagger}(0)|0\rangle$, where R denotes the lattice irrep corresponding to the J^{PC} in question. The operator, $\bar{\Phi}^{(R)}(t) = \Phi^{(R)}(t) - \langle 0|\Phi^{(R)}(t)|0\rangle$, is a gauge invariant, translationally invariant, vacuum subtracted operator, which creates a glueball from the QCD vacuum.

Smearing

The construction of operators which overlap strongly with the glueball energy eigenstates of the system is important to ensure that contamination from higher energy states becomes negligible before statistical noise masks the signal. One method widely employed to reduce the effect of higher modes is *smearing*. Two spatial smearing schemes were used in the operator construction. In the one link scheme, a spatial link, $U_j(x)$, is replaced by a weighted sum of itself plus the four spatial staples along that link, projected into $SU(3)$:

$$U_j^s(x) = \mathcal{P}_{SU(3)} \left\{ U_j(x) + \lambda_s \sum_{\pm(k \neq j)} U_k(x)\, U_j(x+\hat{k})\, U_k^\dagger(x+\hat{j}) \right\}, \tag{5.39}$$

where $\mathcal{P}_{SU(3)}$ denotes projection into $SU(3)$. We denote this smearing scheme by s_{λ_S}. In double link smearing, superlinks of length $2a_s$ are constructed using staples connecting sites separated by a distance twice that of the length of the source link variable:

$$\begin{aligned} U_j^f(x) &= \mathcal{P}_{SU(3)} \Big\{ U_j(x)\, U_j(x+\hat{j}) \\ &+ \lambda_f \sum_{\pm(k \neq j)} U_k(x)\, U_j(x+\hat{k})\, U_j(x+\hat{j}+\hat{k})\, U_k^\dagger(x+2\hat{j}) \Big\}, \end{aligned} \tag{5.40}$$

and we denote this mapping by f_{λ_f}. These individual schemes were composed with each other to give six *smoothing schemes*, $\mathcal{S}_i$. The paths for these basic operators are shown in Fig. 5-1, taken from [50].

5.2.5 Spin on a Lattice

In the continuum a glueball state is described by its spin (i.e. its transformation properties under $SO(3)$), J, and its behaviour under charge conjugation, C, and spatial inversion, P. The allows us to attach a label J^{PC}. The lattice reduces the symmetry of the states. Rather than being determined by the state's action under $SO(3)$, the spin now depends on how the state behaves under the octahedral point group, O. O has 24 elements given by the proper rotations, divided across five conjugacy classes.The single valued irreducible representations are A_1, A_2, E, T_1 and

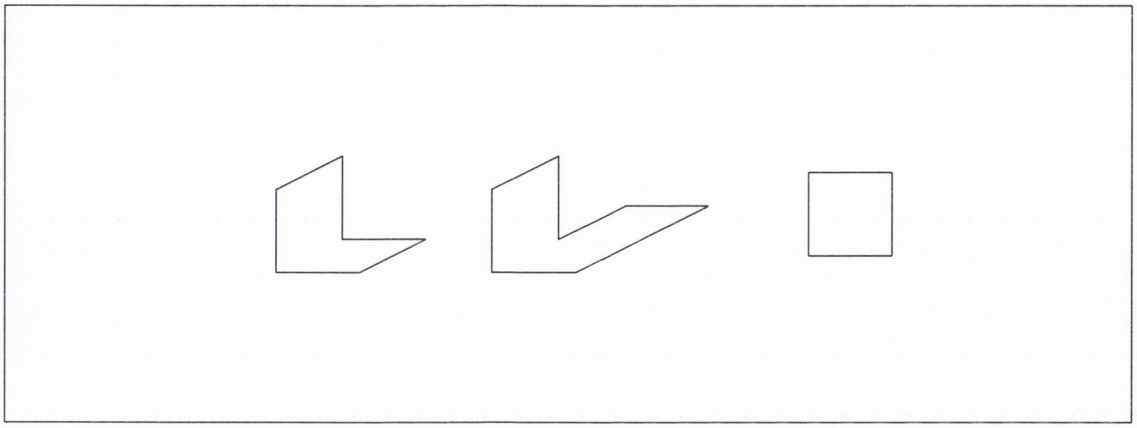

Figure 5-1: The Wilson loop shapes used to form the lattice glueball operators, labelled Operator 1, Operator 2 and Operator 3, respectively.

T_2, with dimension 1, 1, 2, 3 and 3 respectively. When spatial inversion is taken into account, the symmetry group becomes $O_h = O \otimes C_i$. C_i is the two element group containing the identity and spatial inversion elements. The remaining symmetry to be taken into account is charge conjugation. Thus we can refer to the full symmetry group of zero momentum on a cubic lattice as O^{PC}; the irreps are labelled A_1^{PC}, A_2^{PC}, E^{PC}, T_1^{PC} and T_2^{PC}. Having established the symmetry group on a lattice, we must now examine how to retrieve the continuum symmetry, J^{PC}, of a state with a discrete symmetry O^{PC}. To do this, we match the degeneracies observed in the lattice simulations with a given O^{PC} to those expected for the various J^{PC}. For example, if two degenerate states appeared in the E and T_2 channels, we could associate this with a spin 2 state in the continuum. A table of the number of times an irrep of $\mathcal{O}$ occur in the subduced representations, $J \downarrow \mathcal{O}$ of $SO(3)$ restricted to O are given in Table 5.1, from [15].

5.2.6 Correlation Matrices

Once we have constructed glueball states, we now form a correlation matrix, C_{AB}:

$$C_{AB}(t) = \sum_{\tau} \langle 0 | \bar{\Phi}_A^{(R)}(\tau+t)\ \bar{\Phi}_B^{(R)}(\tau) | 0 \rangle. \tag{5.41}$$

Table 5.1: Number of times each irreducible representation of the octahedral group O occurs in the subduced representations $J \downarrow O$ of the rotation group $SO(3)$ restricted to subgroup O.

J	A_1	A_2	E	T_1	T_2
0	1	0	0	0	0
1	0	0	0	1	0
2	0	0	1	0	1
3	0	1	0	1	1
4	1	0	1	1	1

The operators, $\bar{\Phi}_{\alpha}^{(R)}(\tau)$, are given by

$$\Phi_1^{(R)}(\tau) = \sum_x ReTrU_c(t) \tag{5.42}$$

$$\Phi_2^{(R)}(\tau) = \pi_1(\tau)\pi_{-1}(\tau). \tag{5.43}$$

Here, U_c is a closed path ordered product around the closed loops of Fig. 5-1 and

$$\pi_1(\tau) = \sum_{\vec{x}} \bar{u}(\vec{x},\tau)\gamma_5 d(\vec{x},\tau) \tag{5.44}$$

$$\pi_{-1}(\tau) = \sum_{\vec{x}} \bar{d}(\vec{x},\tau)\gamma_5 u(\vec{x},\tau), \tag{5.45}$$

where u and d are distilled fields. Fig. 5-2 shows the three types of correlation functions which make up the correlation matrix. To date, only the disconnected part of the $\pi\pi \rightarrow \pi\pi$ diagram has been evaluated. The connected contributions are expected to be less noisy. We now follow the path laid out in Sec. 3.2.3 to recover the energy spectrum from the correlation matrix, as for the $\phi \rightarrow \chi\chi$ model.

So far, the simulations have advanced to this point. It is, however, beneficial to look at the remaining steps in the process of calculating the energies, some of which were not necessary in the $\phi \rightarrow \chi\chi$ case.

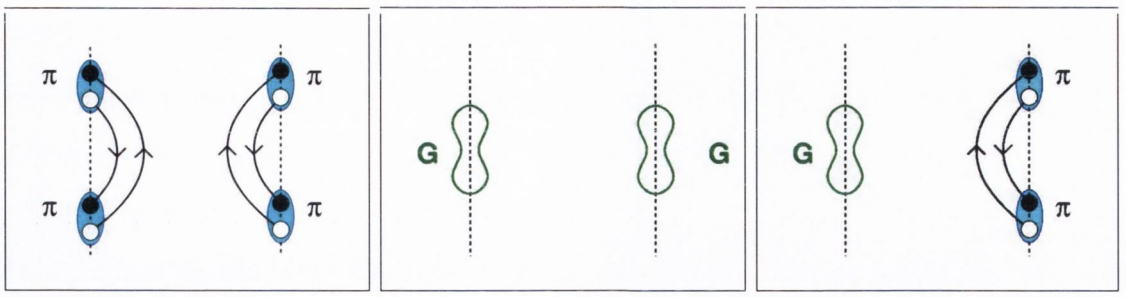

Figure 5-2: Correlation functions making up the correlation matrix.

Variational Method

The last step in the operator construction process is to combine these "building blocks" in a sensible way to guarantee a maximal overlap with the lowest lying glueball in the channel of interest. A general linear combination of the basic operators is formed;

$$\Phi^{(R)}(t) = \sum_{\alpha=1}^{N} v_\alpha^{(R)} \phi_\alpha^{(R)}(t). \tag{5.46}$$

The coefficients, $v_\alpha^{(R)}$, are determined using the variational method; by minimising the effective mass

$$\tilde{m}(t_D) = -\ln \left[\frac{\sum_{\alpha\beta} v_\alpha^{(R)} v_\beta^{(R)} \tilde{C}_{\alpha\beta}(t_D)}{\sum_{\alpha\beta} v_\alpha^{(R)} v_\beta^{(R)} \tilde{C}_{\alpha\beta}(0)} \right], \tag{5.47}$$

with respect to $v_\alpha^{(R)}$. $\tilde{C}_{\alpha\beta}$ is the correlation matrix,

$$\tilde{C}_{\alpha\beta}(t) = \sum_{\tau} \langle 0|\bar{\phi}_\alpha^{(R)}(\tau+t)\, \bar{\phi}_\beta^{(R)}(\tau)|0\rangle. \tag{5.48}$$

of vacuum subtracted operators $\bar{\phi}_\alpha^{(R)}(t) = \phi_\alpha^{(R)}(t) - \langle 0|\phi_\alpha^{(R)}(t)|0\rangle$. Let $\mathbf{v}^{(R)}$ denote a column vector whose elements are the optimal values of the coefficients $v_\alpha^{(R)}$. The minimisation criterion reduces to solving the eigenvalue problem

$$\tilde{C}(t_D)\ \mathbf{v}^{(R)} = e^{-\tilde{m}(t_D)}\ \tilde{C}(0)\ \mathbf{v}^{(R)}. \tag{5.49}$$

The eigenvector, $\mathbf{v^{(R)}}$ corresponding to the largest eigenvalue, $e^{-\tilde{m}_0(t_D)}$, gives us the values of $v_{0\alpha}^{(R)}$ which correspond to the operator $\Phi_0^{(R)}(t)$, best overlapping with the ground state of the glueball in the channel under investigation. Similarly, operators can be constructed for the higher energy states of the glueballs in each channel.

5.2.7 Setting the Scale

In order to convert the glueball masses measured into physical values, we must determine the temporal lattice spacing, a_t. To do this, we choose some physical quantity, measured experimentally, and measure it on the lattice in terms of a_t [55]. The experimentally known value is then used to determine the lattice spacing. A quantity which is well determined experimentally, and easily evaluated numerically is the best choice. Usually the mass of some low-energy particle is used. However, experimental glueball results afford us no such candidate.

Instead, we look at the hadronic scale parameter, r_0, defined in terms of the force between quarks;

$$r^2 \frac{dV(\vec{r})}{dr}\bigg|_{r=r_0} = 1.65. \tag{5.50}$$

The benefits of this technique are listed in Ref. [56]. One problem this approach is that r_0 can not be measured by direct experiment.

To measure r_0, we first calculate the static quark potential, $V(\vec{r})$, for various values of r, from the expectation vales of Wilson loops. We see that

$$W(\vec{r}, t) = Z(\vec{r}) e^{-V(\vec{r})t}. \tag{5.51}$$

These measurements are made independently of glueball mass simulations. Again to avoid excited state contributions, single link smearing is used. Statistical noise is significantly reduced by constructing Wilson loops with thermally averaged temporal links. As when extracting a mass from a correlation function, the potential is taken from the exponential behaviour of the Wilson loops. A suitable plateau region is chosen to minimise the uncertainty in $V(\vec{r})$ and a χ^2 fit is used to extract the best fit values.

We now make an ansatz for the form of the potential;

$$V(\vec{r}) = \frac{e_c}{r} + \sigma r + V_0. \tag{5.52}$$

This form of the potential was found to fit the data on course lattices well. Differentiating analytically, we see that

$$\frac{r_0}{a_s} = \sqrt{\frac{1.65 + e_c}{\sigma a_s^2}} \tag{5.53}$$

in terms of the string tension, σ. To find the ratio, r_0/a_s, we need the anisotropy factor, a_s/a_t, since our estimates of the potential are in terms of a_t ($a_t V(\vec{r})$). Since the renormalisation is small [55], it is safe to use ξ for the anisotropy factor.

While r_0 was first introduced as a replacement for the string tension to avoid fitting data over different length scales, which is affected by lattice artefacts at short distances and by finite volume effects at large distances, the lattices used in this study are too coarse to apply this procedure.

Now that we have discussed all the issues in extracting the energy spectrum from glueball calculations, we move on to look at the results which have been obtained thus far.

5.3 Glueball & $\pi\pi$ Correlators

Measurements were made on 100 configurations of a $8^3 \times 96$ lattice, with two flavours of dynamical quarks and using the tuned parameters of Ref. [55]. Fig. 5-4 shows the correlation functions between smeared Wilson loop sources, such as would be used to measure the glueball spectrum in the theory of gluons alone. Operator 2 is seen to have the lowest noise, but signals are seen in all channels. Fig. 5-5 shows the correlation between these three operators and the distilled two-pion operator (with zero relative momentum). Again, very good signals are observed for such low statistics. Analogous to the $\phi \rightarrow \chi\chi$ matrix elements, the accurate measurement of this correlator forms a vital part in the estimation of the energy levels in the neighbourhood of the avoided level crossings.

Fig. 5-3 shows the disconnected part of the correlation function between two pions at rest at the source and the same sink function. The distillation matrix elements of Eqn. 5.36 are needed for propagation from time-slice t back onto itself for all values of $t = 0 \ldots 95$. These elements can be estimated efficiently using a stochastic method where sources are added every four time-slices with random weights. Two independent random sources are needed to compute the two propagators on each time-slice (as seen in the left panel of Fig. 5-2). Unfortunately, when the sources are on time-slices t such that $t \mod 4 = 0$, four sources would be needed. Since this is

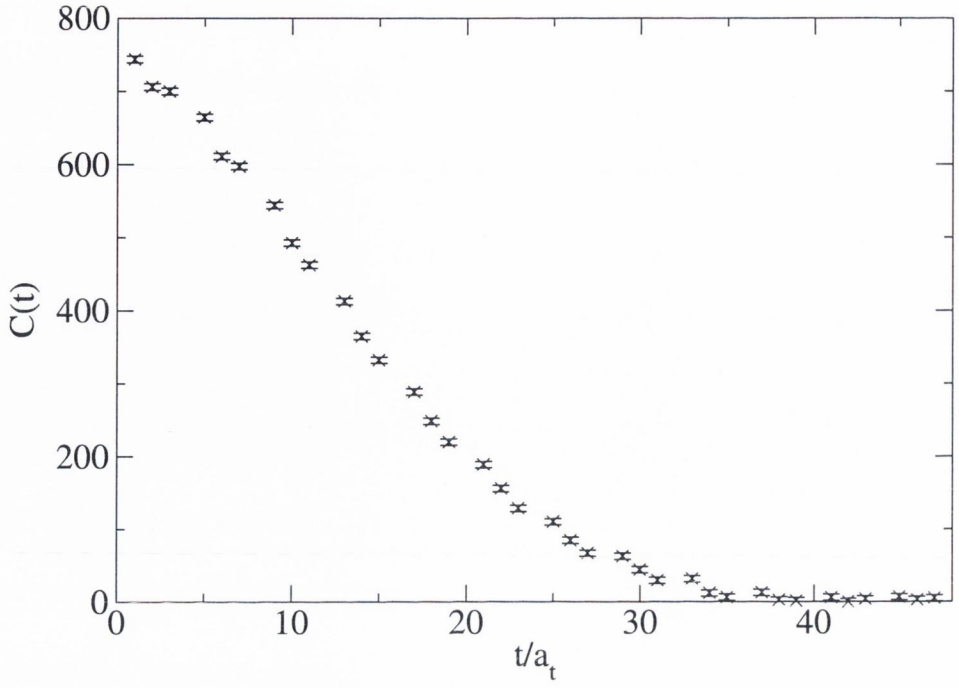

Figure 5-3: $\pi\pi \rightarrow \pi\pi$ correlator.

unavailable in the data set used here, these time-slices are absent from Fig. 5-3.

In these test simulations, $m_\pi \sim 700$ MeV and the only open threshold is the $G \rightarrow \pi\pi$ decay. As the physical pion mass is approached, more thresholds open. Present tests are a long way from exploring this complication.

As was demonstrated with the model $\phi \rightarrow \chi\chi$ theory, the successful application of Lüscher's method depends largely on the measurement of the $\phi \rightarrow \chi\chi$ elements of the correlation matrix in the vicinity of the avoided level crossings. The results presented above clearly show that the $G \rightarrow \pi\pi$ measurements have advanced to a point where a serious attempt to implement Lüscher's method can be made. In the immediate future, the next step will be to enlarge the set of glueball operators being used, and include the connected terms in the $\pi\pi$ operator. This would provide the tools necessary to investigate the finite volume energy spectrum, progressing towards the glueball decay width.

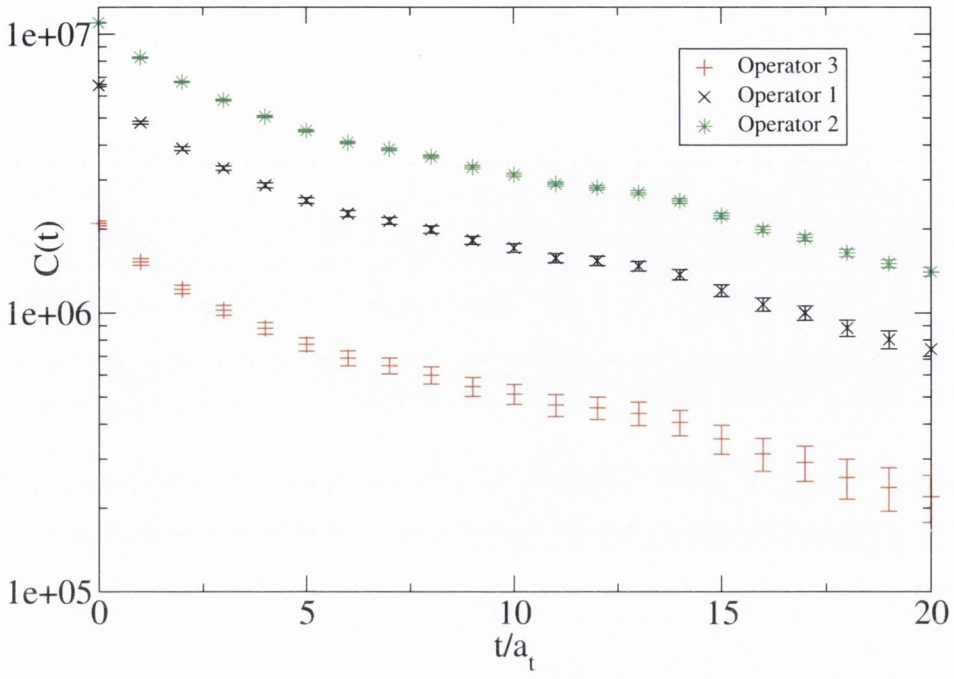

Figure 5-4: $G \to G$ correlator.

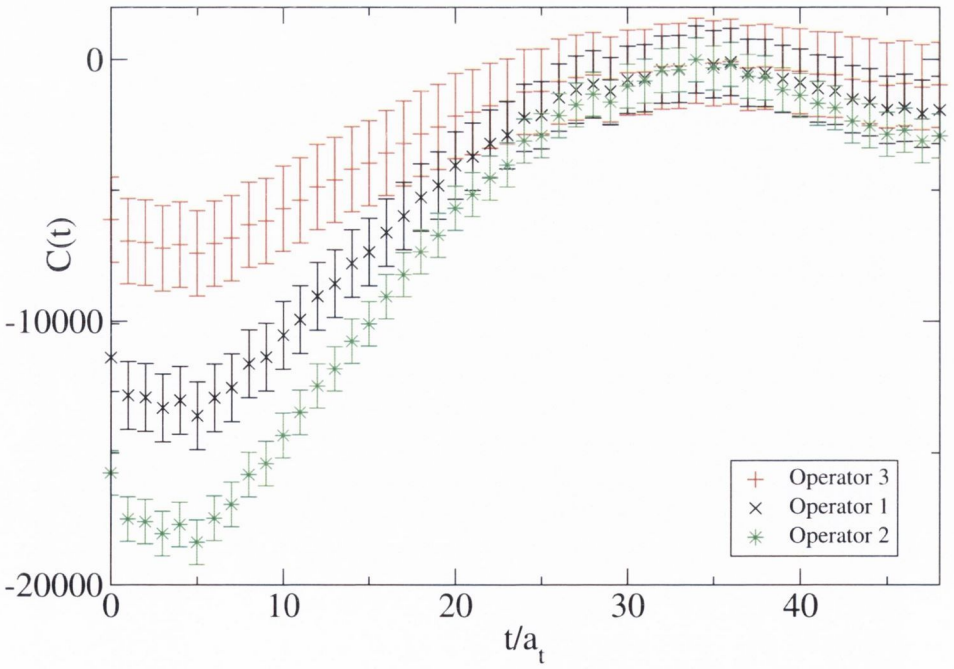

Figure 5-5: $G \to \pi\pi$ correlator.

Chapter 6

Conclusions

6.1 Conclusion

The existence of glueballs would provide strong evidence for the acceptance of Quantum Chromodynamics as the theory of the strong interaction. But, as was highlighted in the introduction, the differing observables in theory and experiment, presents a fundamental problem in the identification of glueballs. This problem originates in the Maiani-Testa Theorem which infers that there can be no direct access to the decay width, as measured by experimentalists, from the Euclidean correlation functions, as calculated by theorists.

We have demonstrated how a link can be made between a Euclidean correlation matrix and the particle decay width, via the finite volume energy spectrum and the scattering phase shift, as prescribed by Lüscher in [9]. This method is based on a one-to-one correspondence between solutions to the Helmholtz equation and solutions to the stationary Schrödinger equation.

To gain an understanding of how this might be implemented for the glueball to $\pi\pi$ decay, we created a model scalar field theory which allowed a ϕ particle to decay into two χ particles, when kinematically possible. We explored the finite volume energy spectrum and scattering phase shift of this theory using Euclidean perturbation theory, as well as performing direct calculations of the decay width of the ϕ particle in Minkowski perturbation theory.

These calculations provided a valuable comparison to the results of the Monte Carlo simulations carried out in the $\phi \to \chi\chi$ theory. Using Markov Chain Monte Carlo integration techniques, we were able to extract the finite volume energy spectrum for a collection of ϕ and $\chi\chi$ states. From this point, we followed Lüscher's method from the energy spectrum to the associated momenta, which was used to evaluate the scattering phase shift before, finally, fitting this data to a Breit-Wigner formula to extract a value of the decay width of the ϕ particle. The results were, at all points of contact, in good agreement with the perturbative results. In particular, our estimates of the decay width all agreed to within 10%.

A first investigation of the corresponding correlation functions in QCD that would mediate decay between the scalar glueball (in analogy with the ϕ field of the model) and two-pion states (the χ field of the model) was performed. The calculation was done on very low statistics for a study of gluonic physics, using only 100 gauge field configurations. Nevertheless, good signals were seen that would enable the first calculations of mixing between glueball states and pions at finite volume to be carried out. This would be the first step towards a reliable determination of the decay parameters of the scalar glueball of QCD and would give direct information relevant to experimental searches for these states.

Bibliography

[1] X. Feng, X. Li, and C. Liu. "Two Particle States in an Asymmetric Box and the Elastic Scattering Phases". *Phys.Rev.* **D70**, 014505 (2004).

[2] A. A. Natale. "Hadronic Physics in Peripheral Heavy Ion Collisions". *Braz.J.Phys.* **32**, 849 (2002).

[3] C.McNeile *et al.*(**UKQCD** Collaboration). "Properties of Light Scalar Mesons from Lattice QCD". *Phys.Rev.* **D74**, 014508 (2006).

[4] G. S. Bali *et al.*(**TXL** Collaboration). "Static Potentials and Glueball Masses from QCD Simulations with Wilson Sea Quarks". *Phys.Rev.* **D62**, 054503 (2000).

[5] C. McNeile *et al.*(**UKQCD** Collaboration). "Mixing of Scalar Glueballs and Flavour-Singlet Scalar Mesons". *Phys.Rev.* **D63**, 114053 (2001).

[6] A.Hart *et al.*(**UKQCD** Collaboration). "On the Glueball Spectrum in O(a)-Improved Lattice QCD". *Phys.Rev.* **D65**, 034502 (2002).

[7] C. McNeile. "Hard Hadron Spectroscopy". *PoSLAT2007*, 19 (2007).

[8] L. Maiani and M. Testa. "Final State Interactions from Euclidean Correlation Functions". *Phys.Lett.* **B245**, 585 (1990).

[9] M. Lüscher. "Two-Particle States on a Torus and their Relation to the Scattering Matrix". *Nucl.Phys.* **B354**, 531 (1991).

[10] M. Lüscher. Lectures given at Les Houches (1988), in: Fields, Strings and Critical Phenomena. Eds. E. Brézin, J. Zinn-Justin (North-Holland, Amsterdam, 1989).

[11] M. Lüscher. "Volume Dependence of the Energy Spectrum in Massive Quantum Field Theories, II. Scattering States". *Commun.Math.Phys.* **105**, 153 (1986).

[12] X. Li and C. Liu. "Two Particle States in an Asymmetric Box". *Phys.Lett.* **B587**, 100 (2004).

[13] A. Messiah. *Quantum Mechanics, Vols. I,II.* North Holland, Amsterdam, 1965.

[14] K. Rummukainen and S. Gottlieb. "Resonance Scattering on the Lattice with Nonzero Total Momentum". *Nucl.Phys.* **B450**, 397 (1995).

[15] C. J. Morningstar and M. J. Peardon. "Glueball Spectrum from an Anisotropic Lattice Study". *Phys.Rev.* **D60**, 034509 (1999).

[16] M. Lüscher. "Volume Dependence of the Energy Spectrum in Massive Quantum Field Theories, I. Stable States". *Commun.Math.Phys.* **104**, 177 (1986).

[17] M. Lüscher. "Signatures of Unstable Particles in Finite Volume". *Nucl.Phys.* **B364**, 237 (1991).

[18] N. H. Christ, C. Kim, and T. Yamazaki. "Finite Volume Corrections to the Two-Particle Decay of States with Nonzero Momentum". *Phys.Rev.* **D72**, 114506 (2005).

[19] M. Gockeler, H. A. Kastrup, J. Westphalen, and F. Zimmermann. "Scattering Phases on Finite Lattices in the Broken Phase of the Four-Dimensional O(4) ϕ^4 Theory". *Nucl.Phys.* **B425**, 413 (1994).

[20] M. Lüscher and U. Wolff. "How to Calculate the Elastic Scattering Matrix in Two-Dimensional Quantum Field Theories by Numerical Simulation". *Nucl.Phys.* **B391**, 222 (1990).

[21] C. R. Gattringer and C. B. Lang. "Resonance Scattering Phase Shifts in a 2-d Lattice Model". *Nucl.Phys.* **B391**, 413 (1993).

[22] H. R. Fiebig and R. M. Woloshyn. "Meson Meson Scattering in (2+1)-Dimensional Lattice QED". *Nucl.Phys.Proc.Suppl.* **B30**, 883 (1993).

[23] H. R. Fiebig, R. M. Woloshyn, and A. Dominiguez. "Meson Meson Scattering in (2+1)-Dimensional Lattice QED". *Nucl.Phys.* **B418**, 649 (1994).

[24] M. Guagnelli, E. Marinari, and G. Parisi. "Scattering Lengths From Fluctuations". *Nucl.Phys.* **B240**, 188 (1990).

[25] R. Gupta, A. Patel, and S. Sharpe. "$I = 2$ Pion Scattering Amplitude with Wilson Fermions". *Phys.Rev.* **D48**, 388 (1993).

[26] M. Fukugita *et al.* "Hadron Scattering Lengths in Lattice QCD". *Phys.Rev.* **D52**, 3003 (1995).

[27] S. Aoki *et al.* "$I = 2$ Pion Scattering Length with Wilson Fermions". *Phys.Rev.* **D66**, 077501 (2002).

[28] C. Liu, J. Zhang, Y. Chen, and J.P. Ma. "Calculating the $I = 2$ Pion Scattering Length using Tadpole Improved Clover Wilson Action on Coarse Anisotropic Lattices". *Phys.Rev.* **B624**, 360 (2002).

[29] P. Hasenfratz, K.J. Juge, and F. Niedermeyer. "New Results on Cut-off Effects in Spectroscopy with the Fixed Point Action". *JHEP* **0412**, 030 (2004).

[30] X. Du, G. Meng, C. Miao, and C. Liu. "$I = 2$ Pion Scattering Length with Improved Actions on Anisotropic Lattices". *Int. J. Mod. Phys.* **A19**, 5609 (2004).

[31] S. Aoki *et al.* "$I = 2$ Pion Scattering Length from Two-Pion Wave Functions". *Phys.Rev.* **D71**, 094504 (2005).

[32] S. Aoki *et al.* "$I = 2$ Pion Scattering Phase Shift with Wilson Fermions". *Phys.Rev.* **D67**, 014502 (2003).

[33] T. Yamazaki *et al.* "$I = 2$ $\pi\pi$ Scattering Phase Shift with Two Flavours of $O(a)$ Improved Dynamical Quarks". *Phys.Rev.* **D70**, 074513 (2004).

[34] S. R. Beane, P. F. Bedaque, K. Orginos, and M. J. Savage. "$I = 2$ $\pi\pi$ Scattering from Fully-Dynamical Mixed Action Lattice QCD". *Phys.Rev.* **D73**, 054503 (2006).

[35] S. Aoki *et al.* "Lattice QCD Calculation of the ρ Meson Decay Width". *Phys.Rev.* **D76**, 094506 (2007).

[36] H.J. Rothe. *Lattice Gauge Theories, An Introduction.* World Scientific, 3rd edition, 2005.

[37] M. E. Peskin and D. V. Schroeder. *An Introduction to Quantum Field Theory.* Advanced Book Program, 1995.

[38] J.R. Taylor. *Scattering Theory.* Wiley, 1972.

[39] Mark Srednicki. *Quantum Field Theory.* Cambridge University Press, 2007.

[40] W. Press, S. Teukolsky, W. Vetterling, and B. Flannery. *Numerical Recipes in C.* Cambridge University Press, 2007.

[41] M. Mitchell. *An Introduction to Genetic Algorithms.* MIT Press, 1996.

[42] W. Ochs. "Searching for the Scalar Glueball". *AIPConf.Proc.* **1030**, 207 (200).

[43] H. Forkel. "Scalar Gluonium and Instantons". *Phys.Rev.* **D64**, 034015 (2001).

[44] K.T. Chao, X.G. He, and J.P. Ma. "On Two-Body Decays of a Scalar Glueball". *Eur.Phys.J.* **C55**, 417 (200).

[45] P. Minkowski and W. Ochs. "Scalar Mesons in B-decays". *AIP Conf. Proc.* **814**, 52 (2006).

[46] S. Narison. "QCD Tests of the Puzzling Scalar Mesons". *Phys.Rev.* **D73**, 114024 (2006).

[47] Y. Chen *et al.* "Glueball Spectrum and Matrix Elements on Anisotropic Lattices". *Phys.Rev.* **D73**, 014516 (2006).

[48] W.-J. Lee and D. Weingarten. "Scalar Quarkonium Masses and Mixing with the Lightest Scalar Glueball". *Phys.Rev.* **D61**, 014015 (2000).

[49] T. Kunihiro *et al.*(**SCALAR** Collaboration). "Scalar Mesons in Lattice QCD". *Phys.Rev.* **D70**, 034504 (2004).

[50] C. J. Morningstar and M. J. Peardon. "Efficient Glueball Simulations on Anisotropic Lattices". *Phys.Rev.* **D56**, 4043 (1997).

[51] A. Hart *et al.*(**UKQCD** Collaboration). "A Lattice Study of the Masses of Singlet 0^{++} Mesons". *Phys.Rev.* **D74**, 114504 (2006).

[52] K. Symanzik. "Continuum Limit and Improved Action in Lattice Theories. 1. Principles and ϕ^4 Theory". *Nucl.Phys.* **B226**, 187 (1983).

[53] G. P. Lepage and P. B. MacKenzie. "Viability of Lattice Perturbation Theory". *Phys.Rev.* **D48**, 2250 (1993).

[54] T. DeGrand and C. DeTar. *Lattice Methods for Quantum Chromodynamics.* World Scientific Publishing Company, 2006.

[55] R. Morrin, A. O'Cais, M. Peardon, S.M. Ryan, and J. Skullerud. "Dynamical QCD Simulations on Anisotropic Lattices". *Phys.Rev.* **D74**, 014505 (2006).

[56] R. Sommer. "A New Way to Set the Energy Scale in Lattice Gauge Theories and its Applications to the Static Force and α_s in SU(2) Yang-Mills Theory". *Nucl.Phys.* **B411**, 839 (1994).